UNIVERSIDADE ESTADUAL DE CAMPINAS
Faculdade de Engenharia Elétrica e de Computação

Jorge Rufino Fernández Herrera

Plasmonic sensing contributions using prism and waveguide coupling platforms
Contribuições no sensoriamento plasmônico usando as plataformas de acoplamento por prisma e guia de onda

Campinas

2023

Jorge Rufino Fernández Herrera

Plasmonic sensing contributions using prism and waveguide coupling platforms

Contribuições no sensoriamento plasmônico usando as plataformas de acoplamento por prisma e guia de onda

Tese apresentada à Faculdade de Engenharia Elétrica e de Computação da Universidade Estadual de Campinas como parte dos requisitos exigidos para a obtenção do título de Doutor em Engenharia Elétrica, na Área de Telecomunicações e Telemática.
Thesis presented to the Faculty of Electrical and Computing Engineering of the University of Campinas as part of the requirements for obtaining the title of Doctor in Electrical Engineering, in the area of Telecommunications and Telematics.

Orientador: Prof. Dr. Hugo Enrique Hernandez Figueroa

Este trabalho corresponde à versão final da dissertação/tese defendida pelo aluno Jorge Rufino Fernández Herrera, e orientada pelo Prof. Dr. Hugo Enrique Hernandez Figueroa.

Campinas

2023

Ficha catalográfica
Universidade Estadual de Campinas
Biblioteca da Área de Engenharia e Arquitetura
Elizangela Aparecida dos Santos Souza - CRB 8/8098

F391p

Fernandez Herrera, Jorge Rufino, 1987-
Plasmonic sensing contributions using prism and waveguide coupling platforms / Jorge Rufino Fernandez Herrera. – Campinas, SP : [s.n.], 2023.

Orientador: Hugo Enrique Hernandez-Figueroa.
Tese (doutorado) – Universidade Estadual de Campinas, Faculdade de Engenharia Elétrica e de Computação.

1. ressonância de plasmon de superfície. 2. Análise modal. 3. Biossensores remoto. 4. Plasmônicas. 5. Engenharia do plasma. I. Hernandez-Figueroa, Hugo Enrique, 1959-. II. Universidade Estadual de Campinas. Faculdade de Engenharia Elétrica e de Computação. III. Título.

Informações Complementares

Título em outro idioma: Contribuições no sensoriamento plasmônico usando as plataformas de acoplamento por prisma e guia de onda
Palavras-chave em inglês:
Surface plasmon resonance
Modal analysis
Remote biosensor
Plasmonics
Plasma engineering
Área de concentração: Telecomunicações e Telemática
Titulação: Doutor em Engenharia Elétrica
Banca examinadora:
Hugo Enrique Hernandez Figueroa
Jorge Ricardo Mejía Salazar
Jhonattan Cordoba Ramirez
Gilliard Nardel Malheiros Silveira
Eric Fujiwara
Data de defesa: 17-02-2023
Programa de Pós-Graduação: Engenharia Elétrica

Identificação e informações acadêmicas do(a) aluno(a)
- ORCID do autor: https://orcid.org/0000-0003-3563-2510
- Currículo Lattes do autor: http://lattes.cnpq.br/0578145994974268

COMISSÃO JULGADORA - TESE DE DOUTORADO

Candidato(a): Jorge Rufino Fernández Herrera RA: 144396
Data de defensa: 17 de Fevereiro de 2023
Titulo da Tese: "Plasmonic sensing contributions using prism and waveguide coupling platforms"

Prof. Dr. Hugo Enrique Hernandez Figueroa (Presidente)
Prof. Dr. Jorge Ricardo Mejía Salazar
Prof. Dr. Jhonattan Cordoba Ramirez
Prof. Dr. Gilliard Nardel Malheiros Silveira
Prof. Dr. Éric Fujiwara

A Ata de Defesa, com as respectivas assinaturas dos membros da Comissão Julgadora, encontra-se no SIGA (Sistema de Fluxo de Dissertação/Tese) e na Secretaria de Pós-Graduação da Faculdade de Engenharia Elétrica e de Computação.

De forma resuelta dedico esta tesis al pueblo trabajador brasileño. A los que luchan, aunque tal vez de forma confusa y a veces contradictoria, por un mejor país. Un país que es diferente, pero es el mismo que Perú, donde miré el cielo por primera vez, maravillado y consciente. Que es diferente y el mismo que Colombia, que casi no conozco, pero lo conozco porque leí y conocí colombianos fundamentales. El mismo país que es la Patria Grande, porque las fronteras son un invento caduco y reaccionario.

De forma resuelta, desde el pedazo de cielo del Abya Yala más cercano de África. Tambaú, João Pessoa (Paraíba). 18/10/2022.

Agradecimentos

Agradeço a CONCYTEC/CIENCIACTIVA pelo recurso de financiamento no marco do programa de 'Becas de doctorado en el exterior' do governo peruano, qual me manteve durante os três primeiros anos do doutorado com contrato FONDECYT 115-2017. Também o presente trabalho foi realizado com apoio da Coordenação de Aperfeiçoamento de Pessoal de Nível Superior - Brasil (CAPES) - Código de Financiamento 001, processo: 88887.508709/2020-00, qual me apoiou durante o tempo da pandemia. Finalmente agradeço o apoio que recebi como bolsista Sisfoton/CNPq, formando parte do grande time do Sisfoton da UNICAMP, como laborátorio integrante do Sistema Brasileiro de Fotônica.

Agradeço também o apoio permanente dos meus familiares, em particular, meus pais Juan Fernández e Sara Herrera quem, desde pequeno, sempre me incentivaram a leitura e estudo, além da exploração da natureza. Sem o seu apoio permanente para seguir uma carreira científica, teria sido muito mais difícil chegar até aqui.

Agradeço também profundamente ao meu orientador, Prof. Dr. Hugo Figueroa, bem como a sua esposa, Profa. Marli Freitas, quem me apoiaram em muito mais do que uma orientação acadêmica, abrindo-me as portas de sua casa e me tratando como mais um membro da família. Agradeço seu apoio e a oportunidade de compartilhar conversas acadêmicas e sobre muitas outras questões humanas. Muito obrigado.

Agradeço aos meus colegas de laboratório quem, com suas conversas, ajudaram a esclarecer as ideias e conceitos ou até mesmo a se divertir durante a realização da pesquisa. Não teria sido possível sem Yesica Rumaldo, Ursula Salazar, Paloma Pellegrini e Yuri Isayama, compartilhando muito nos últimos anos.

Aproveito também para agradecer aos amigos que forjei ao longo dos anos pelo tempo que compartilhamos, são muitos, mas menciono em particular ao Juan Sebastián, Carlos Donizete, Sérgio Ribeiro, Thiago Barbosa, Sylvia Caroline, Johann Baader, Vinícius Ares, Víctor Sánchez e Alex Rodríguez, quem junto com meus velhos amigos Víctor Cáceres, Leonid Huancachoque e Alex Valle ajudaram muito a conhecer melhor o Brasil e outros cantos da América Latina.

"The most beautiful thing we can experience is the mysterious. It is the source of all true art and all science. He to whom this emotion is a stranger, who can no longer pause to wonder and stand rapt in awe, is as good as dead: his eyes are closed."

(Albert Einstein)

Resumo

As plataformas de detecção plasmônica têm as maiores perspectivas de crescimento no campo de sensores e biossensores ópticos. Recursos unicos, como monitoramento em tempo real, alta sensibilidade, ressonâncias de alto fator de qualidade, dentre outros, permitem que esses sensores sejam amplamente utilizados hoje para uma variedade de aplicações, desde a caracterização de novos medicamentos até aplicações em monitoramento ambiental. A plataforma plasmônica mais utilizada é aquela que utiliza um prisma como interface de acoplamento. Essa configuração, chamada de configuração Kretschmann, é a que tem mais presença hoje em laboratórios e clínicas de todo o mundo que trabalham com essa tecnologia. Esta tese estuda essa configuração explorando suas possibilidades e limites, levando em consideração a espessura da camada de adesão, por vezes ignorada, em seu desempenho como sensor. A análise foi validada com uma experiência prática na análise da pureza do etanol. Esses resultados sugerem novos limites aos padrões da lâmina de ouro usados nos setups comerciais. Em relação a uma plataforma plasmônica integrada, o presente trabalho inclui um estudo analítico e primeiros testes experimentais de um tipo de estrutura HPWG (Hybrid Plasmonic-Dielectric Waveguide) como sensor, utilizando SiO_2 como cobertura de baixo índice. É feita uma análise do impacto da espessura do núcleo e da cobertura, bem como o impacto da espessura e comprimento da camada de ouro no desempenho do sensor.

Palavras-chaves: ressonância de plasmon de superfície; configuração de Kretschmann; Guía de onda híbrido plasmônico-dielétrico; análise modal; sensoriamento.

Abstract

Plasmonic sensing platforms have the greatest growth prospects within the field of optical sensors and biosensors. Unique capabilities such as real-time monitoring, high sensitivity, high quality factor resonances, among others, allow these sensors to be widely used today for a variety of applications from characterization of new drugs to environmental monitoring applications. The most widely used plasmonic platform is the one that uses a prism as the coupling interface. This configuration, called the Kretschmann configuration, is the one with the most presence today in laboratories and clinics around the world that work with this technology. This thesis studies this configuration exploring its possibilities and limits, taking into account the sometimes ignored thickness of the adhesion layer in its performance as a sensor. The analysis was validated with a practical experience in the analysis of the purity of ethanol. These results suggest new limits to the gold layer standards used in commercial equipment. In the aspect of an integrated plasmonic platform, the present work includes an analytical study and first experimental tests of a specific type of HPWG (Hybrid Plasmonic-Dielectric Waveguide) structure as a sensor, using SiO_2 as low-index cladding. An analysis is made of the impact of core thickness and overcladding, as well as the impact of thickness and length of the gold layer on its performance as a sensor.

Keywords: surface plasmon resonance; Kretschmann configuration; Hybrid Plasmonic-Dielectric Waveguide; modal analysis; sensing.

Lista de ilustrações

Lista de tabelas

Lista de abreviaturas e siglas

SARS-CoV-2	Severe acute respiratory syndrome coronavirus 2
LoC	Lab on a Chip
PoC	Point of Care
HPWG	Hybrid Plasmonic Waveguide
SPP	Surface Plasmon Polaritons
SPR	Surface Plasmon Resonance
MIM	Metal-insulator-metal
LEMAC	Laboratory of Applied and Computational Electromagnetism
CMOS	Completamentary Metal-Oxide-Semiconductor
TE	Transversal Electric
TM	Transversal Magnetic
ATR	Attenuated total reflection
FEEC	Faculty of Electrical and Computing Engineering
IFGW	Physics Institute Gleb Wataghin
RPM	Revolution per minute
FWHM	Full width half minimum
FoM	Figure of Merit
LoD	Limit of detection
RIU	Refractive Index Unit
GUI	Graphics User Interface
AU	Arbitrary Units
CCD	Charged Coupled Device
ER	Extinction Ratio
FDTD	Finite-difference time-domain
BPC	Best Potential Case

Lista de símbolos

m	Effective optical mass
γ	Characteristic collision frequency
ω_p	Plasma frequency
β	Propagation constant
ε	Dielectric permitivity
mW	MiliWats

Sumário

1 INTRODUCTION

1.1 Overview

The years 2020 and 2021 witnessed a phenomenon with a very high impact, although recurrent in history, for life in human society: a pandemic. In December 2019, the first outbreaks of a new variant of the coronavirus, SARS-CoV-2, were detected in China. The advance of this pandemic caused that by April 2020, around half of the world's population was in the 90 countries or territories in which governments had implemented some type of lockdown policies (SANDFORD, 2020). This attitude revealed how fragile, although advanced compared to the pandemics of previous centuries, medical and epidemiological science is to face situations of this nature (leaving aside for a moment the great problems of social inequality, access to health and unhealthy living conditions in which billions of people subsist), while the number of deaths from the pandemic has passed 6 million (SCHOOL, 2022).

Faced with this dramatic situation, one of the main challenges is early diagnosis. Early diagnosis makes it possible to detect, through a sample from the patient, small concentrations of the virus or some bodily agent that reacts to its presence and that serves as an indicator of its invasion in the patient, even without the appearance of any detectable symptoms (DEBACKERE; BIENSTMAN; BAETS, 2009; Aruna Gandhi et al., 2019). In this way, this diagnosis allows attacking the disease in the initial stages of its development and leads to a greater possibility of successful treatment. Early diagnosis technologies have been developed to combat various ailments such as heart attack (KRUPIN; BERINI, 2019), diabetes, infectious diseases, among others (search not only plasmonic).

This need for early diagnosis, together with the goal of developing low-cost (by clinical laboratory standards), portable technology that can be implemented in Point-of-Cares in rural areas leads to the concept of Lab-on-a-Chip: a micro platform that allows reliable medical diagnoses, with few inputs and easy to use (ZHUANG et al., 2020; SOLER; HUERTAS; LECHUGA, 2019). The Lab-on-Chip concept has been developing since the 1980s with working groups that currently show great advances, as in the case of diabetes and cholesterol control.

Another point to highlight is the importance of plasmonic sensors as a crucial force among optical sensors (HILL, 2016; MEJÍA-SALAZAR; OLIVEIRA, 2018). According to (Richard B. M. Schasfoort, 2017) among the use of plasmonic sensors, the sensing platform based on the Kretschmann configuration is the most common, already consolidated in the market as an important tool in the analysis of sensing and biosensing, drug discovery

and instrumentation (Affinité Instruments, 2019). The search for an on-chip plasmonic sensing application is also quite sought after, highlighting MIM, interferometric and HPWG-based structures which present a wide variety of simulated and tested structures (Fernandez H; RUMALDO; HERNANDEZ-FIGUEROA, 2022; ALAM, 2012), but still under development to gain traction as a viable integrated option.

1.2 Motivation and scope research

Initially, the thesis project was born with the idea of strengthening the line of photonics for sensing in the Laboratory of Applied and Computational Electromagnetism, this time focusing on biodetection. Since 2013, a collaboration had begun with the Catalan Institute of Nanoscience/Nanotechnology of Barcelona (ICN2) within the framework of a project for the development of new optical biosensing platforms by interferometry. This collaboration allowed the development of an optical sensing device based on a trimodal waveguide, using SU8 photoresist as raw material, a material that was explored both for its optical and biofunctional characteristics (RAMIREZ et al., 2015; RAMIREZ et al., 2018). In parallel, a first version of the SPR sensor was developed in the group, under the Kretschmann configuration, oriented towards the analysis of a first version of the Kretschmann SPR mounted on the LEMAC and its sensitivity using air, water, isopropyl alcohol and ethanol (MOREIRA, 2016).

This thesis fits into this last line of work, that of plasmonic sensing platforms for detection. This thesis fulfills the role of a previous step to that of a biodetection platform, since one of its main axes has been to improve and develop a new prism-based plasmonic detection platform, which represents a second version of the SPR sensor in the LEMAC. This time, with a complete management system for tracking analysis in real time and with an operating microfluidic system, capable of being used in other interrogation systems, in addition to the angular one. The $\theta/2\theta$ rotation system is the one that has been used for sensitivity analysis and human-computer interface development.

Additionally, and in accordance with the aim of joining the development of on-chip detection platforms, the device based on the Hybrid Plasmonic Waveguide (HPWG) structure has been explored with the differential that works from a slab guide perspective and using a low index material of silicon oxide, with a metallic deposition on this substrate. In this respect, a theoretical analysis on the impact of the length of gold is carried out, together with some initial experimental tests.

There are other feasible plasmonic platforms to be analyzed and developed that have not been included in this work, such as the use of metallized multimode fibers, diffraction gratings in waveguides or the use of spatial reflection modulator to improve the detection limit, only to mention some of the options that were addressed at the time, but

that do not have results to date. However, they remain pending to be worked on in future scientific projects and contributions.

1.3 Goal and objective of the thesis

From the description of the motivation and scope of the research, it can be expressed concretely that the goal and objectives of the thesis are the following:

- Analysis of the behavior of prism-based plasmonic resonance, its limitations and performance, focused on the impact of microfabrication aspects, in particular, the thickness of the titanium and gold layer. It also addresses the development of a detection management system for the Kretschmann setup at LEMAC for a functional prototype. This platform was used to experimentally verify the theoretical approach on the impact of Ti/Au thickness on sensing performance.
- Approach of integrated platforms that can perform plasmonic detection from a hybrid dielectric-plasmonic (HPWG-based) platform. Design considerations, in relation to the thickness of the dielectric materials, from the modal analysis for the case of slab guides, as well as the gold layer, both its thickness and the impact of the length.

Both objectives were met and are exposed in this thesis.

1.4 Primary contributions to scientific knowledge

This thesis presents the following scientific contributions:

- Detection platform by Kretschmann of high sensitivity "home-made". Developed from a Data Acquisition and Management platform using Arduino+Python. This detection platform reaches a detection limit of 2.3E-4RIU, which allows it to be used as a real-time monitoring and detection platform, similar to commercial SPR systems.
- Identification of the impact of the thickness of titanium and gold on the sensing performance based on the semi cylindrical prism. Usually, commercial equipments which work in this configuration use 50 nm gold thickness, a determination that is carried out by various research groups and in experimental setups. However, in the present work, from a theoretical and experimental approach, it is shown that this thickness does not always represent the best option for all applications. It is shown that in the case of the exposed application a gold thickness of 75 nm presents better sensitivity and detection limit.

- Identification of the performance and main elements of the hybrid-plasmonic sensor from the modeling of the modal exchange area in the hybrid region and the impact of the length of the gold surface on the sensor performance: sensitivity (S) and figure of merit (FoM). This contribution allows us to consider this new variable in the design and obtain improvements in the manufacturing performance of this hybrid sensor, compatible with CMOS manufacturing technology.

1.5 Organization of the thesis

As this thesis deals with the study of two plasmonic detection platforms, the chapters have been adapted to have a certain independent tenor to describe each of the platforms with their contributions. In Chapter 2, a technical presentation of plasmonic technology, its fundamentals, a compilation of its current formats and developments is made. Chapters 3 and 4 are dedicated to the detection platforms used, both in their description and detection performance. Chapter 3 deals with the Kretschamnn configuration, the prototype at the LEMAC (both in its mechanical design and its Data Management system) and its performance. Chapter 4 presents the On-Chip detection platform, where the dielectric-plasmonic hybrid waveguide (HPWG) is presented, details of its design, fabrication and characterization. In each of these chapters, the design aspects, manufacturing challenges and the experimental tests developed are presented. Finally, Chapter 5 presents the conclusions and perspectives for future work.

2 FUNDAMENTALS AND CURRENT STATUS OF THE TOPIC

Although the phenomenon of plasmonics is well documented and explained in the literature, we have decided to begin the Chapter 2 with a brief description of the fundamental guidelines involved (Section 2.1). Subsequently, in Section 2.2, a compilation of achievements obtained in the plasmonic sensors presented in the technical literature is made.

2.1 Basics of plasmonics

Initial observations of what is now known as plasmons occurred at the beginning of the 20th century, when the appearance of dark bands in the spectrum of refracted light on a metal diffraction grating were reported and they were referred to as anomalies (WOOD, 1901). Throughout the twentieth century other similar observations were reported until in the year 1968 Otto explains some of these results indicating that the dark bands are produced due to the appearance of superficial plasmons in metal sheets (OTTO, 1968).

The plasmons constitute a type of evanescent wave that appear specifically in metal-dielectric interfaces, presenting among its most representative characteristics a high attenuation and high field strength (HOMOLA, 2006b). It is also important to indicate that by altering the structure of the metal surface, the properties of the plasmons can be modified, which offers great potential for various applications with photonic devices. In this way, it is an interesting alternative for integrated optical applications in short distances and in detection applications (biosensing) (BARNES; DEREUX; EBBESEN, 2003).

On the other hand, an optical sensor is a device that, by optical means, converts a physical quantity into one of another nature which is typically encoded within some of the wave's characteristics. In the case of sensors based on Surface Plasmon Resonance - SPR, a surface plasmon is excited at the metal-dielectric interface allowing the measurement of changes in the refractive index of the material by varying the propagation constant of the plasmon superficial. The change of the propagation constant of the plasmon is translated as a variation of the coupling conditions between the excitatory light and the plasmon and which can be observed by means of some of the coupling parameters adopted in the experimental scheme, such as the angle of incidence, wavelength, phase or by polarization modulation (Fig. 2.1). This also constitutes one of the classification criteria of SPR sensors.

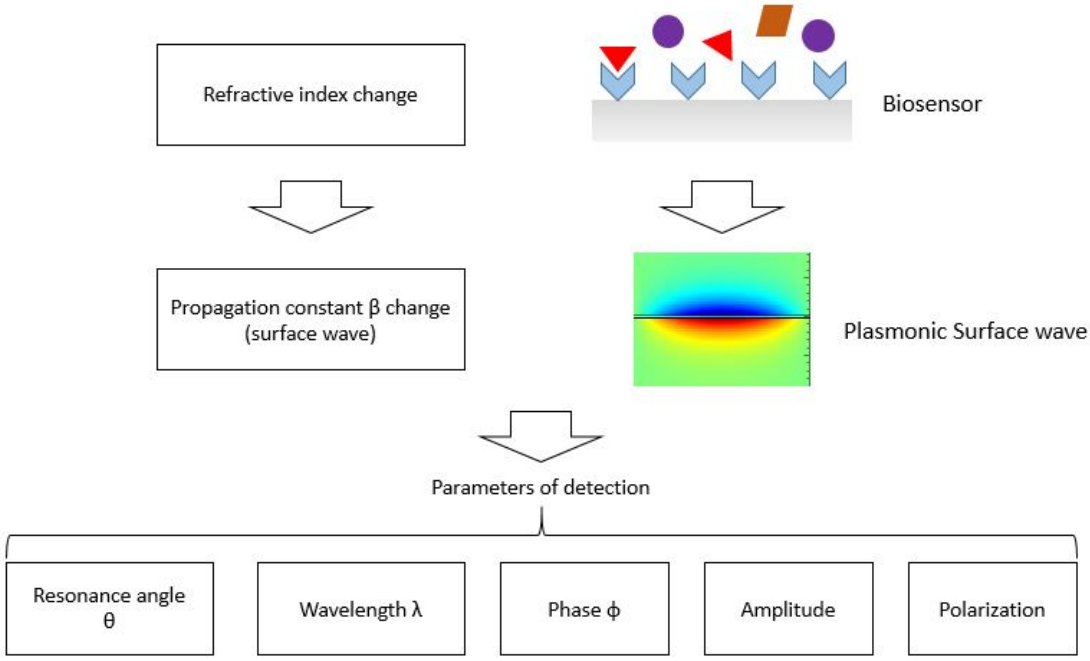

Figura 2.1 – Schematic SPR-based sensors.

2.1.1 Electromagnetics of metals

The first approximation to study the plasmonic resonance is to address the interaction of the electromagnetic waves with metals. The properties of metals can be approached by a *plasma model*, where a gas of free electrons oscillates on a fixed background of positives ion cores.

In response to an external electric field $\mathbf{E}$, the motion for an electron of the plasma is defined by (Stefan Maier, 2007):

$$m\ddot{\mathbf{x}} + m\gamma\dot{\mathbf{x}} = -e\mathbf{E} \tag{2.1}$$

Where m is the effective mass of each electron, γ is the characteristic collision frequency which produces damped on the motion via collision inside the crystal network and e is the electron charge. At this point we are interested in the result for a time-harmonic field ($\mathbf{E}(t) = \mathbf{E}_0 e^{-j\omega t}$) and where the position has the same behavior. So, the position in function of time is given by

$$\mathbf{x}(t) = \frac{e}{m(\omega^2 + j\gamma\omega)}\mathbf{E}(t) \tag{2.2}$$

This displaced electrons contribute to the polarization $\mathbf{P} = -ne\mathbf{x}$, where n is

the electron density:

$$\mathbf{P} = -\frac{ne^2}{m(\omega^2 + j\gamma\omega)}\mathbf{E} \tag{2.3}$$

Substituting this expression in the constitutive relations, we can find the dielectric function of the free electron gas:

$$\varepsilon(\omega) = 1 - \frac{\omega_p^2}{\omega^2 + j\gamma\omega} \tag{2.4}$$

where the real part of this dielectric function is responsible for polarization and imaginary part is responsible for losses. $\omega_p^2 = ne^2/(\varepsilon_0 m)$ is the *plasma frequency* of the free electron gas. Let's consider two limiting cases:

$$\varepsilon \approx 1 - \frac{\omega_p^2}{\omega^2} + j\frac{\gamma}{\omega}\frac{\omega_p^2}{\omega^2}, \quad \omega \gg \gamma \tag{2.5}$$

$$\varepsilon \approx 1 - \frac{\omega_p^2}{\gamma^2} + j\frac{\omega_p^2}{\gamma\omega^2}, \quad \omega \ll \gamma \tag{2.6}$$

In the high frequency limit, Eq. 2.5, we can see that the imaginary part is proportional to inverse of ω^3, so ε is predominantly real. When ω is much less than the collision frequency, the real part is a constant, it doesn't depend on the frequency, and the imaginary part is proportional to $1/\omega^2$.

In order to have good plasmonic materials we need a high frequency, because at high frequency the imaginary part of permittivity is quite small (low loss) but on the other hand, in for retain the metallic character of the material, the frequency should be less than the plasma frequency. It means that for good plasmonic materials we should be between γ and ω_p.

The dielectric function of the free electron gas Eq. 2.4 is thus also known as the Drude model of the optical response of metals.

2.1.2 Surface Plasmon Polaritons at single interface

Surface plasmon polaritons are electromagnetic waves evanescently confined at the interface between, in the simplest case, a dielectric and a conductor. These electromagnetic waves arise via the coupling of the electromagnetic fields to oscillations of the conductor's electron plasma. The term *polariton* means a hybrid wave with energy contributed by two parts. One part is the pure electromagnetic energy accumulated in the electric and magnetic fields, and the second part is the energy of solid state.

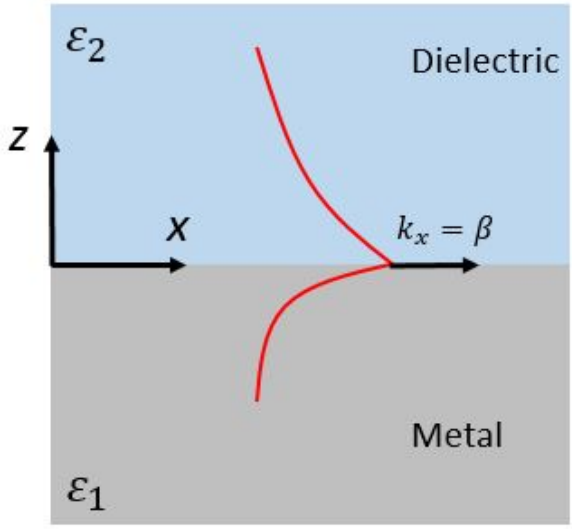

Figura 2.2 – Surface plasmon polariton (SPP) is a surface electromagnetic wave propagating along the metal-dielectric interface.

The problem we need to solve is, since the schematic shown in Fig. 2.2, to find the distribution of electric and magnetic field and the dispersion, it means the dependence of frequency of surface plasmon polariton on propagation constant β.

We start from the situation of absence of external sources and charges, to perform the modal analysis and solve the wave equation from the conditions of a metal-dielectric interface. From Fig. 2.2 we can describe the electrical field as $\mathbf{E}(x, y, z) = \mathbf{E}(z)e^{j\beta x}$. The following expression is arrived for the wave equation:

$$\frac{\partial^2 \mathbf{E}(z)}{\partial z^2} + (k_0^2 \varepsilon - \beta^2)\mathbf{E} = 0 \tag{2.7}$$

Where $\beta = k_x$ is called the *propagation constant* of the travelling waves and corresponds to the component of the wave vector in the direction of propagation. This equation is applied separately in regions of constant ε, and the obtained solutions will be matched using the boundary conditions. A similar equation of Eq. 2.7 exists for the magnetic field $\mathbf{H}$.

In order to explicit the field profile for $\mathbf{E}$ and $\mathbf{H}$, will be used the curl expressions of Maxwell equations. From this and taking into account that propagation is on x-direction ($\frac{\partial}{\partial x} = j\beta$) and homogeneity in the y-direction ($\frac{\partial}{\partial x} = 0$), the system of equation simplifies to independent and self-consistent solutions shown on Table 2.1.

For **TM** modes, the E_x and E_z expressions are in function of H_y while H_y corresponds to the solution of the wave equation of form as Eq. 2.7, for the magnetic field. Analogously, for **TE** modes, the H_x and H_z are in function of E_y.

From here, we proceed to solve the field profiles for each of the regions, dielectric and metal. Let us first look at **TM** solutions. We have the field profiles expressed on Table 2.2

The boundary condition of continuity of the electric and magnetic field in the interface allows to establish that $A_1 = A_2$ and

$$\frac{k_2}{k_1} = -\frac{\varepsilon_2}{\varepsilon_1} \tag{2.8}$$

Since k_1 and k_2 are positive, from the expressions shown in Table 2.2, the existence of the surface wave demands that $\varepsilon_1\varepsilon_2 < 0$, which happens at interfaces between materials with opposite sign of the real part of their dielectric permitivities, i.e. between a conductor and an insulator.

We take into account the expression for the propagation constant of the wave in each region:

$$k_1^2 = \beta^2 - k_0^2\varepsilon_1 \tag{2.9}$$

$$k_2^2 = \beta^2 - k_0^2\varepsilon_2 \tag{2.10}$$

Replacing Eq. 2.8 on Eqs. 2.9 and 2.11 we can obtain the dispersion relation of

Tabela 2.1 – Two sets of polarizations as a solution to the wave equation.

TM or p modes	TE or s modes
$\frac{\partial E_x}{\partial z} - j\beta E_z = j\omega\mu_0 H_y$	$\frac{\partial E_y}{\partial z} = -j\omega\mu_0 H_x$
$\frac{\partial H_y}{\partial z} = j\omega\varepsilon_0\varepsilon E_x$	$j\beta E_y = j\omega\mu_0 H_z$
$j\beta H_y = -j\omega\varepsilon_0\varepsilon E_z$	$\frac{\partial H_x}{\partial z} - j\beta H_z = -j\omega\varepsilon_0\varepsilon E_y$

Tabela 2.2 – TM solutions of surface wave.

z>0	z<0
$H_y(z) = A_2 e^{j\beta x} e^{-k_2 z}$	$H_y(z) = A_1 e^{j\beta x} e^{k_1 z}$
$E_x(z) = jA_2 \frac{1}{\omega\varepsilon_0\varepsilon_2} k_2 e^{j\beta x} e^{-k_2 z}$	$E_x(z) = -jA_1 \frac{1}{\omega\varepsilon_0\varepsilon_1} k_1 e^{j\beta x} e^{k_1 z}$
$E_z(z) = -A_2 \frac{\beta}{\omega\varepsilon_0\varepsilon_2} e^{j\beta x} e^{-k_2 z}$	$E_z(z) = -A_1 \frac{\beta}{\omega\varepsilon_0\varepsilon_1} e^{j\beta x} e^{k_1 z}$

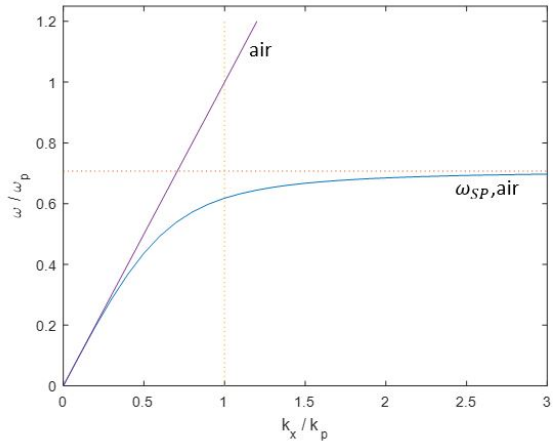

Figura 2.3 – SPP dispersion relationship.

SPPs propagating at the interface between the two half spaces:

$$\beta = k_0 \sqrt{\frac{\varepsilon_1 \varepsilon_2}{\varepsilon_1 + \varepsilon_2}} \tag{2.11}$$

Since confinement to the surface requires $Re[k_1] > 0$ and $Re[k_2] > 0$, this condition is only fulfilled if $A_1 = 0$, so that also $A_2 = A_1 = 0$. Thus, no surface modes exist for **TE** polarization and surface plasmon polaritons only exist for **TM** polarization. Exist some exceptions for the case of materials where the magnetic permeability is no constant like metamaterials, which are artificially designed materials.

Dispersion relation of SPP is depicted in Fig. 2.3. Due to their surface nature, the SPP excitations correspond to the part of the dispersion curves lying at right of respective light line of air or vacuum. Thus, special phase-matching techniques such as grating or prism coupling are required for their excitation.

2.2 Review of plasmonic sensors

2.2.1 Plasmonic sensors based on prism coupling

First configurations based on prism coupling for SPR were proposed, near to simultaneously by Otto (OTTO, 1968) and Kretschmann (KRETSCHMANN; RAETHER, 1968), which designs are based on the Frustrated - Total Internal Reflection principle (ORFANIDIS, 2016).

The use of the prism, as a medium with a higher refractive index, allows achieving a greater moment to the incident photons, in such a way that it is possible to comply with the phase matching between the component parallel to the interface,

of the incident wave, with the vector wave pattern of the characteristic plasmon of the metal/dielectric interface.

This coupling principle has been fundamental for the development of the first SPR sensor and today they can be considered as the most consolidated in the field, conforming the detection principle of the main SPR sensor setups in the market (Medina Escuela, 2011; Richard B. M. Schasfoort, 2017)

Between the main SPR setups from these companies there is the Biacore 8K+ as high-sensitive SPR system presented as suitable for screening, characterization, process optimization and quality control. This station, with more than 140 kg weight, works in the refractive index range from 1.33 to 1.39, eight channels for insertion microfluidics, minimal volume samples from 20 to 50 μL and automation for work for more than 70 h in unattended operation. Similarly, in BioNavis company, we can find other models like the MP-SPR Navi 400 KONTIO, specially designed to measure cell adhesion and cell-based interactions. In this case, the station work has 4-channel flow-cell, two independents wavelength measurements from each channel, wide angular range (40-78°), control over the liquid flow. (CYTIVA, 2020; CYTIVA/BIACORE, 2022)

These equipments are basically developed to be used in sophisticated laboratory benches due to cost, design no oriented to portability and that involves trained personnel. Taking into account these limitations, both other commercial proposals and academic developments have been developed to overcome them. One of these proposals is the Spreeta 2000 (CHINOWSKY et al., 2003), which is based on prism coupling to guarantee a compact device focused on portability and easy to use in areas outside the laboratory. Developed by TI and Prolinx Inc., this device integrate all of the optical and electronic components for implementing SPR biosensor in a plastic package in the order of centimeters.

With the same objective of promoting the use of SPR in a portable and user-friendly way, several research groups have developed innovations in the Kretschmann design that allow them to maintain their benefits, combining them with miniaturized, portable and/or low-cost configurations. One of these developments has been taking place at the University of Campina Grande (UFCG) in Brazil, where Biosensor's Laboratory works with SPR configurations based on home-made prisms (MOREIRA et al., 2010).

Taking advantage of the simplicity of the angular sweep mechanical principle in the Kretschmann setup, in this work (LAKSONO et al., 2018) is developed a low-cost setup using Arduino and gears achieving an angular resolution angle of incidence laser up to 0.01° and were tested the angles for total internal reflection and plasmonic resonance in the interface gold/air with high accurate.

On the side of integration of plasmonic sensors using prisms, the attempts to couple with cellphones stand out, which allow the use of the flashlight as a source and

the camera to capture the data. One of the first prototypes presented is described in (PREECHABURANA et al., 2012), where from a PDMS structure it is possible to couple a prism to a cellphone that, through the source and the camera, can perform a diagnosis by intensity. Along the same lines, in (FALQUETO, 2019), work is being done on the integration of the PPBIO prism adapted at the UFCG with a smartphone, being able to work in the angular or spectral interrogation mode. This type of development keeps the line of exploration open in structures that can be portable enough to carry out diagnoses in remote areas using mobile phones.

2.2.2 Plasmonic sensors based on waveguide coupling

Parallel to the use of fiber optics as a platform for plasmonic sensors, the use of waveguides on planar substrates began to generate interest. Benefits such as miniaturization, integration, multiplexing capability, and the emergence of the Lab on a Chip concept were supported by new advances in the fields of microfabrication, microfluidics components, and materials.

Within the field of waveguide-based plasmonic sensors, we can find two types in the literature: those that use waveguides by deposition of thin metallic and dielectric films on a high-index prism (WANG et al., 2018b; LEE et al., 2010) and those that they use the waveguide as a means of transporting the light from the source, feeding the sensor plasmonic structure (ČTYROKÝ et al., 1999; LAVERS; WILKINSON, 1994). In this section we will focus on the latter.

The type of waveguide-based plasmonic sensors works mainly with a spectral interrogation system, which allows to identify the plasmonic resonance through a guide structure that excites the plasmon at the sensor interface. From the change in the refractive index and the consequent plasmonic wave vector, the resonance wavelength will indicate the change. In (DEBACKERE et al., 2006; HOMOLA, 2006a) guide structures are indicated where the metal surface is in direct contact with the core of the guide. These induce high losses but allow monitoring and multiplexing of the sensor capacity. In (ALAM, 2012) structures that work with an intermediate layer of lower index are presented, which allow reducing the level of loss and also allow spectral monitoring. The latter are the most discussed in Chapter 4.

2.2.3 Plasmonic sensors based on optical fibers

While the feasibility of using plasmonic sensors appeared together with prism coupling, it has been the use of optical fibers as a substrate for resonance production that has sparked a vast stream of development in the plasmon sensor field. Literally, hundreds of works by research groups throughout the world can be mentioned that have

contributed to the use of optical fibers in plasmonic resonance detection devices from different perspectives, coating, multi-detection, miniaturization, sensitivity improvement, remote monitoring, among others.

In this section will be describe in short the main trends in the plasmonic sensors using fibers as substrate. With this goal have been development a variety of tehcniques, among which we can mention:

- D-shape fibers. From the polishing of fibers, it is possible to expose part of the fiber core that can be metallized and that allows to have high sensitivity conditions.
- Etching techniques for remove claddings. From a chemical attack it is possible to remove the cladding from the fiber to fully expose the core, this being generally of the multimode type. The metallization of this surface, which presents a challenge due to its cylindrical structure, allows the production of plasmons at the metal-sample interface that can be used as a sensor structure under the intensity interrogation scheme.
- Tapers. From a controlled reduction in the diameter of the fiber it is possible to use the evanescent wave as a means of excitation of plasmons in contact with an external medium. As in the previous cases, this technique works under the spectral interrogation detection scheme.

Additionally, in (ZHAO et al., 2019) is pointed the use of plasmonic sensors on fibers based grating structures. These configurations allow to keep intact the cladding or structure of the fiber, modifying only the refractive index of the nucleus periodically, using techniques such as holography. This condition produces an adequate reflection to the propagating light in the nucleus that allows the cladding to be reflected and interact with a metallic interface for plasmonic sensing.

3 KRETSCHMANN CONFIGURATION-BASED SPR SENSOR

The most common method for the excitation of surface plasmons today is the method based on the phenomenon of attenuated total reflection (ATR) method. This configuration requires a medium with a higher optical index than that of air (generally a prism) to excite a propagating plasmonic wave between a metallic surface and a medium under analysis, fulfilling the phase matching conditions mentioned in chapter 2. There are two possible configurations for the ATR method: the Otto configuration (OTTO, 1968) and the Kretschmann configuration (KRETSCHMANN; RAETHER, 1968). Figure 3.1 shows the scheme of both configurations.

While the Otto configuration has become a tool in surface quality analysis (Stefan Maier, 2007; LEE et al., 2018), the Kretschmann configuration is the first alternative for most commercial SPR sensor implementations (Richard B. M. Schasfoort, 2017; BRASIL; RODRIGUES; PEREIRA, 2019; PANDEY; RAGHUWANSHI; KUMAR, 2022).

Using the Kretschmann configuration there are several options to monitor the change in index of the medium to be sensed. The way in which this monitoring is carried out is called the interrogation or modulation method, which are described in (HOMOLA, 2006a). In this chapter the two implemented and tested methods are discussed: plasmonic resonance detection using angular interrogation and intensity interrogation.

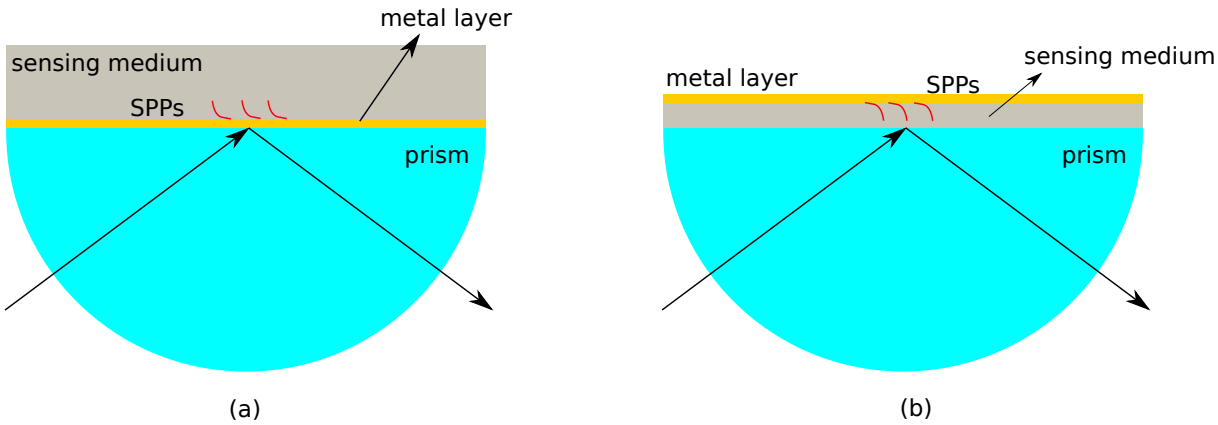

Figura 3.1 – (a) Kretschmann configuration, the metal layer is placed in direct contact with the prism, (b) Otto configuration, the metal sheet is separated from the prism by the medium to be sensed. In both schemes, the SPPs (surface plasmons polaritons) are generated at the metal-medium interface to be sensed.

3.1 Sensing by angle interrogation

The scheme of this setup is shown in Figure 3.2. It is based on a $\theta/2\theta$ rotation system that is controlled by a step motor model KTC-5017-008 (KALATEC, 2022) controlled by an Arduino which, in turn, is managed by a user from a human-computer interface developed in Python. Like any angular detection system, the levels of mechanical and electronic noise must be adequately characterized, controlled and reduced. The sensitivity and detection limit of the system under tests of ethanol-fuel concentrations are presented.

3.1.1 Optical configuration

Source

A laser cannon model HNL050LB HeNe (Thorlabs) is used as source (THORLABS, 2022b), with a nominal operating wavelength of 632.8 nm, an output power of $5mW$ and linear polarization. In order to control the power at the prism input, a variable attenuator is used (model NDC-50C-4M by Thorlabs (THORLABS, 2022d), in addition to an optical isolator (model IOT-3D-633-VLP by Thorlabs (THORLABS, 2022c)) to avoid any harmful reflection to the source and maintain the polarization.

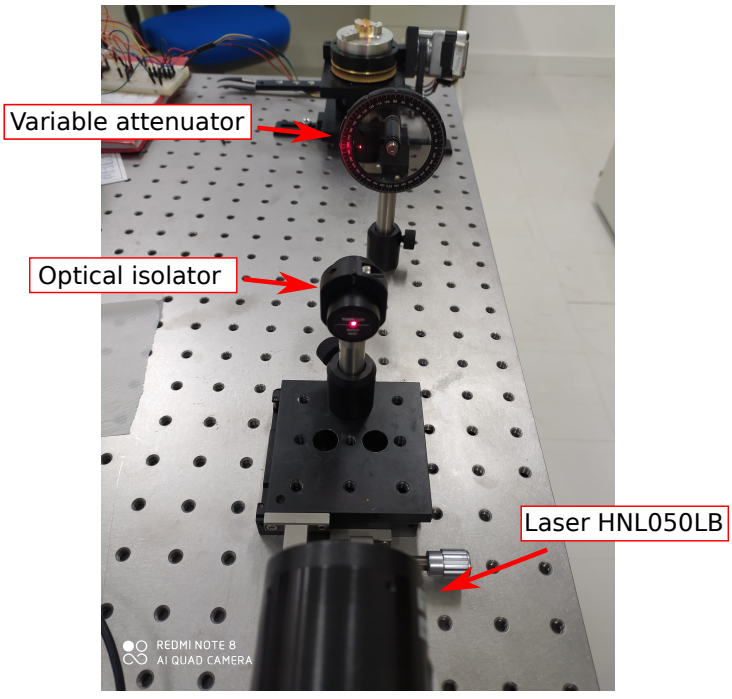

Figura 3.2 – Photo of the laser, optical isolator and variable attenuator, elements to regulate the optical power that incides the prism.

Prism

The optical prism used is semi-cylindrical in shape from the FOCtek (FOCTEK, 2022) and is made of BK7 material. This material is a type of high quality optical

borosilicate glass developed for high precision experiments and instruments (Glass Dynamics, 2022).

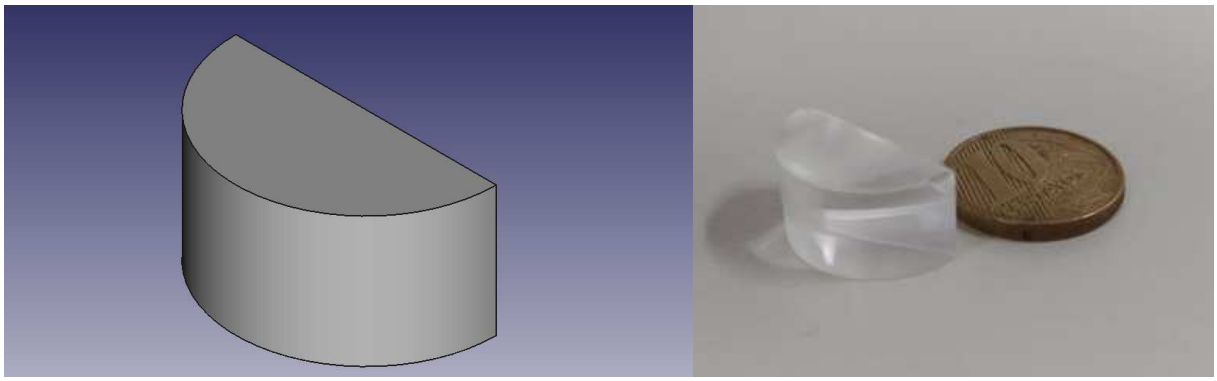

Figura 3.3 – (a) Schematic of the semicircular prism used (FreeCAD). (b) Photo of the 1cm diameter prism together with a 10-centavo coin.

Gold layer

The gold layers were manufactured from the metallization of commercial circular glass slides of 13 mm diameter and with a standard thickness between 130 and 170μm. The material of these slides is borosilicate glass and they were purchased from (SPLAB, 2022). The metallic deposition was carried out by the high vacuum evaporator model ULS400 by Balzers, at the Device Research Laboratory - IFGW (IFGW, 2022). Several metallic depositions were made with thicknesses of 2 to 4 nm of Titanium (as adhesion layer) followed by 50 nm of gold.

The next step is to identify the efficiency of the gold layers and prism, under the real conditions imposed by the components and background noise (laboratory environment). Thus, the percentage of reflection of the optical power has been captured for different values of incident power, obtained from the manipulation of the variable optical attenuator. The angle of incidence is 55°, outside the resonance condition for the gold/air interface. The values obtained are compiled in Table 3.1.

As shown in Fig. 3.7, the sheets show a fairly similar behavior, although less than expected, which is 80%. The deduction of the theoretical power is obtained through the implementation in Matlab of the conditions of oblique incidence in multilayer substrates, for which use is made of the material made available by Sofocles Orfanidis (ORFANIDIS, 2016).

The photodetector circuit is responsible for capturing the reflected optical signal and taking it to a voltage reading in an input port of the Arduino board. As a first step, we capture the reflected power with the Optical Power Meter with different angles of incidence of the laser to know the optical power that will affect the photodiode and the efficiency of the plasmonic resonance in terms of power.

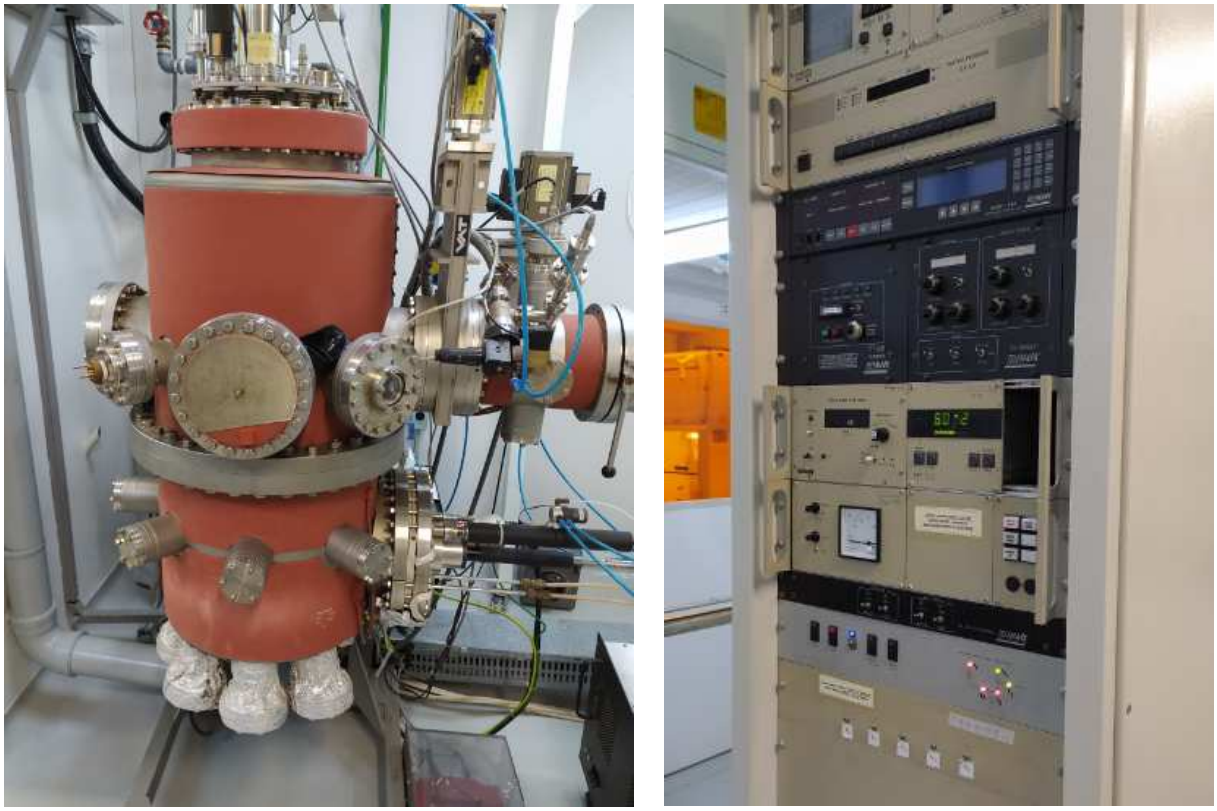

(a) (b)

Figura 3.4 – (a) High vacuum induction chamber for deposition of thin films by evaporation. (b) Camera control equipment. Both equipments are at the Devices Research Laboratory (DFA-IFGW).

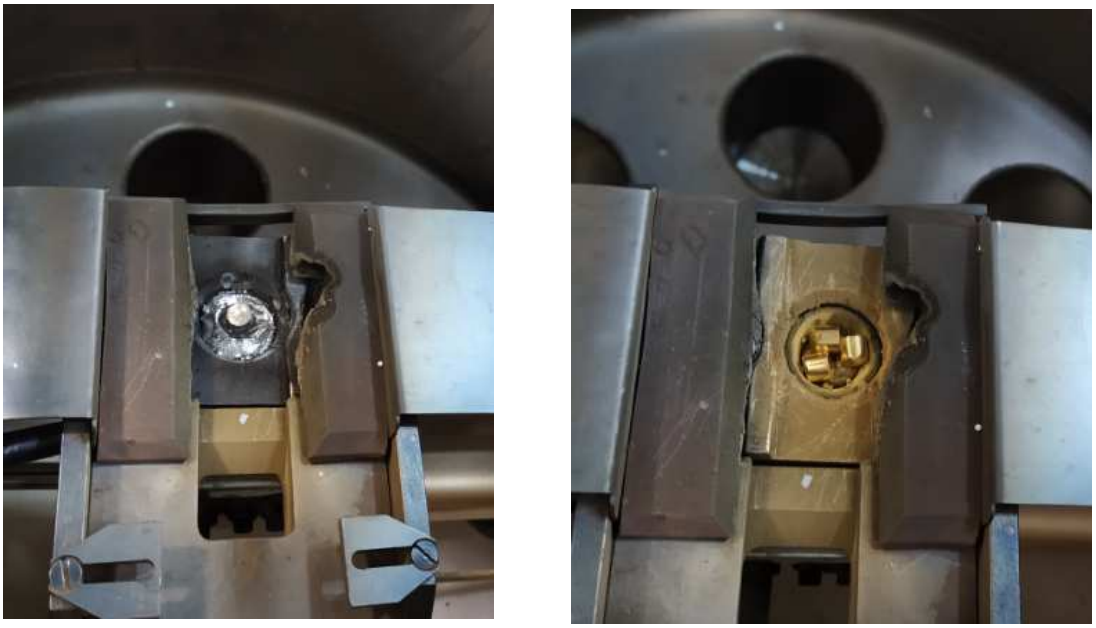

(a) (b)

Figura 3.5 – (a) Titanium sample with 99.9999% purity in the chamber. (b) Gold sample with 99.9999% purity.

Figura 3.6 – Borosilicate glass substrate used for gold deposition.

Sample	Input Power (mW)	Reflected Power (mW)	Reflectance (%)
S1	1.06	0.56	52.83
S1	2.07	1.07	51.69
S1	3.06	1.55	50.65
S1	4.05	2.05	50.61
S2	1.03	0.55	53.39
S2	2.07	1.08	52.17
S2	3.08	1.63	52.92
S2	3.99	2.13	53.38
S3	1.04	0.54	51.92
S3	2.05	1.05	51.21
S3	3.02	1.58	52.31
S3	3.95	2.05	51.81
S4	1.06	0.55	51.88
S4	2.04	1.04	50.98
S4	3.07	1.57	51.14
S4	3.96	2.02	51.01
S5	1.00	0.48	48.00
S5	2.01	0.97	48.25
S5	3.01	1.43	47.50
S5	4.02	1.93	48.01
S6	1.05	0.55	52.38
S6	2.03	1.06	52.21
S6	3.04	1.58	51.97
S6	4.00	2.09	52.00

Tabela 3.1 – Incident and reflected power values of the prism-gold layer structure with the HNL050LB laser.

Fig. 3.8 shows the reflected power for a range of incidence angles from 35 to 55 degrees, using water as the sensing medium. The PM400 power meter allows the capture

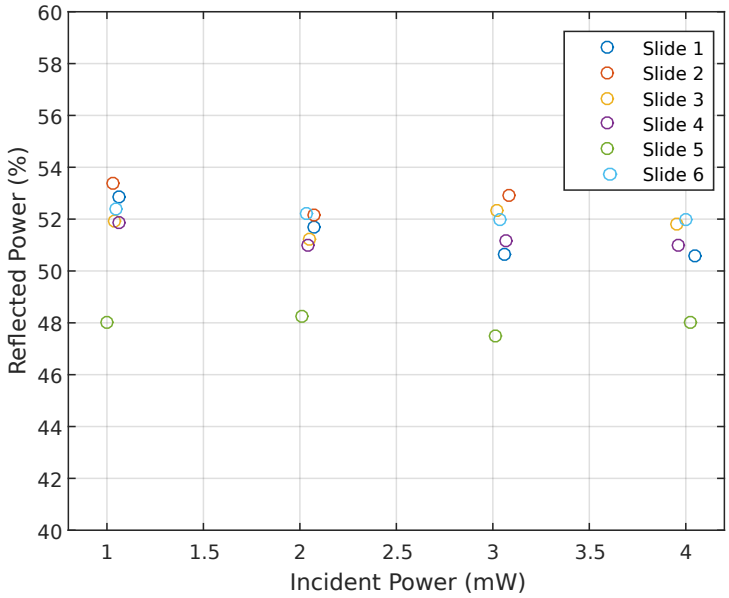

Figura 3.7 – Reflectance percentages for each sample for different incident power values.

recording option in the time domain, with an approximate resolution of 10 ms per sample, so captures have been made in a range of approximately 160 s, the time it takes for the system to turn the specified angular range. As we can see from Fig 3.8 (a) and (b), the reflection and plasmonic resonance behavior is independent of the incident power, reaching a resonance power of approximately 30% of the maximum reflected power.

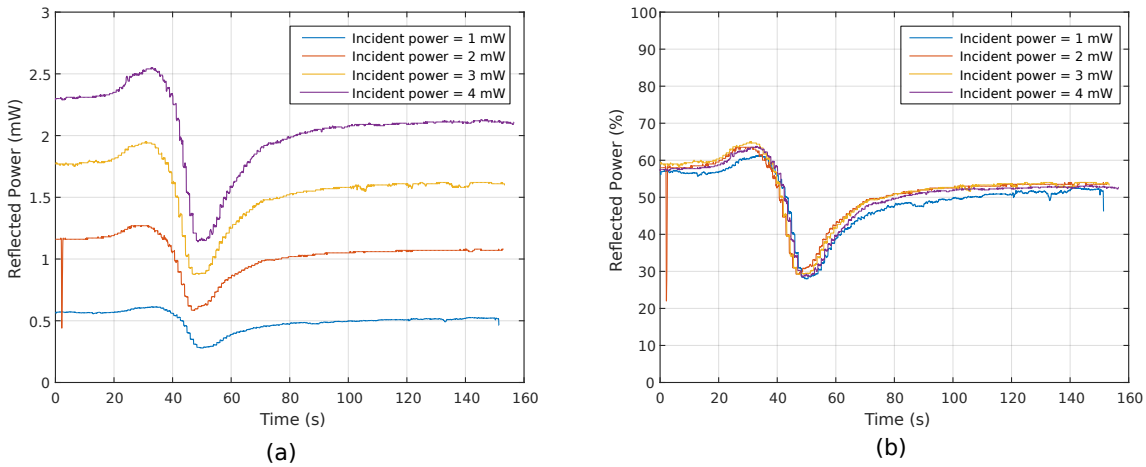

Figura 3.8 – Reflected optical power captured by the Power Meter versus time. The analyzed range is from 35 to 55° for incident angle. The power meter captures the power for a given range of time, so the x-axis represents time in seconds. All cases use the same gold slide.(a) Absolute values. (b) Relative values.

Photodetector

The photodetection electronic circuit must allow the optical power behavior to be transferred to equivalent voltage values at the Arduino input port. The photodetector

used is by Hamamatsu model S5870 Si PIN photodiode (HAMAMATSU, 2022). For the electronic design, the following must be taken into account:

- Using the Arduino board, we have a $5V$ DC source available, in addition, since our objective is sensing, we will use one of the analog input ports, which capture voltage values between 0 to $5V$ encoded with 10 bits, for which has 1023 levels of reading, with a resolution of $4.9mV$.
- We have a maximum incident power to the photodetector of $2.6mW$, considering an incident laser power to the prism of $4mW$.

Based on these restrictions, an **R1** value of 5 $KOhms$ has been reached, so the reading circuit is as shown in Fig. 3.9.

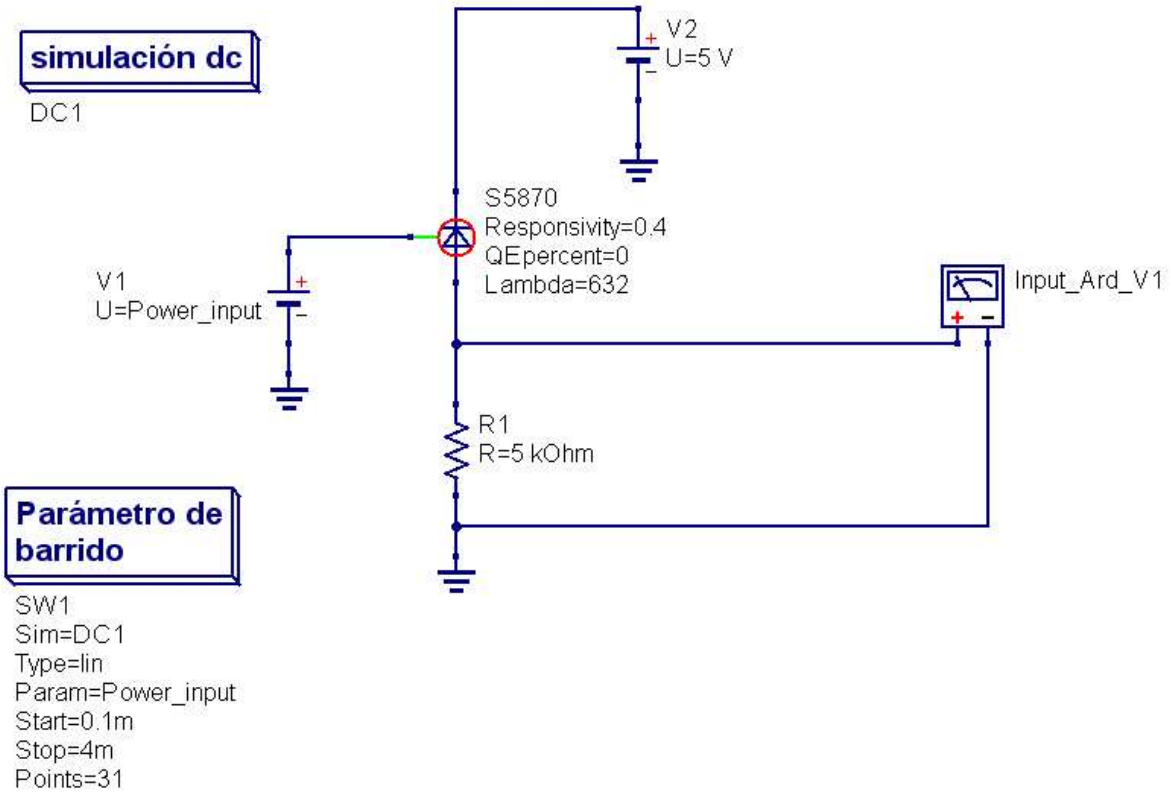

Figura 3.9 – Photodetection circuit. The 5 V supply voltage is given by the Arduino power port. The reading from **R1** goes to one of the analog input ports.

The values of the voltage on **R1**, read by the analog input port, for different values of the incident optical power **U**, are shown in Fig. 3.10.

We can see in Fig. 3.10 that the voltage values at read port (A5) have a linear behavior up to an input value of 2.8 mW. From this value, the voltage remains constant, because the photodiode is no longer polarized in its operating region. With incident power values between 0.1 and 2.5 mW, a linear behavior in the voltage is observed, between 0 to

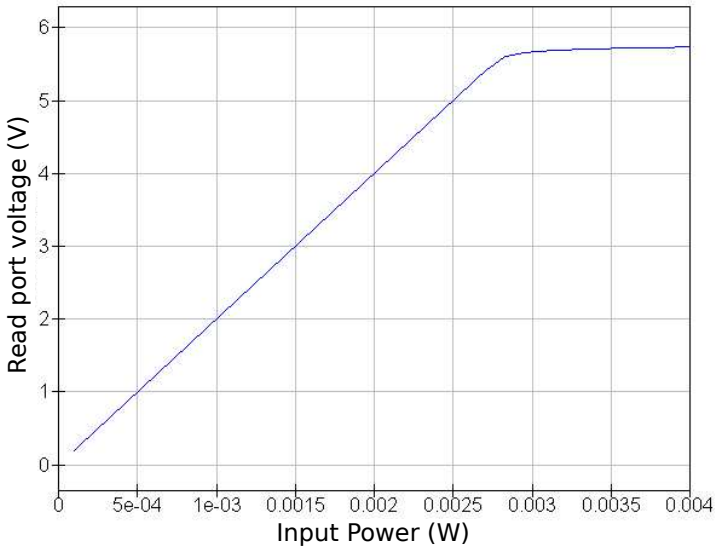

Figura 3.10 – Photodetection circuit. The 5 V supply voltage is given by the Arduino power port. The reading from **R1** goes to one of the analog input ports.

$5V$. Due to the fact that with 2.5 mW a voltage value of 5 V is reached at the input, and this will be the maximum reading limit at the input port, it has been decided to work with an incident laser power of 3 mW, which according to the Fig. 3.8 reflects optical power values between 0.8 to 2 mW, which generate a voltage at the input port between 1.3 to 4 V, in the region of linear behavior.

There is another important aspect to take into account, especially for high-speed signal acquisition systems, which is the impact of the junction capacitance of the photodetector. The capacitive effect formed at the PN junction of the photodetector limits the response speed of the device, and is discussed in some detail in (Medina Escuela, 2011) for its unique photodiode sensor design. To calculate how much this parameter limits the response speed in our setup, we take into account the values of the datasheet of our device. As stated in (HAMAMATSU, 2022) the model S5870 photodetector has a terminal capacitance of 100 pF, for a reverse voltage of 5 V, while we maintain a 5 $KOhm$ resistor as shown in the circuit model of the photodetector.

This allows us to calculate the time constant (τ) of the device expressed by Eq. 3.2:

$$\tau = R * C \tag{3.1}$$

Being τ the time both for charging to reach 63.21% of the total charge and in the case of downloading to decrease to 36.78% of the initial charge. For practical reasons, 10τ is taken as the total charge or discharge time of the junction capacitor of our photodiode. In this way, a time of 20τ is the time that we assume as a minimum for the

photodetector to perform a single reading.

$$MRT = 20 * \tau = 10useg \tag{3.2}$$

Where MRT represents the Minimum Reading Time that photodetector used takes to pick up a single value of intensity.

3.1.2 Microfluidics

Microfluidic circuits made on PDMS substrate manufactured in the Microfabrication Laboratory of the CNPEM, with dimensions of 1x1 cm and channels with a depth of 50μm and 6 mm extension, have been used. Figure 3.11(a) presents the FreeCAD design of the fabricated structure, while Fig 3.11(b) presents a photo with the detail of the microfluidic channel.

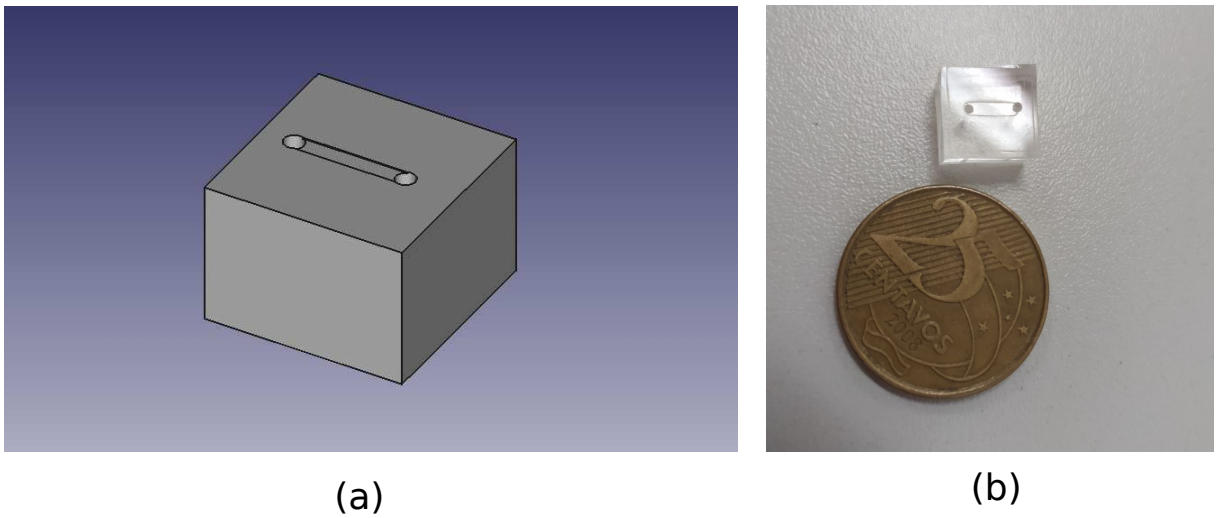

Figura 3.11 – (a) Schematic microfluidic chip in PDMS. (b) Photo of the PDMS chip with a side of 1 cm and a channel of 50μm depth together with a 25-cent coin.

Microfluidic hoses of 1 mm diameter are used and inserted into the PDMS microchannels. A hose is connected to a 10 mL syringe installed in an infusion pump, model UNK-SP-2014 by UHNICA (METALVET, 2022). This infusion pump allows us to introduce the fluid in a controlled way, generating a laminar flow that covers the entire microfluidic channel. The other hose is for the fluid outlet and is placed on a disposable fluid collection container.

3.1.3 Rotation system and data capture

The angular scanning system is based on the well-known $\theta/2\theta$ rotation platform. This platform allows two parallel planes to rotate with different angular speeds from the same axis of rotation. In this way, it is ideal for our application, since when we rotate the

prism θ degrees in relation to the incident light beam, it is required to rotate 2θ degrees the position of the photodetector to capture the reflected light. A photo of the system is shown in Fig. 3.12.

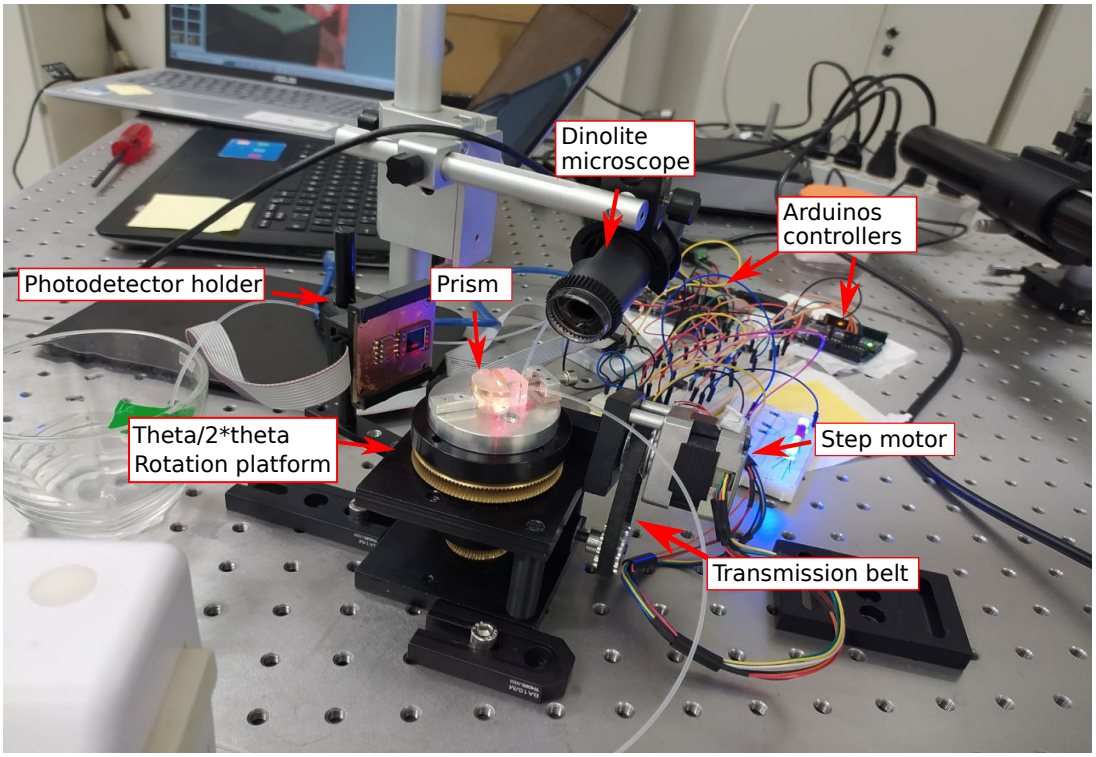

Figura 3.12 – Details of $\theta/2\theta$ rotation system and setup used in the angular interrogation system.

Table 3.2 presents the main mechanical characteristics of the rotation platform.

Dimensions	Side: 75 mm Height: 95 mm Height with prism: 105 mm
Weight	around 1 kg
Step motor	KTC-5017 008 (Kalatec)
Maximum resolution according developer	0.015°
Material	Metallic

Tabela 3.2 – Mechanical characteristics of rotation platform.

The electronically controlled mechanical rotation system was improved in two respects. First, the incorporation of plastic pieces of ABS material designed ad hoc and produced on a 3D printer. The second aspect has been the new programming of the Arduino controller for the immediate capture of reflected light intensity values, allowing parallel management of the stepping motor and the photodetector, which is impossible to achieve with serial management.

3D parts printing

The initial $\theta/2\theta$ rotation system was functional to our needs but had a limitation, which was the use of a gear timing belt with unconventional dimensions. With continuous testing, this strap broke and it was necessary to replace it with a conventional length, XL size, which is the shortest available on the market. This new belt implied a new distance between the gears of the system, which is why new posts were required under this demand. For this it was necessary to design and print 3D posts with $37mm$ length.

The LEMAC has a 3D printer, Ender 3 model, recently acquired that works with various types of filaments, including ABS and PLA. Both materials are quite common for different types of applications. Two pieces were designed: containment posts for the $\theta/2\theta$ system and a holder for the photodetector that allows better handling and positioning of the same during the experiment. The 3D printer, the designed and printed parts are shown in Fig. 3.13.

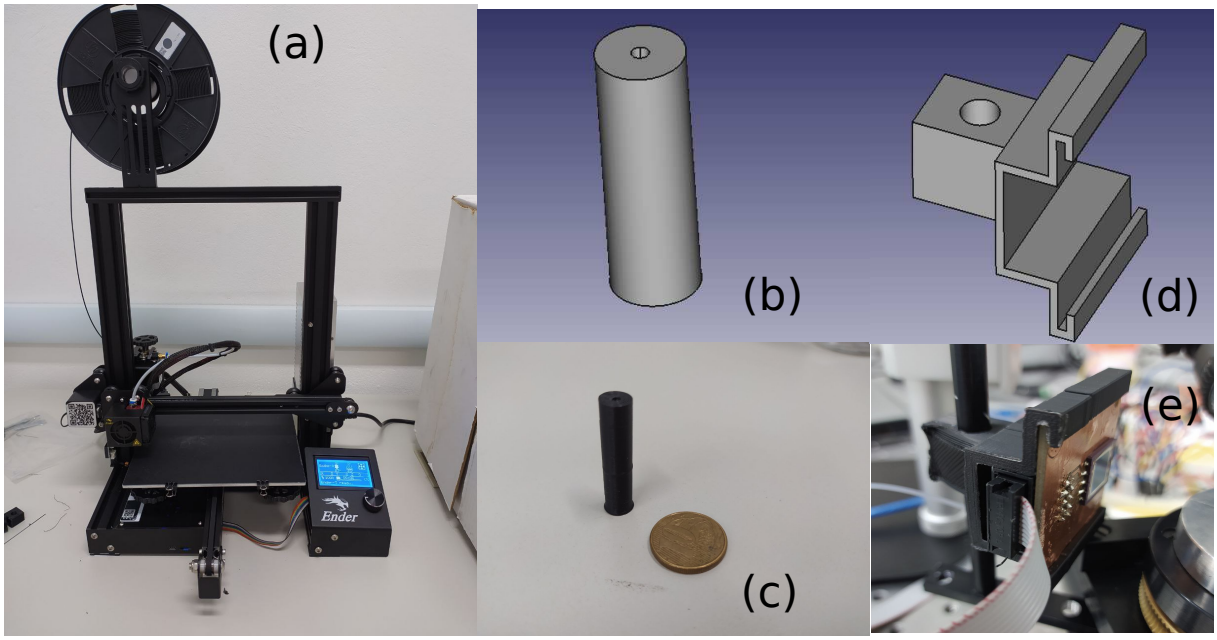

Figura 3.13 – (a) Ender 3 model 3D printer. (b) Design of column. (c) Column printed. (d) Photodetector holder design. (e) Holder printed. All cases use ABS material.

Parallel management of the stepper motor and photodetector

The stepping motor is controlled by an Arduino which in turn is managed by the human-computer interface developed in Python. In relation to data capture, this is done from the connection of the photodetector to the Arduino analog input port, as indicated in the previous subsection.

One of the main advantages of an SPR sensor is the real-time monitoring of the chemical bonds that affect the refractive index of the material in contact with the metal. To this end, it is necessary to have a high speed sweep of the system, in this case, a

sweep over a certain angular range. The initial setup, of a single serial controller to drive the stepper motor and photodetector, involved an angular displacement of the motor, followed by a reflected current capture, then re-rotate the motor a small enough angle (for example, 15 milligrades) to then capture the reflected intensity value. This required, for example, in the case of an angular sweep of 4 degrees, more than 260 successive steps. Due to mechanical impulses of the stepping motor, each step lasted more than 0.5 s, which implied a duration of more than 130 s to carry out the complete sweep. That is, capturing a single resonant angular position took 130 s.

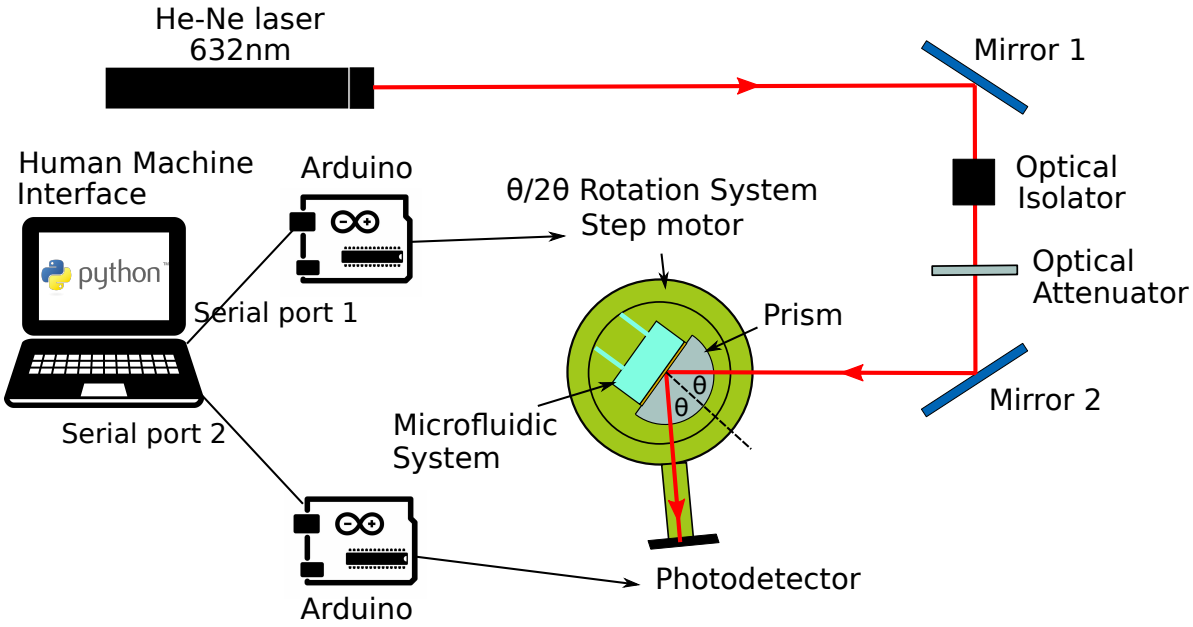

Figura 3.14 – Schematic of the optical setup. Two arduino controllers for parallel management are used.

In order to capture a series resonance curve, capturing the incident intensity on the photodetector simultaneously with the rotation of the motor, two Arduinos are required, which allow one to control the motor and the other to control the intensity capture, working synchronously. In this way, a time of approximately six seconds was chosen for an angular sweep of 10 degrees. Time in which the motor rotates at a speed of 100RPM as soon as the photodetector saves the captured values in an array. In this way, a single resonant angular position is obtained in more than 20 times less time.

The number of samples that the photodetector captures in this time range is 800 intensity values, which indicates an approximate time of 7.5 ms per sample. This is where the minimum time in which the photodetector used can distinguish a sample must be taken into account without the delay effect imposed by the parasitic capacitive effect characteristic of all PN junctions. As it was calculated in the previous subsection, related to the photodetector, this time is 10μs, which is much lower than the value we work with. This indicates that we can even reduce the capture time of the resonance curve, but for reasons of stability of the mechanical system, we have maintained this capture rate.

The schematic of this setup is shown in Fig. 3.14.

3.1.4 System management software

Two interfaces were developed for the management of the SPR system. The first is called "Resonance detection Interface" and allows capturing the reflected intensity curve for a certain angular range and the second interface is called "Tracking system interface", which allows capturing N intensity curves with the automatic detection of resonance position.

Resonance detection interface

This interface is aimed at capturing the resonance curve in order to recognize the best angular position of the system to start a subsequent resonance tracking process. The graphical user interface, showed in Fig. 3.15, was developed in Python and using the Tkinter packages.

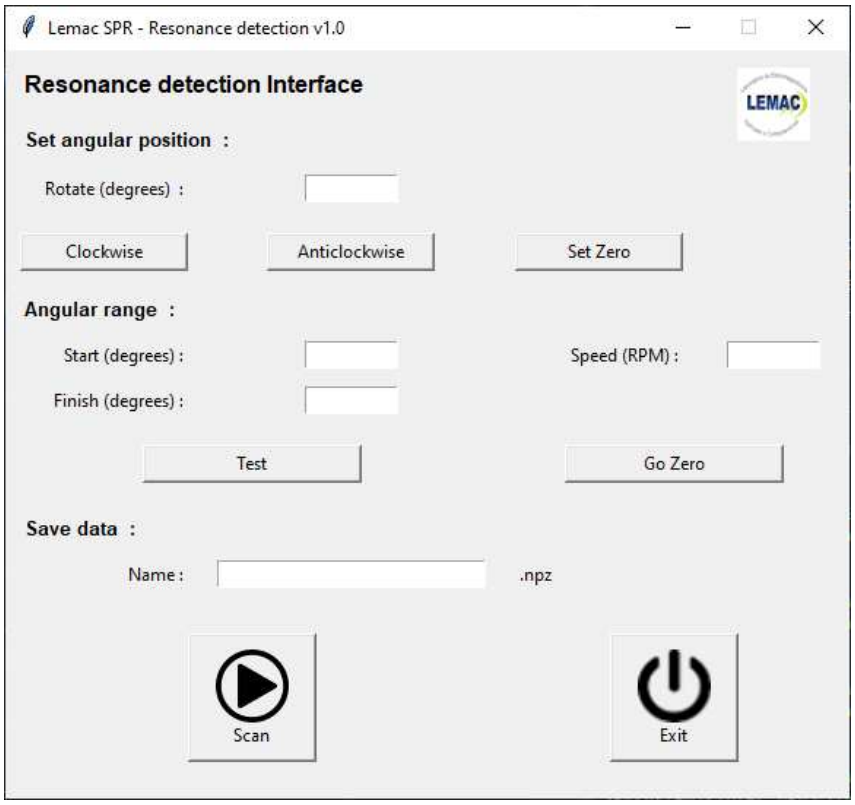

Figura 3.15 – GUI for resonance curve detection for certain angular range.

Each of the buttons and fields shown in Fig. 3.15 are described below.

- **Clockwise:** Captures the value inserted in the **Rotate (degrees)** field to rotate the system clockwise.
- **Anticlockwise:** Captures the value entered in the **Rotate (degrees)** field to rotate the system counterclockwise.

- **Set Zero:** Sets the current position as a relative position of “zero degrees”, formed between the incident light beam and the normal to the gold foil.
- **Test:** Performs a rotation from an angular position entered in the **Start (degrees)** field to the final position entered in the **Finish (degrees)** field at a rotation speed entered in the **Speed (RPM)** field.
- **Go Zero:** Go to the previously defined as "zero degrees"position.
- **Scan:** It captures the intensity that reaches the photodetector while the motor is rotating the system. All data is saved with the name inserted in the field "Name:"with the extension .npz.

Tracking system interface

This interface allows a capture of N reflectance curves. This sequence allows the identification of the change in the resonance angle over time. Fig. 3.17 presents a screenshot of the described interface.

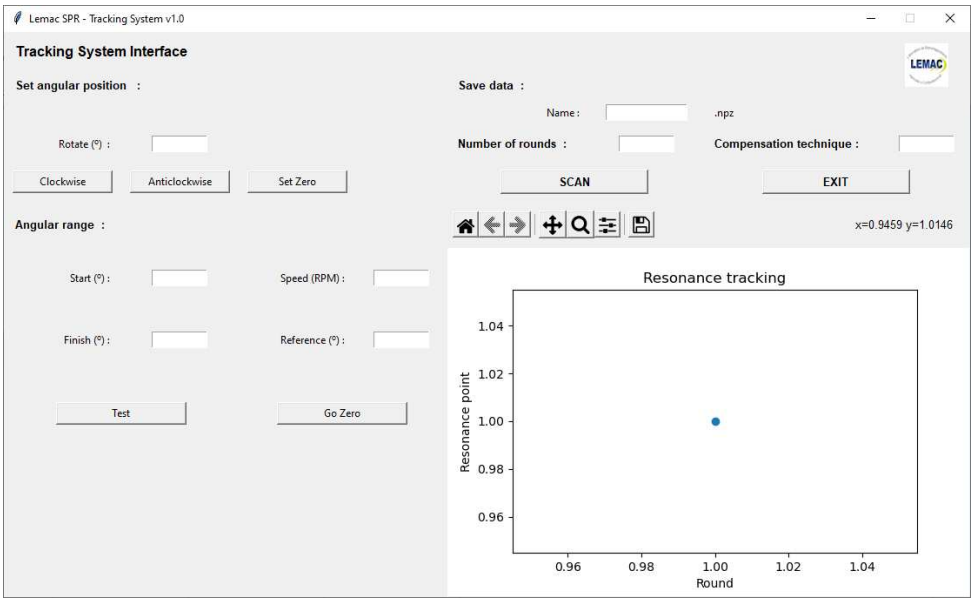

Figura 3.16 – GUI for the tracking resonance system.

The functionalities present in this interface are:

- **Clockwise:** Captures the value inserted in the **Rotate (°)** field to rotate the system clockwise.
- **Anticlockwise:** Captures the value entered in the **Rotate (°)** field to rotate the system counterclockwise.
- **Set Zero:** Sets the current position as a relative position of ’zero degrees’, formed between the incident light beam and the normal to the gold foil.

- **Test:** Performs a rotation from an angular position entered in the **Start (°)** field to the final position entered in the **Finish (°)** field at a rotation speed entered in the Speed field.
- **Go Zero:** Go to the previously defined as 'zero degrees' position.
- **Scan:** Performs N capture rounds of the captured reflectance curve. The number of rides is captured in the **Number of rounds** field, all captured curves are saved in the folder under the name inserted in the 'Name+i' field, where i is the round number and saved with the .npz extension. The graph inserted in the interface allows the resonance position to be followed in real time.

  In the 'Resonance tracking' graph are presented all the resonant points captured for each round (resonance curve) in real time.

3.1.5 Sensor characterization

The characterization of any sensor is established from the determination of its main parameters: Sensitivity, Full Width Half Minimum (FWHM), Figure of Merit and Limit of Detection (BIJALWAN; SINGH; RASTOGI, 2020; AKIB et al., 2021). These parameters allow us to know if the sensor has the capacity to resolve enough refractive index variations to meet a given application. Next, an analysis of the resonance curves and the sensorgram is carried out, for the particular case of mixtures of ethanol-fuel with water, describing the way in which the data is processed and the characteristics of the sensor are deduced.

Resonance curve

With the 'Resonance detection interface' we can capture the resonance curve of the sensor. As described in section 3.1.4, the angular range and the speed of rotation can be set. This rotation speed is taken into account to enable, in this period of time, the continuous capture of intensity values that reach the photodetector.

For example, after one round of data capture in a certain angular range, the curve shown in Fig. 3.17 is obtained.

Fig. 3.17 shows the resonance curve for the case of water in contact with gold foil, which occurs at approximately a 72 degree angle of incidence. It can be seen that the x-axis shows the variable *Points* which represents the number of intensity points captured in the photodetector. There are 848 points for the interval of 10 degrees of scanning, which is equivalent to an angular resolution of 0.012°. It is also possible to observe that there is a small level of noise in the intensity that accompanies the entire angular range and that it is mainly produced by the noise of the laser itself. Figs. 3.18(a) and (b) present the detail of the laser noise captured by the photodetector.

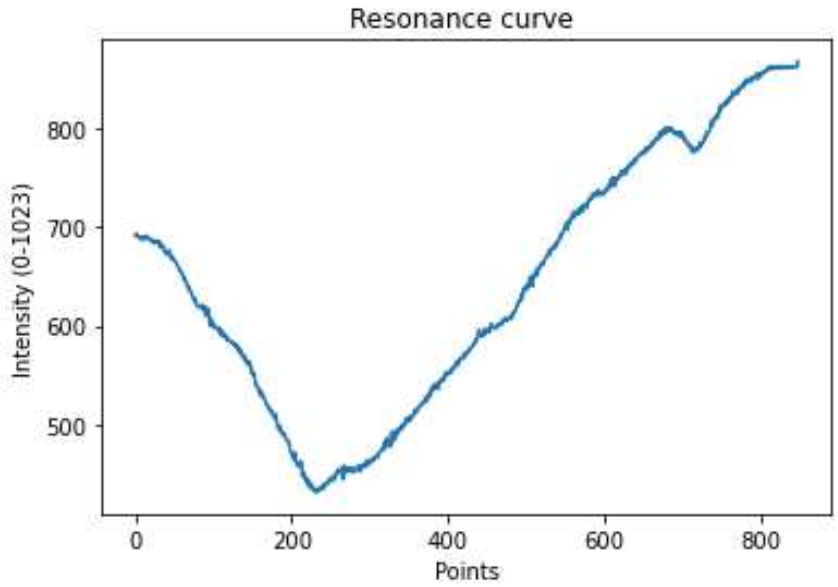

Figura 3.17 – Resonance curve captured with a 2 nm Ti and 50 nm gold slide, in contact with water via microfluidic channel.

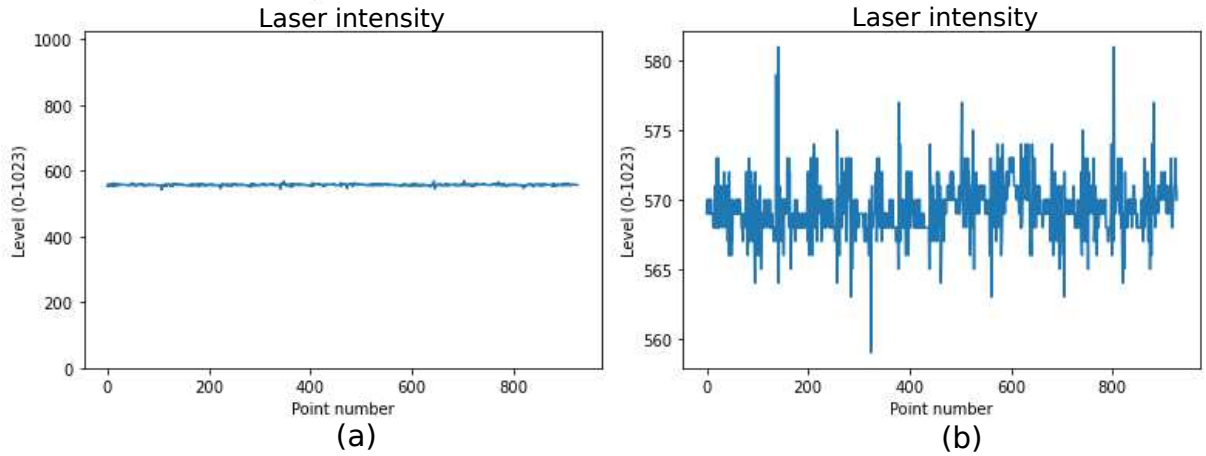

Figura 3.18 – (a) Attenuated intensity of the laser captured directly by the photodetector. Small power fluctuations can be observed. (b) Detail of laser power fluctuations.

These laser fluctuations impact the identification of the power minimum and the resonant angular position, which is based on monitoring this position to make a reliable diagnosis about the change in the refractive index of the sample. Figs. 3.19(a) and (b) show the impact of these fluctuations for the case of 20 repeated curves with the same conditions: same sample and same laser intensity. Ideally, it should remain static, but we know that there is always inherent noise in any system, called system noise, which needs to be analyzed to determine our limit of detection (Medina Escuela, 2011).

The most practical option adopted to deal with this noise was to use a digital filter with the fast Fourier transform to filter the higher frequency components of the curve, avoiding the loss of relevant information. This filter takes into account a threshold value

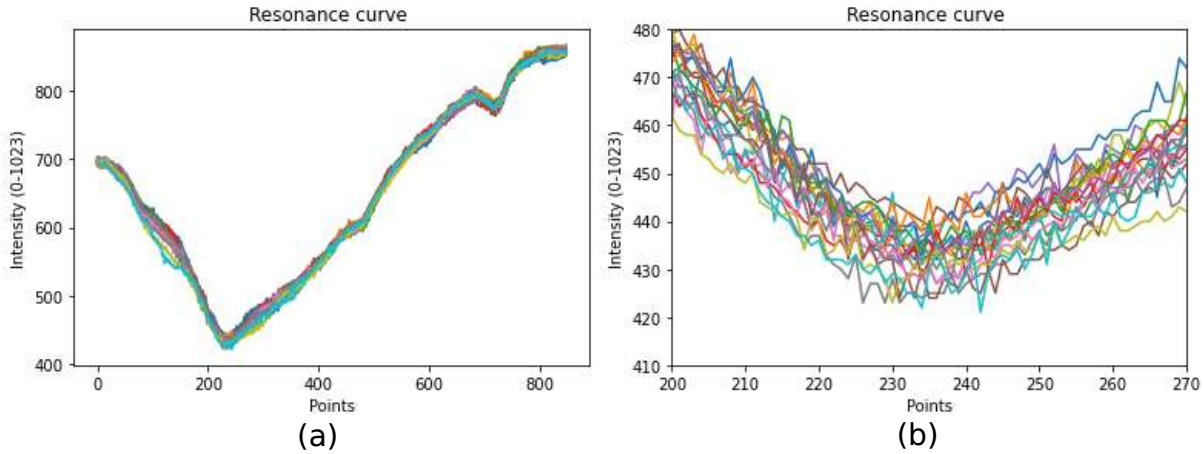

Figura 3.19 – Resonance curves for the case of water in contact with 50 nm gold layer. (a) Twenty repetitions. (b) Detail of the noise in the resonance region.

(N_{THRESH}), which is the coefficient that impacts the number of frequency components that will be maintained in the curve. For example, a value $N_{THRESH} = 5$, retains less high frequency jitter information compared to a value $N_{THRESH} = 10$. Fig. 3.20 graphically presents the impact of both values.

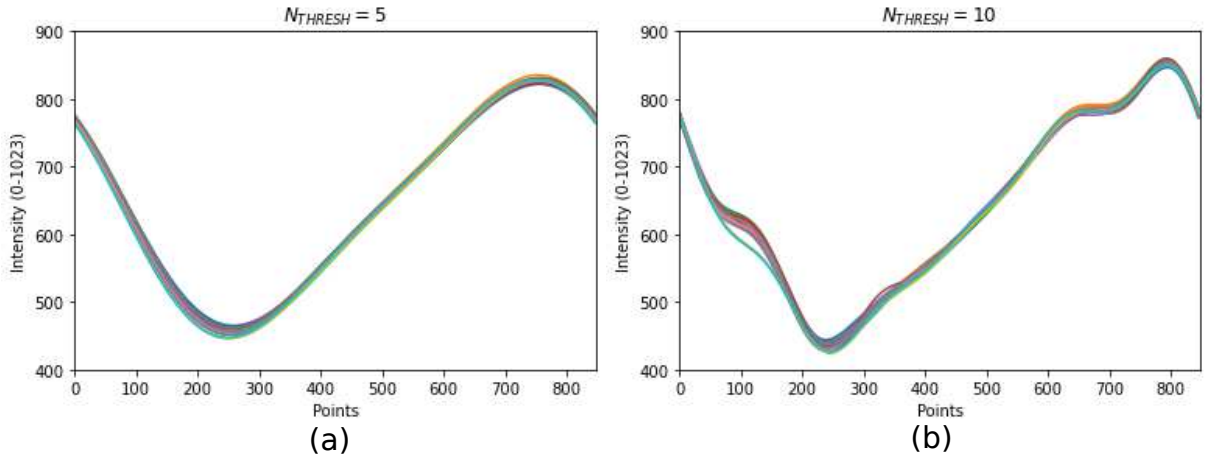

Figura 3.20 – Filtered resonance curves with a threshold coefficient of (a) $N_{THRESH} = 5$ (b) $N_{THRESH} = 10$.

The value we choose for threshold will impact the position of the resonance and therefore, the stability of our system, which will represent the noise of the system linked to the system detection. Fig. 3.21 (a) and (b) show the capture of the resonance position for the twenty captured curves, using the coefficient N_{TRESH} with values of 5 and 10.

The necessary value to be captured in Fig. 3.21 (a) and (b) is that of the standard deviation, which will be calculated in terms of variation of resonant points, and which can be expressed in terms of angles due to the mentioned equivalence than a difference of each point equivalent to 0.012°. Table 3.3 presents a compilation of the values of the mean, standard deviation and its angular equivalent for different values of

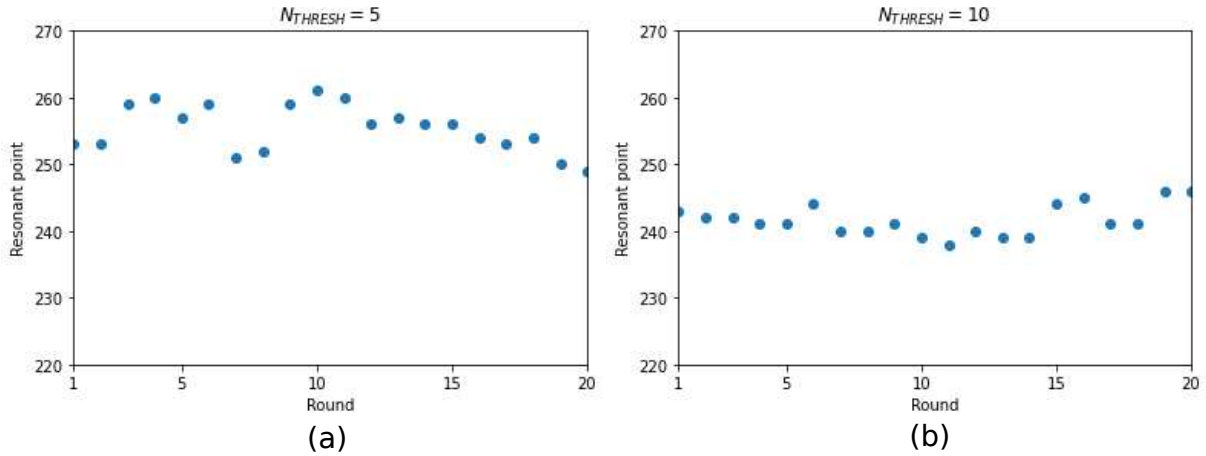

Figura 3.21 – Resonance positions for the 20 rounds, considering a digital filter with coefficient (a) $N_{THRESH} = 5$ (b) $N_{THRESH} = 10$.

N_{THRESH}.

N_{THRESH}	Mean point	Standard deviation (point)	Standard deviation (°)
3	292.4	2.33	0.027
5	255.4	3.47	0.041
7	259.6	1.39	0.016
10	241.6	2.31	0.027
12	241.3	3.16	0.037
15	245.6	1.74	0.020

Tabela 3.3 – Standard deviation values for different values of the filter used.

From Table 3.3 it can be inferred that for a wide variety of values of N_{THRESH} there is a standard deviation of less than 0.05°, reaching a minimum value of 0.016°.

Sensorgram

With the 'Tracking System Interface' it is possible to capture the resonance curve and monitor the resonance angular position for each curve, like the images shown in Figure 3.21. In this way, the sensorgram allows to identify the change of the index of the sample versus time. A sensorgram that has a high tracking frequency will allow the index change to be identified more quickly, which is important for the analysis of bonding and antibonding reaction rates, for biological and pharmacological applications (Richard B. M. Schasfoort, 2017; MUSTANSAR, 2020; Affinité Instruments, 2019).

To evaluate this tracking process, 3 solutions have been tested: pure water, a mixture of water and 25% ethanol and one with 50% ethanol. The refractive indices measured with the Metter Toledo refractometer are, respectively: 1.3333, 1.3462 and 1.3582, from an average of ten measurements, average truncated to the fourth significant decimal.

The fourty rounds captured are shown in Fig 3.22.

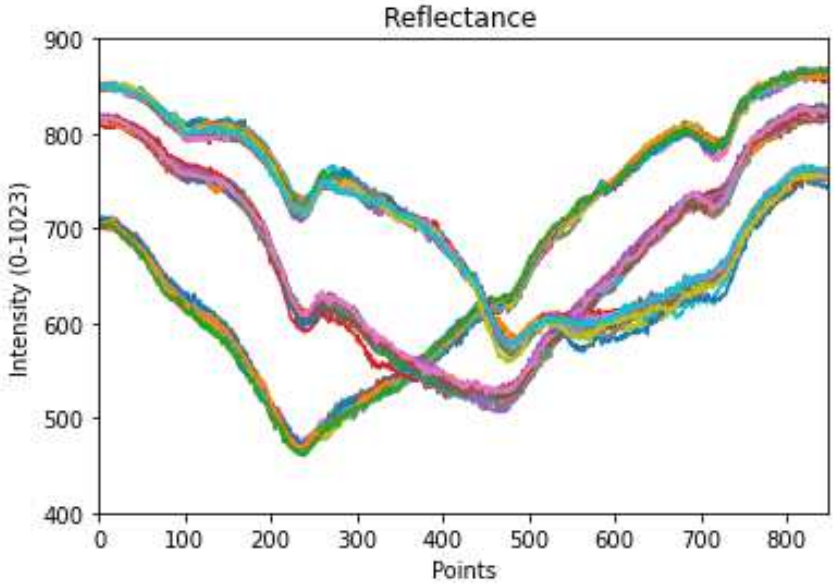

Figura 3.22 – Resonance curves captured for three different samples: water, 25% ethanol-fuel, and 50% ethanol-fuel.

Again, to reduce the noise, the digital filter is used, whose threshold coefficient filters the noise but also limits the amount of information contained in the curve. The impact of this coefficient on the sensorgram is shown in Fig. 3.23.

At this point, it is important to highlight that the sensor presented is of differential type, that is, it is based on the diagnosis of the change in resonance position, based on a referential sample, with a previously known index, from which the resonance change.

Working with the sensorgrams shown in Fig. 3.23, the value of the sensor's sensitivity can be obtained as the slope of the adjusted line of resonance angle variation versus the refractive index value. A pair of these curves are shown in Fig. 3.24 for the values $N_{THRESH} = 3$ and 9. As mentioned, the slope of the line represents the sensitivity in units of $°/RIU$. Another parameter of interest is 'coefficient of determination' (R^2) which tells us how well our linear regression fits our measurements (SCRIBBR, 2022). A collection of sensitivity, coefficient of determination, and standard deviation values for each of the three regions is shown in Table 3.4.

According to the results shown in Table 3.4, we can infer that the most convenient N_{THRESH} value to work in this setup is $N_{THRESH} = 9$. With this parameter there is a sensitivity of $156°/RIU$ (the highest value) with a coefficient of determination of 0.96. The standard deviation values per region indicate the detection limits that the sensor presents working in the region of these samples. The FWHM estimation is also performed for each region since it can be seen that the resonance curve changes in each of

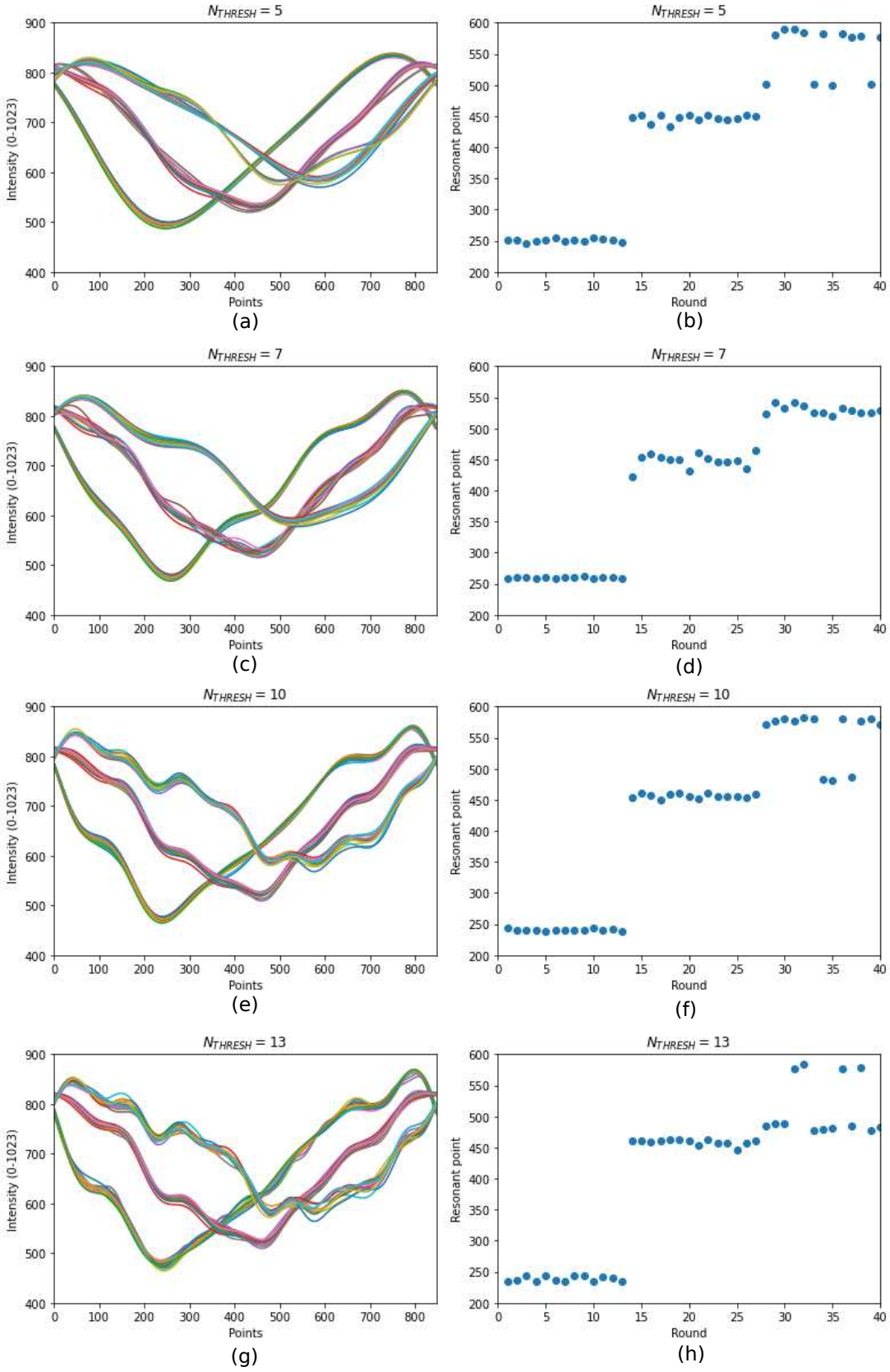

Figura 3.23 – (a), (c), (e) and (g) present the resonance curves for different N_{THRESH} values. (b), (d), (f) and (h) present the impact on sensorgrams.

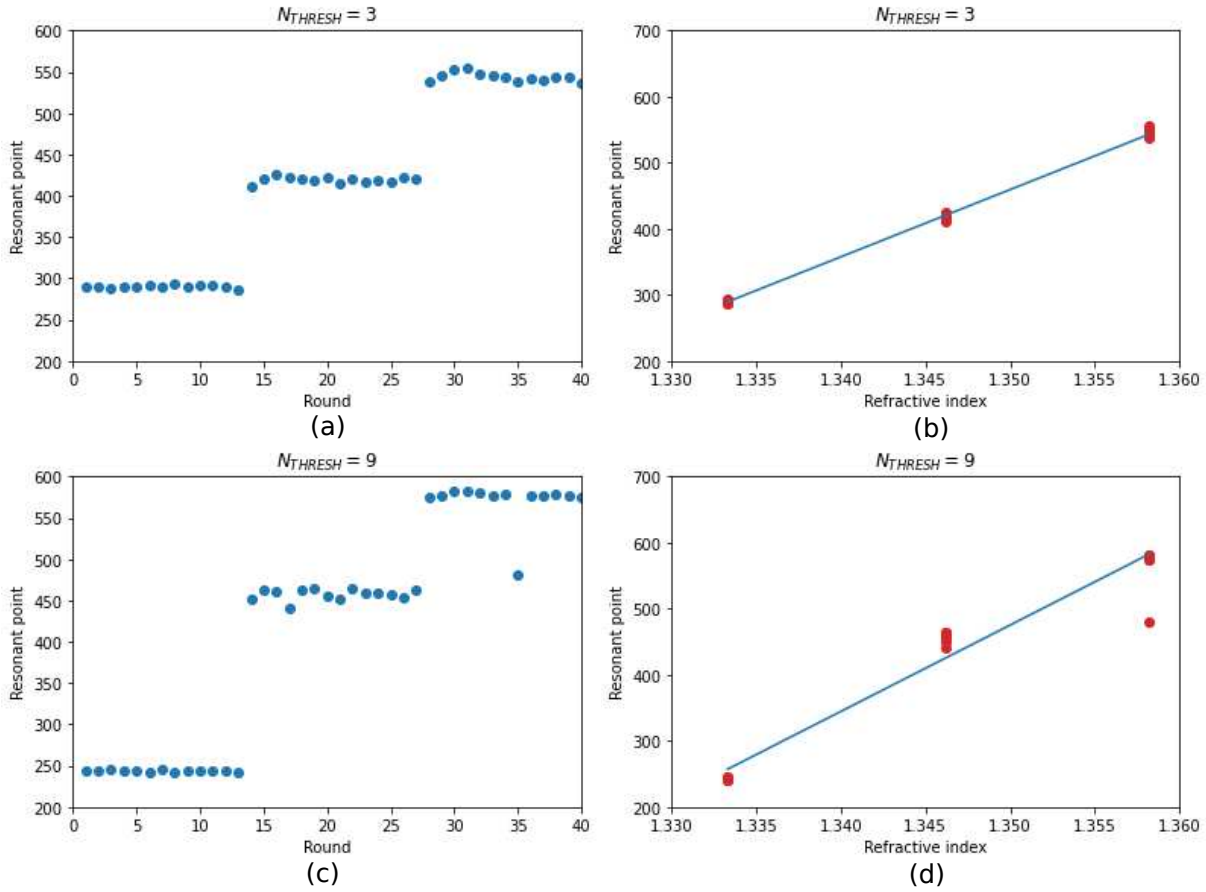

Figura 3.24 – (a) and (c) present the sensorgram for different $N_{THRESH} = 3$ and 9 values. (b) and (d) present the respective linear regressions adapted.

these cases. The compilation of these sensor parameters are shown in Table 3.5. At this point we remember that the FoM and LoD concepts used are defined by Eqs. 3.3 and 3.4 (BIJALWAN; SINGH; RASTOGI, 2020; AKIB et al., 2021).

$$FoM = S/FWHM \tag{3.3}$$

$$LoD = 3\sigma/S \tag{3.4}$$

The figure of merit of the sensor is in the range $33 - 39RIU^{-1}$ while the detection limit reaches $2.3E{-}4RIU$ for samples with indices close to 1.3333 (region 1). As the refractive index of the sample increases (region 2 and 3) the LoD increases, reducing the ability of the sensor to distinguish small variations of the index. This issue of the sensor's ability to work in specific ranges of indices is also discussed in Section 3.3 where it is discussed from the perspective of the impact of the gold and titanium layer used.

N_{THRESH}	S (°/RIU)	R^2	Standard deviation (°)		
			Region 1	Region 2	Region 3
3	122	0.99	0.019	0.042	0.059
4	134	0.97	0.026	0.047	0.301
5	145	0.94	0.032	0.066	0.452
6	136	0.95	0.012	0.077	0.277
7	129	0.95	0.014	0.130	0.080
8	146	0.95	0.011	0.080	0.332
9	156	0.96	0.012	0.073	0.311
10	149	0.93	0.014	0.041	0.479
11	146	0.9	0.033	0.022	0.559
12	138	0.88	0.028	0.037	0.583
13	134	0.85	0.048	0.050	0.537
14	123	0.83	0.028	0.049	0.415
15	122	0.83	0.019	0.060	0.407
16	122	0.83	0.021	0.060	0.399

Tabela 3.4 – Sensitivities, determination coefficientes and standard deviation per region for different values of N_{THRESH}.

	Region 1 n = 1.3333	Region 2 n = 1.3462	Region 3 n = 1.3582
FWHM (°)	4	4.7	4.4
FoM (RIU^{-1})	39	33	35
LoD (RIU)	2.3E-4	1.4E-3	5.9E-3

Tabela 3.5 – Sensor parameters for $N_{THRESH} = 9$, S = 156°/RIU.

3.1.6 Experimental results

In addition to the tests for the characterization of the sensor, two additional sets of measurements were captured with different concentrations of water and ethanol-fuel to analyze the behavior of the sensor for other data sets. Due to the experimental conditions, the combinations between amounts of water and ethanol-fuel were not always exactly the same. This led us to measure the refractive index of each sample prior to insertion into the microfluidic system.

Set of measures 1

Four samples of water and different concentrations of ethanol-fuel were prepared. The sensorgram obtained in this experiment together with the linear fit is shown in Fig. 3.25.

The sensorgram shown was obtained for the value of $N_{thresh} = 6$ and comprises a total of 70 rounds, that is, 70 resonance curves analyzed, taking a time of about 30

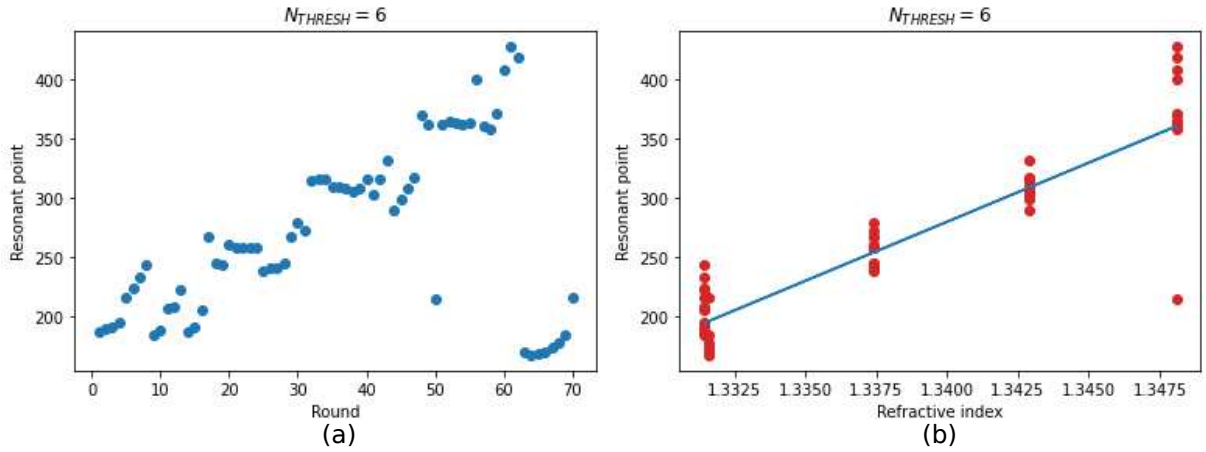

Figura 3.25 – Sensorgram and linear fit for $N_{THRESH} = 6$. Refractive index values: $1.3314, 1.3374, 1.3429, 1.3481, 1.3316$.

minutes.

For the use of the coefficient $N_{thresh} = 6$, the values of S and R^2 for different values of this coefficient were analyzed. The behavior of the values of S and R^2 are shown in Fig. 3.28. This value was chosen since it presents the best performance in the linear line fit, having a determination coefficient value of 0.86.

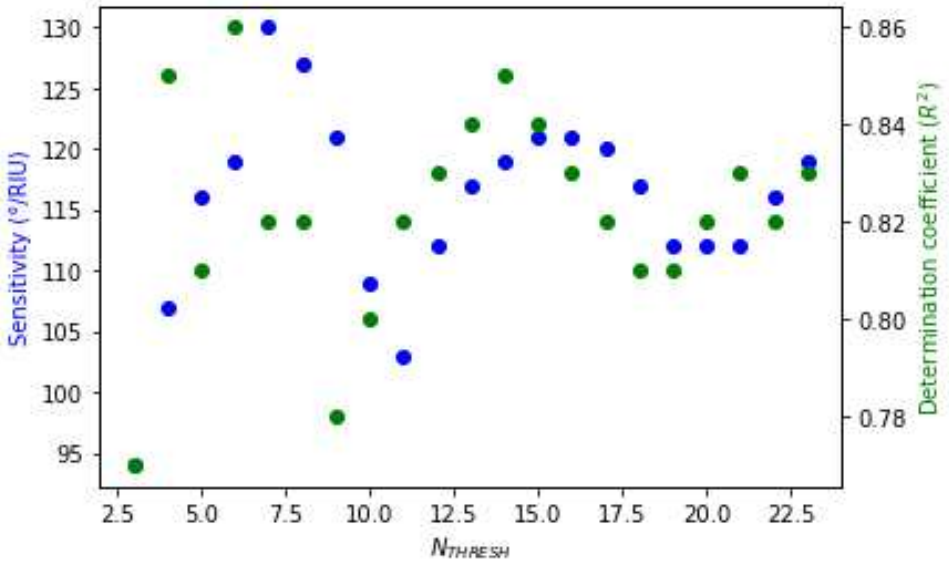

Figura 3.26 – Sensitivity and coefficient of determination for N_{thresh} values from 3 to 23. The maximum value of R^2 is obtained for $N_{thresh} = 6$.

The FWHM value obtained is close to 3.6°, so this value will be used to calculate the sensor parameters. Since we have a sensitivity of 119°/RIU, the Figure of Merit (FoM) is:

$$FoM = \frac{S}{FWHM} = \frac{119^o/RIU}{3.6^o} = 33RIU^{-1} \tag{3.5}$$

Regarding the value of the detection limit, it is calculated based on the standard deviation of the continuous capture in each of the samples. The results are shown in Table 3.6.

	Region 1 n = 1.3314	Region 2 n = 1.3374	Region 3 n = 1.3429	Region 4 n = 1.3481
Standard deviation (°)	0.2151	0.1480	0.5600	0.1835
LoD (*RIU*)	5.42E-3	3.73E-3	2.71E-03	1.41E-2

Tabela 3.6 – Sensor parameters for $N_{THRESH} = 6$, S = 119°/RIU.

Set of measures 2

Again, four sets of samples with different refractive indices were taken. The sensorgram obtained with $N_{thresh} = 5$ and the linear fit is shown in Fig. 3.27. The values of S and R^2 for different values of N_{thresh} are shown in Fig Y. The criteria for choosing the value of N_{thresh} to work with is the one that allows us to have the best coefficient of determination.

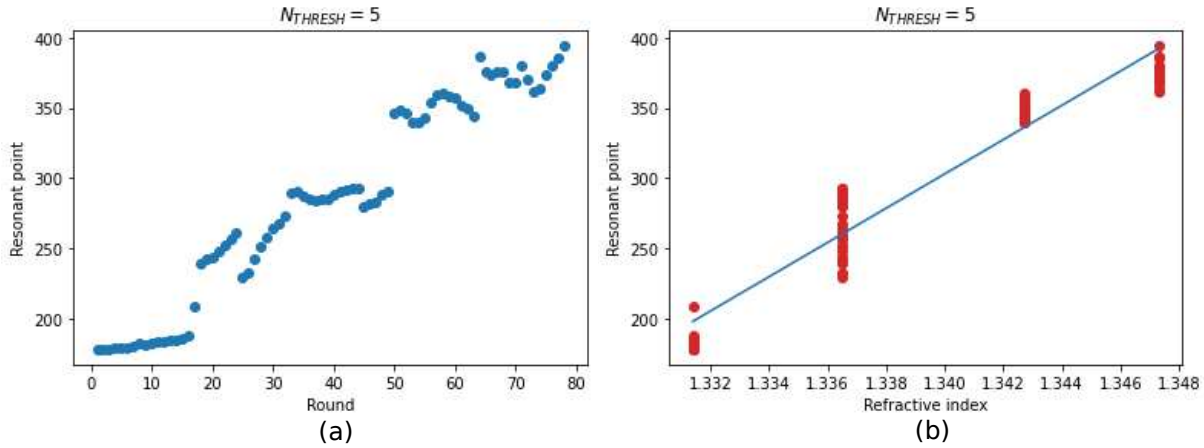

Figura 3.27 – Sensorgram and linear fit for $N_{THRESH} = 6$. Refractive index values: 1.3314, 1.3374, 1.3429, 1.3481, 1.3316.

Again, the FWHM value obtained is close to 3.6°, so this value will be used to calculate the sensor parameters. Since we have a sensitivity of 146°/RIU, the Figure of Merit (FoM) is:

$$FoM = \frac{S}{FWHM} = \frac{146^o/RIU}{3.6^o} = 40RIU^{-1} \tag{3.6}$$

Regarding the value of the detection limit, it is calculated based on the standard deviation of the continuous capture in each of the samples. The results are shown in Table 3.7.

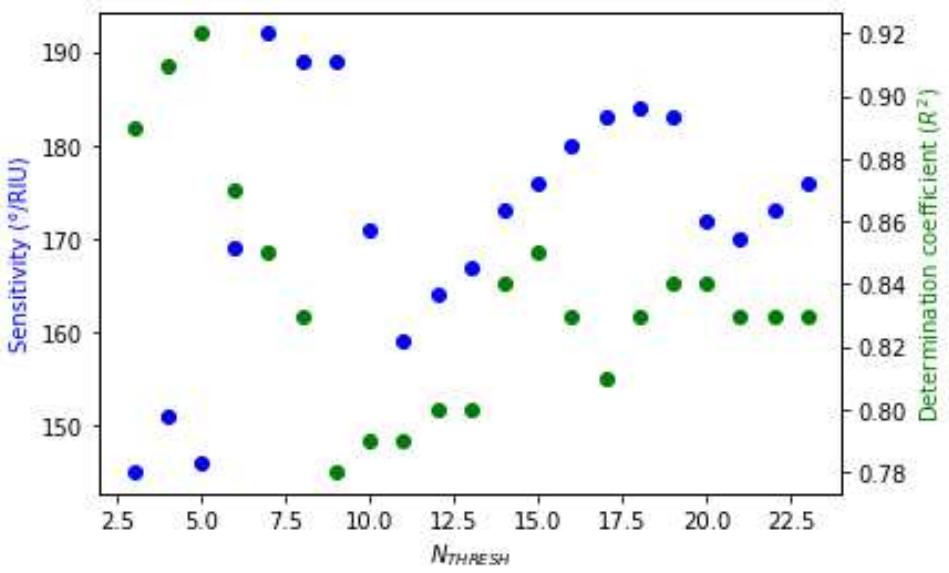

Figura 3.28 – Sensitivity and coefficient of determination for N_{thresh} values from 3 to 23. The maximum value of R^2 is obtained for $N_{thresh} = 5$.

	Region 1 n = 1.3314	Region 2 n = 1.3374	Region 3 n = 1.3429	Region 4 n = 1.3481
Standard deviation (°)	0.0822	0.2436	0.0808	0.1012
LoD (RIU)	1.68E-3	5.00E-3	1.66E-03	2.07E-3

Tabela 3.7 – Sensor parameters for $N_{THRESH} = 5$, S = 146°/RIU.

3.2 Sensing by intensity interrogation

This detection system is based on the determination of the refractive index change from the change in the intensity of light reflected from the gold/dielectric interface. The intensity interrogation system allows to maintain the angle of incidence constant, and its principles are described in (HOMOLA, 2006a).

3.2.1 Setup configuration

The system used is the same as the one shown in Fig. 3.12 and with the scheme in Fig. 3.14, so the rotation configurations and materials are the same as those described in section 3.1.1. The variation is found in the detection system, also called the interrogation scheme: Starting from the location of the resonance position, the angle of incidence is kept constant, continuously capturing the reflected intensity by varying the samples in contact with the gold. Fig. 3.29 shows the photodetector and CCD camera used for capturing the reflected beam.

Intensity Tracking System Interface

This interface allows to continuously capture the different intensity values that

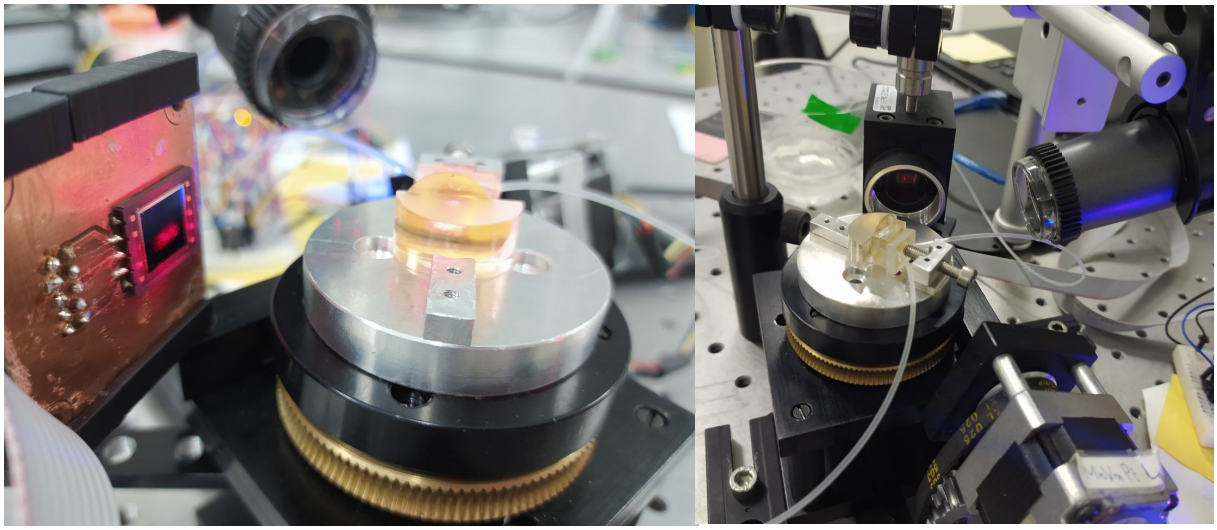

(a) (b)

Figura 3.29 – (a) Photodetector S5870 capturing the reflected intensity. (b) CCD Camera recording the incident beam.

are received in the photodetector. It is shown in Fig. 3.30.

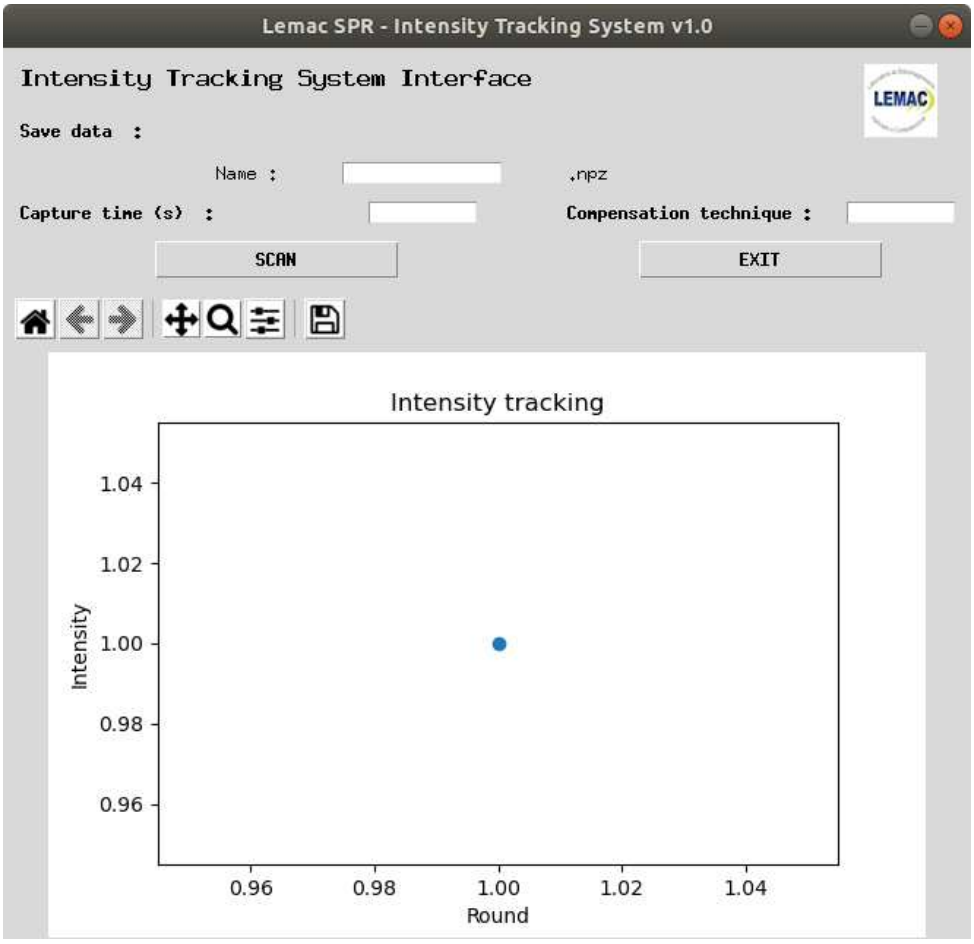

Figura 3.30 – GUI for the intensity tracking system.

The interface features are described below:

- **Name:** Set the name of the file with extension .npz to save the intensity values.
- **Capture time:** It is the period of time for which the intensity values received will be capture for the photodetector.
- **Scan:** Starts the data capture period in the photodetector. At the end of the programmed period, the file will be created with all the intensity values captured.
- **Exit** Close the interface.

  In the 'Resonance tracking' graph are presented all the intensity values captured at each instant of time during the set period. It is important to highlight that for the initial angular location the 'Resonance detection interface' GUI described in section 3.1.4 is used.

  This interface is only used with the S5870 photodetector, whose readout is linked to the Arduino, shown in Fig. 3.29(a). In the case of intensity reading with the CCD camera, the intensity files are saved directly on the computer with the proprietary software ThorCam (THORLABS, 2022e).

3.2.2 Detection using Photodetector

In this case, the S5870 photodetector is used to capture the intensity values with the previously described graphical interface. The sensorgram was captured with different samples of combinations of water with ethanol-fuel, from which we can obtain the main parameters of the sensor.

Six samples of different combinations were used, obtaining the sensorgram shown in Fig. 3.31. From combinations of water and ethanol were obtained samples with indexes from $1.3313, 1.3360, 1.3425, 1.3477, 1.3525, 1.3561$. All these values were obtained by the refractometer before entering the microfluidic circuit.

The intensity values are assumed to be arbitrary units (au) and we perform the linear fit from the mean intensity values obtained and shown in Fig. 3.32. The slope of the line represent the sensitivity of the sensor, in this case this value is $S = 11154 AU/RIU$. This linear regression presents a determination coefficiente $R^2 = 0.97$.

From these values, the sensor parameters compiled in Table 3.8 are obtained.

3.2.3 Detection using CCD Camera

Intensity detection is also evaluated using a CCD camera model DCU224M (THORLABS, 2021). In this case, the beams reflected by the metal/sample interface are captured directly with the camera. 100 images are captured for each sample, to obtain a representative value of the standard deviation obtained with this setup.

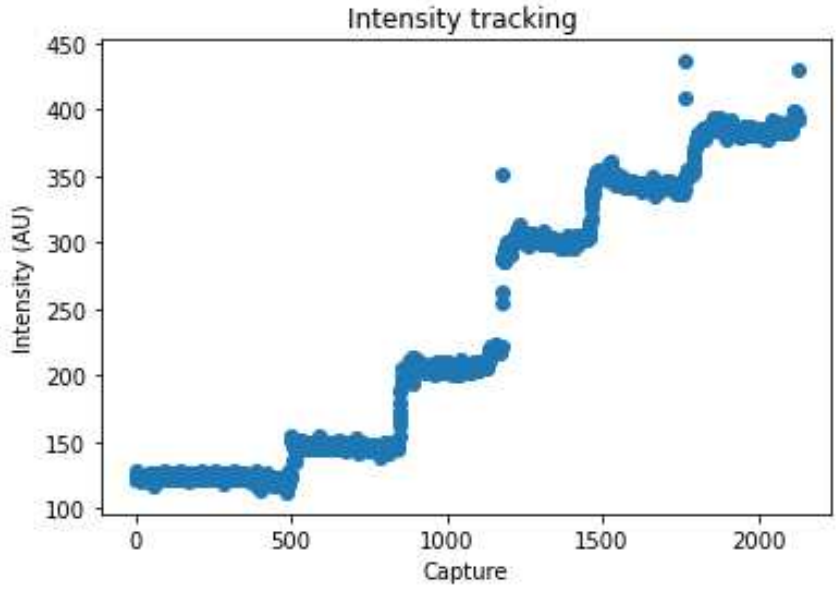

Figura 3.31 – Intensity values (in Arbitrary Units) for six different samples with $RI = 1.3313, 1.3360, 1.3425, 1.3477, 1.3525, 1.3561$.

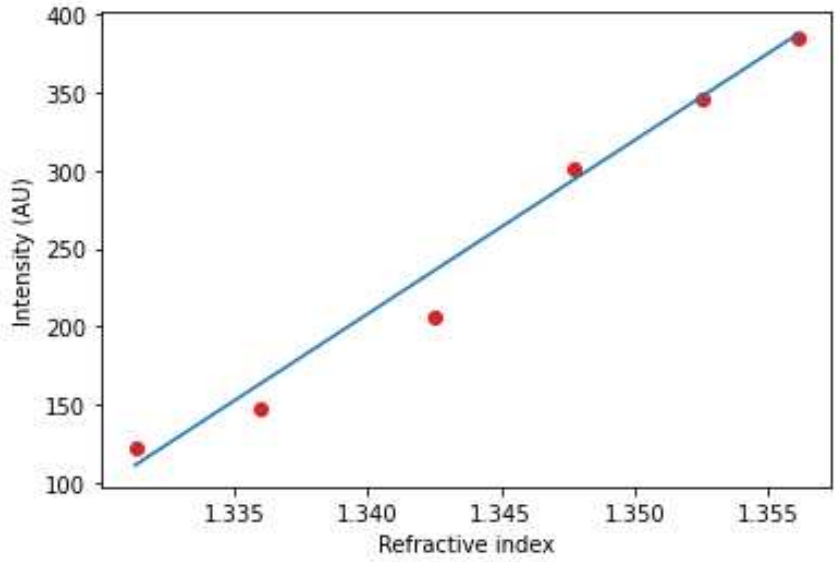

Figura 3.32 – Linear regression for intensity values in function of the refractive index of the samples.

	Region 1	Region 2	Region 3	Region 4	Region 5	Region 6
Refractive index (RIU)	1.3313	1.3360	1.3425	1.3477	1.3525	1.3561
Mean Intensity (ua)	122.48	146.57	206.64	301.05	345.69	385.05
Standard deviation (ua)	1.98	2.04	7.52	5.55	8.72	4.57
LoD (RIU)	5.3E-4	5.4E-4	2.0E-03	1.4E-3	2.3E-3	1.2E-3

Tabela 3.8 – Sensor parameters for intensity interrogation system.

Figure 3.33 shows a collection of beams captured for different combinations of water and ethanol-fuel with refractive indices: 1.3311, 1.3371, 1.3426, 1.3475, 1.3520, 1.3529. Figure 3.34 presents the relative intensity representations for each sample along with the line fit obtained for such a case.

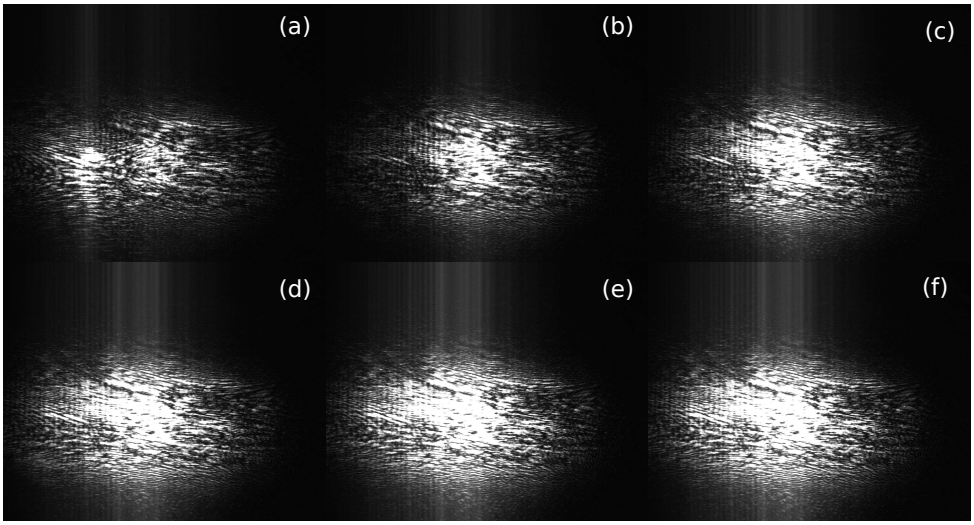

Figura 3.33 – Reflected beams captured by CCD camera for different samples.

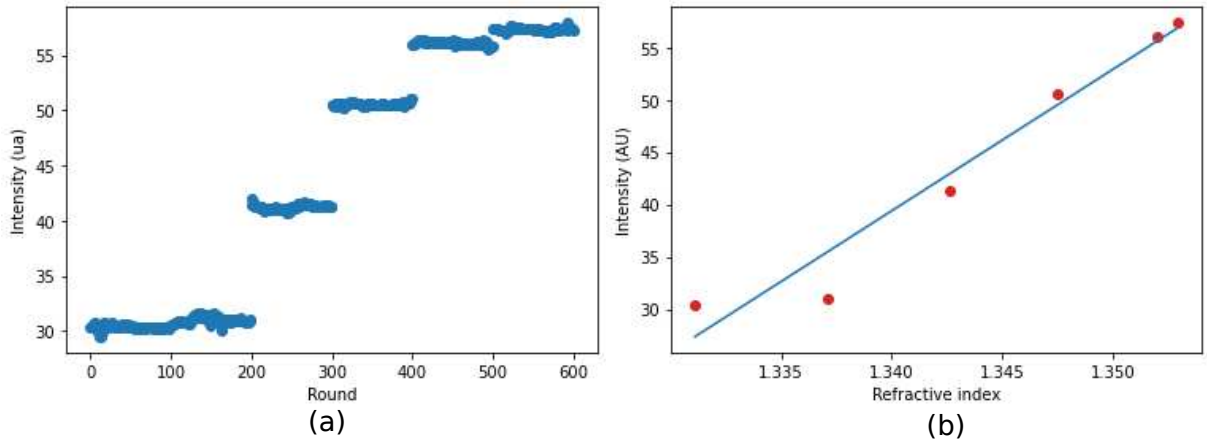

Figura 3.34 – Linear regression for intensity values in function of the refractive index of the samples.

The intensity values from the captured beam images are obtained from the sum of the values assigned to each pixel, which are values from 0 to 255 in the .tif extension, a format provided by the camera software. Because the image is $1280x1024$ pixels, the total sum is divided by 1310720 (total number of pixels), which allows us to have a normalized intensity value, so in this case we also use arbitrary units for intensity. Finally, the objective is the evaluation of the slope of the line of adjustment or sensitivity in the dimension that allows it to be reproduced in a simple way. Thus, the sensitivity obtained by linear regression is 1349 au/RIU with a determination coefficient $R^2 = 0.95$. The other sensor parameters are shown in Table 3.9.

	Region 1	Region 2	Region 3	Region 4	Region 5	Region 6
Refractive index (RIU)	1.3311	1.3371	1.3426	1.3475	1.3520	1.3529
Mean Intensity (ua)	30.35	31.0	41.24	50.55	56.07	57.34
Standard deviation (ua)	0.21	0.27	0.21	0.12	0.16	0.13
LoD (RIU)	4.6E-4	6.0E-4	4.6E-04	2.6E-4	3.5E-4	2.8E-4

Tabela 3.9 – Sensor parameters for intensity interrogation system using CCD camera.

3.3 Adhesion layer impact in sensing performance

3.3.1 Analytical approach

In this subsection, the Fresnel reflection coefficient is used to simulate a multilayer structure and to analyze the characteristics of a SPR sensor based on the Kretschman configuration. For simplicity, the Matlab code available in (ORFANIDIS, 2016) was adapted and used as a starting point.

We start the plasmon resonance analysis from a gold deposition directly on prism (without adhesion layer), working at 632.8 nm wavelength. The materials are: prism BK7 ($n_a = 1.5151$) (SCHOTT, 2014) and gold ($n = 0.18508 - j3.4233$) (P. B. Johnson and R. W. Christy, 1972), and as sensing material is considered air ($n_b = 1$). For this case, a maximum resonance (lower resonance reflection) is obtained around 48 nm of gold thickness. Figure 3.35 plots this resonance curve for a wide angular range. In addition, two resonance quality parameters are indicated: Extinction Ratio (ER) and Full Width at Half Minimum (FWHM). Both parameters are used to characterize various plasmonic or dielectric resonant devices (HAQUE; ROUF, 2019; MANOLIS et al., 2019).

The ER is defined as the depth of the dip in the resonance condition, while the FWHM quantifies the curve width at half intensity dip.

A high-quality plasmon resonance implies a maximum extinction ratio and a minimum FWHM. However, to analyze the resonance curve from the perspective of its application as a sensor, new factors come into play as sensitivity (S), detection accuracy (DA) and Figure of Merit (FOM) (BIJALWAN; SINGH; RASTOGI, 2020; AKIB et al., 2021). These new parameters directly involve the displacement of the resonance against a change in the index of the sensing medium (n_b). The literature in this regard defines the following:

- Sensitivity - S: Rate of change of the resonance angle with respect to the index of the medium to be sensed.
- Detection Accuracy - DA: Inverse of FWHM.

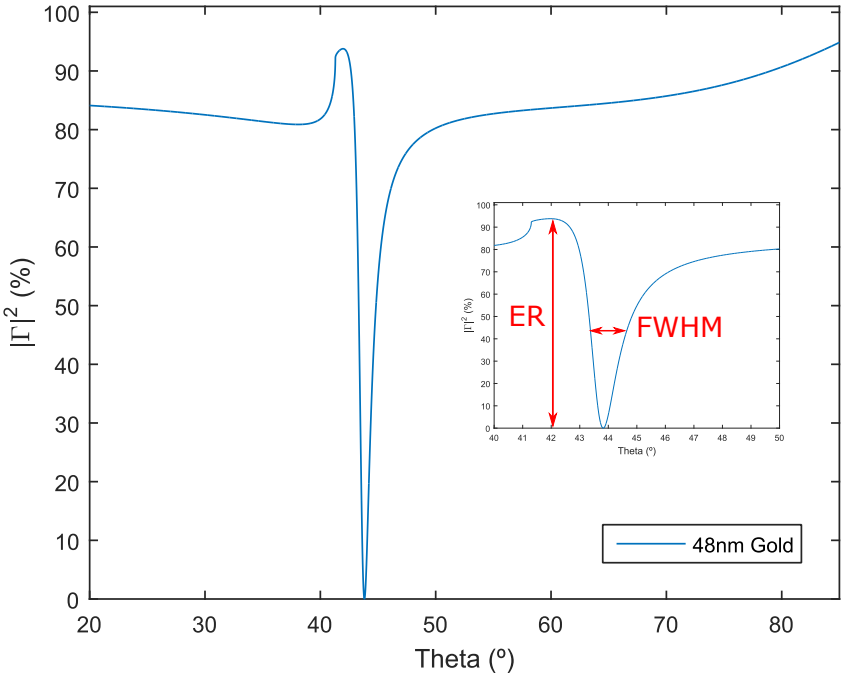

Figura 3.35 – Reflectance values (in %) for wide incidente angular range. Sensing medium: air.

- Figure of Merit - FOM: relationship between the sensitivity with the FWHM.

In this way, new sensor designs of any kind are constantly searching for devices with the higher sensitivity and FoM values (higher DA and lower FWHM).

3.3.2 Single gold layer case

We start the analysis of the sensing performance from a single layer of active plasmonic metal: the ideal case of a direct deposition of gold on prism. Foreseeing the analysis of sensing using ethanol-fuel samples, we consider a variation from $n_b = 1.3638$.

As is known (SRIVASTAVA; VERMA; GUPTA, 2011), for low concentrations of water in ethanol, the refractive index tends to increase, so we consider an analysis range between 1.3638 and 1.3650 (approximately 10% water concentration or 90% ethanol-fuel purity). Fig 3.36 shows the resonance variation for five values of n_b in the range mentioned above, considering a gold thickness of 48 nm and a wavelength of 632 nm.

With the samples indicated in Fig. 3.36 a sensitivity $S = (195 \pm 10)°/RIU$ is obtained. However, for different gold thickness values, sensitivity changes. Figure 3.37 shows these changes in the $30 - 80$ nm gold thickness range. As shown in the insets of Fig. 3.37, both 30 and 80 nm thickness values represent extreme cases for the practical use of resonance in sensing activity. For the case of a 30 nm thickness of gold, the ER remains relatively high (approximately 50%) however the reflection at resonance is quite

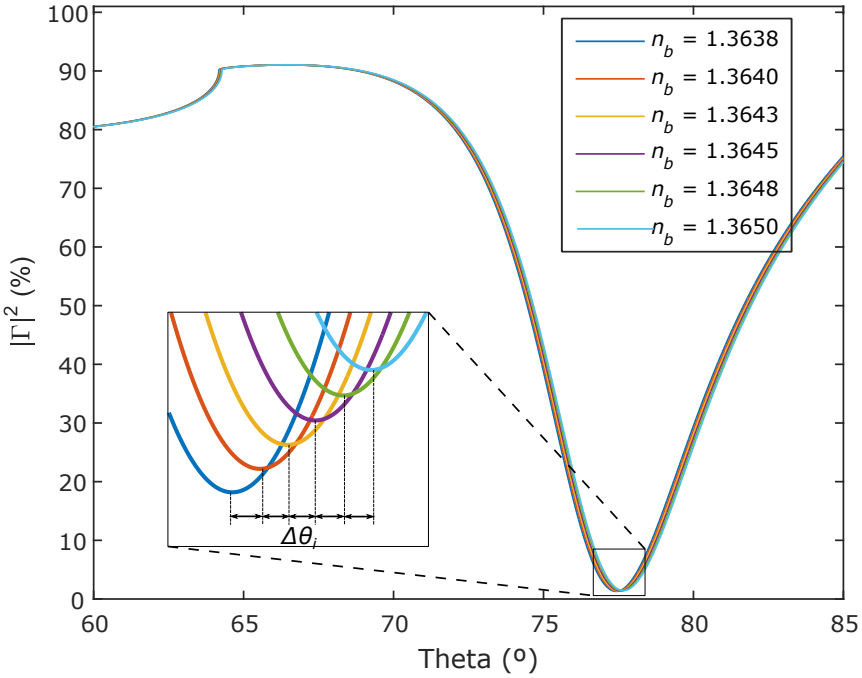

Figura 3.36 – Sensing by angular interrogation method. Sensing mediums: different concentrations of water in ethanol-fuel.

close to the reflection level for other angles of incidence, as shown by the symbol Δ. This represents a weakening in sensing ability, which explains a lower value for S. The other extreme case occurs for values greater than 80 nm, as shown in the second inset of Fig. 3.37. In this case, the ER drops to levels of 10%. This low extinction ratio at resonance can cause problems for experimental measurement setups, so in this work an ER of 10% is taken as the minimum limit to be considered practical.

3.3.3 Cases for titanium and gold layer

Now we consider the case of the intermediate layer of titanium, considering thicknesses between 0 and 20 nm, because this value already implies a loss of resonance, following the criteria mentioned in the previous section. In the same way a maximum gold thickness of 80 nm is considered. Figure 3.38 shows the sensitivity levels for the range of values indicated.

From Fig. 3.38 we can identify six regions. The region in darker color is the blue one marked as 'no resonance region'. This is due to the fact that in this region the thickness of titanium present produces a loss of resonance, according to the criteria shown in Fig. 3.37. The other five regions are differentiated by their average sensitivity values, varying between around $140°/RIU$ up to $220°/RIU$.

The next parameter analyzed is the FOM, which is an expression of the potential quality of the sensor, as indicated in the previus subsection, it is calculated from the

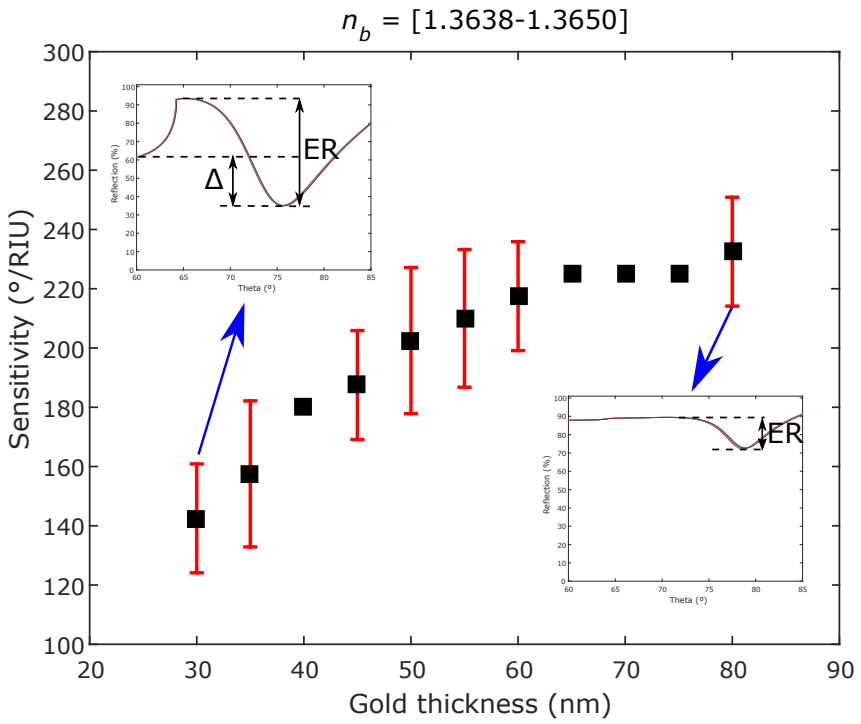

Figura 3.37 – Sensitivity values for different gold layer thicknesses.

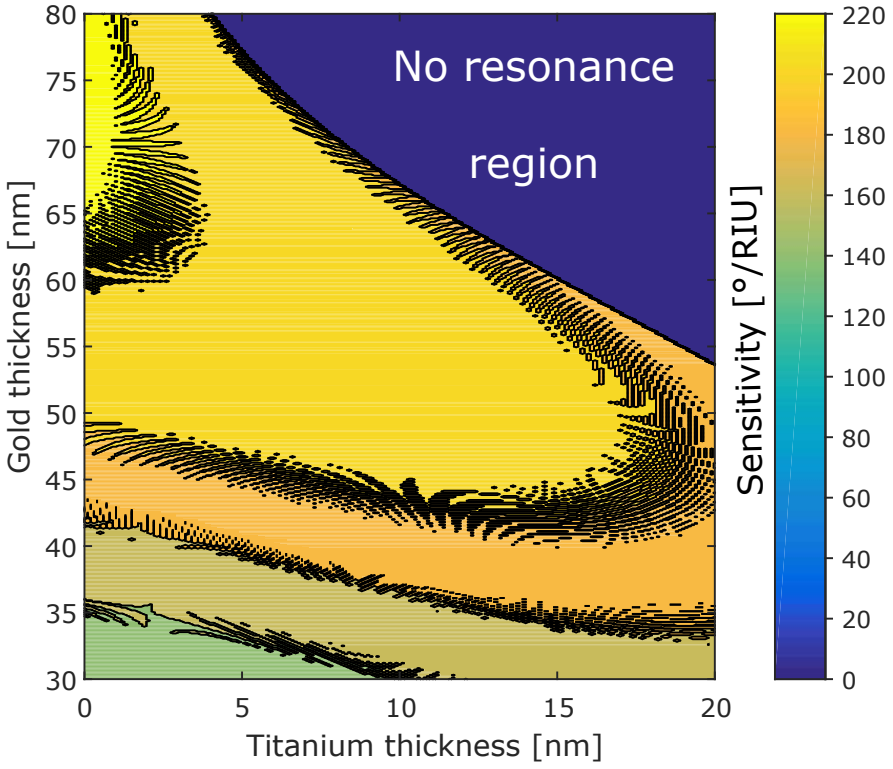

Figura 3.38 – Sensitivity values for values of Titanium and Gold thicknesses.

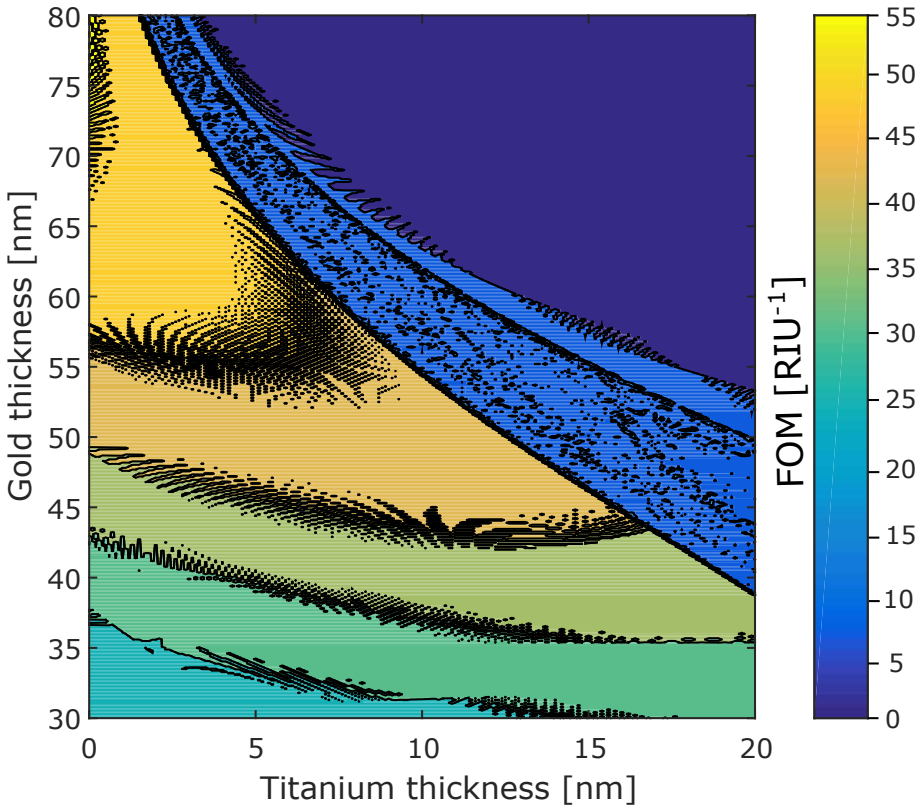

Figura 3.39 – FOM values for values of Titanium and Gold thicknesses.

relationship between S and FWHM. Figure 3.39 shows the results obtained for the range of thickness values analyzed. Again the upper right region, with the dark blue color, presents a null value due to the loss of resonance. However, unlike Fig. 3.38, this region, with a softer blue color, 'penetrates' the regions where high sensitivity values were reported. This is because the resonance in these regions, although they overcome the barrier of the criteria indicated in Fig. 3.37 to be considered 'valid', the width of the resonance is high, thus the FOM values are the lowest reported (about 10 RIU^{-1}). Six regions with FOM ranging from values of 25 RIU^{-1} to 55 RIU^{-1} are then identified.

3.4 Experimental tests

To validate the theoretical results presented in last subsection, experimental data was acquired with an SPR sensor setup based on the Kretschmann configuration and with angular interrogation. The setup uses 632 nm He-Ne laser with a TM polarization as excitation, a photodetector for reflectivity measurements, a circular BK7 prism, a $\theta/2\theta$ rotation system based on a stepper motor for incidence angle variation and a PDMS microfluidic system for liquid measurements. A schematic view and a picture of the complete setup is shown in Fig. 3.40, together with the Arduino control system and the Python based human machine interface.

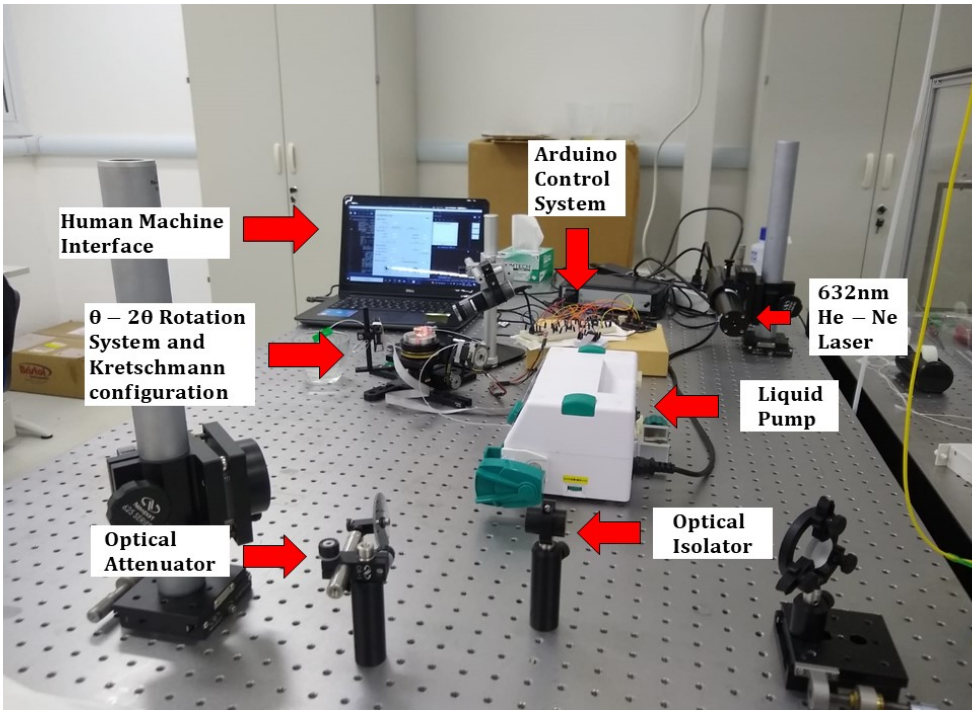

Figura 3.40 – Photo of SPR sensor setup based on Kretschmann configuration used for experimental validation.

3.4.1 Representative samples measurements

After careful calibration and alignment of the experimental setup, reflectivity measurements were taken for different SPR chips Ti/Au thicknesses. In this case, a constant layer of 2 nm of titanium was considered while the gold layer varied between 35, 50 and 75 nm. The liquid considered for testing was ethanol-water mixtures of 90%, 95% and 100% ethanol. To better estimate the point of minimum reflectivity, 10 measurements were taken for each liquid in each Ti/Au thickness case and the mean curve, obtained as the point by point mean of the 10 acquired curves, was considered. Not only that, but a moving average filter with a window of 30 samples was used to smooth the noise acting over the mean. The stepper motor moved a total of 10° with a constant step of 0.015° in each measurement and the refractive index of each sample was measured with a digital refractometer, where we found that 100% ethanol has an RI of 1.3638, 95% has an RI of 1.3648 and 90% has an RI of 1.3651. The results are shown in Fig. 3.41. The sensitivity obtained from the angular coefficients of each calibration curve is resumed in Tab. 3.10, together with its respective theoretical value and the relative error between numerical simulation and experimental results.

Clearly, the sensitivity presented by our setup is in great agreement with the sensitivity obtained through numerical simulation. Indeed, the relative error between experimental data and simulated data was, at maximum, 2.27%, validating that thicker gold layers gives greater sensitivity in SPR sensors for a same titanium layer. However,

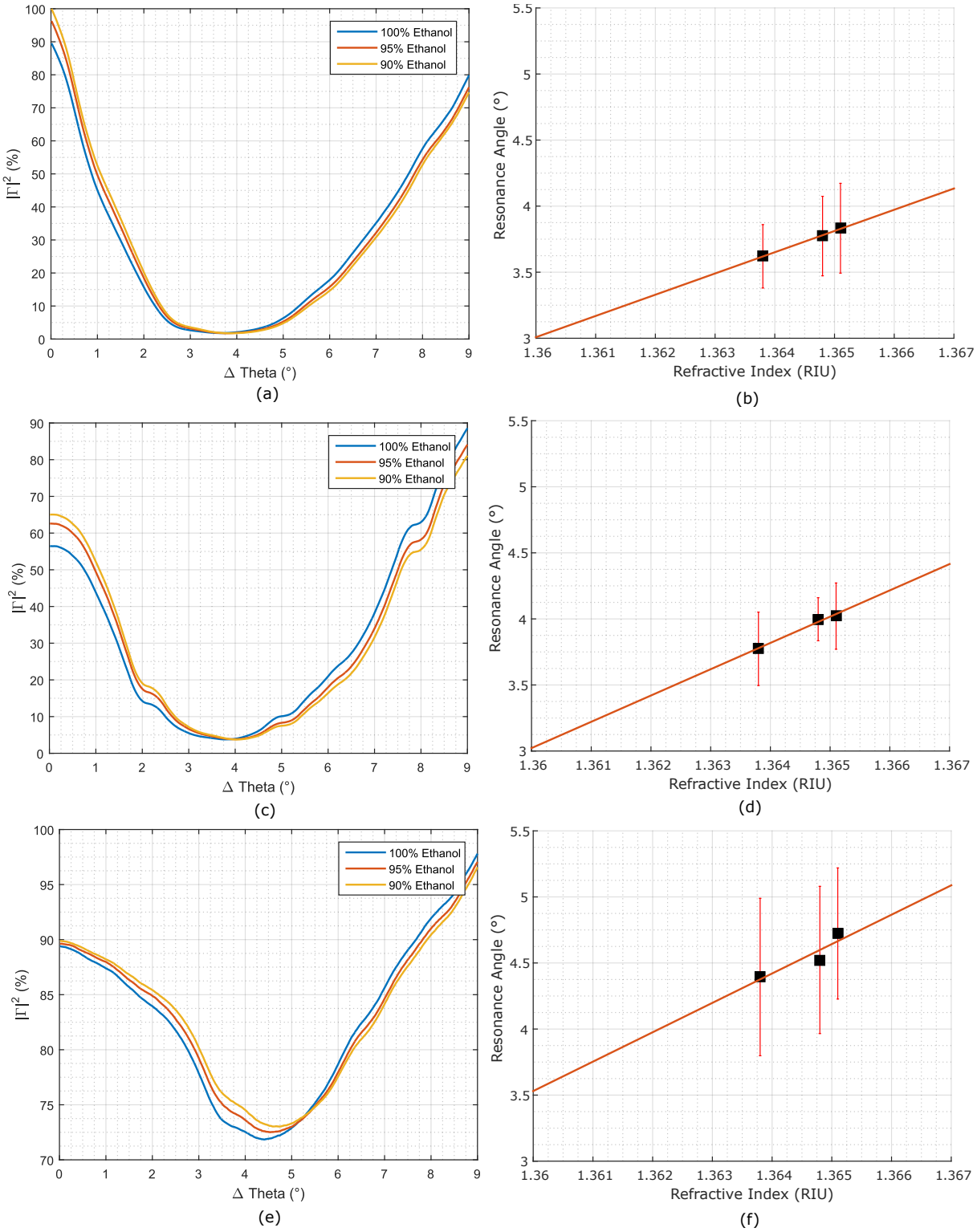

Figura 3.41 – SPR curves and calibration curves obtained for chips with a titanium layer of 2 nm and a gold layer of (a)-(b) 35 nm, (c)-(d) 50 nm and (e)-(f) 75 nm. The SPR curves shows, in the horizontal axis, the incidence angle in relation to the initial angular position, which we called $\Delta\theta$.

Tabela 3.10 – Comparison between sensitivity obtained through numerical simulation and experimental results.

Gold Layer Thickness (nm)	Theoretical Sensitivity ($°/RIU$)	Experimental Sensitivity ($°/RIU$)	Relative Error (%)
35	164.33	160.76	2.17
50	203.00	198.94	2.00
75	217.50	222.43	2.27

from the resonance curves shown in Fig. 3.41, the ER seems to reach lower and lower values with increasing gold layer thickness. As a matter of fact, the ER for a 35 nm gold layer is, approximately, 95%, while for the 75 nm gold layer, the ER was, approximately, only 18%. This results shows that there is a big trade-off between sensitivity and ER. Even though bigger sensitivities are reachable with thicker gold layers, weaker resonances are found for this same situation.

Table 3.11 shows the error obtained for our FOM measurements. A good agreement can be seen between the simulated values and the measured ones. The trend remains as in Tab. 3.10, the higher the thickness of gold, the higher the sensitivity and the FOM.

Tabela 3.11 – Comparison between FOM obtained through numerical simulation and experimental results.

Gold Layer Thickness (nm)	Theoretical FOM (RIU^{-1})	Experimental FOM (RIU^{-1})	Relative Error (%)
35	27.3	26.8	1.8
50	37.6	37.5	0.2
75	54.3	58.5	7.7

3.5 Comparison with other works

Table 3.12 presents a brief compilation of Kretchsmann schemes with adaptations that allow analyzing their performance for certain particular cases.

From the Fresnel reflection equations, the impact of the materials on the quality of the resonance curve and the sensitivity of the setup can be theoretically analyzed. In (GUPTA; KONDOH, 2007) the impact on sensitivity and figure of merit for three different prism types is exposed, both analytically and experimentally for dilute ethanol combinations. Using a unique photodiode scheme, in (Medina Escuela, 2011) an intensity detection configuration with a detection limit of up to 2.69E-5 RIU is presented, this solution is placed an order of magnitude below our result, which indicates that our setup

still requires improvements to reach this resolution. The larger FoM scheme is presented in (MÉJARD et al., 2013) which uses Long-range Surface Plasmons (LRSP) achieving quite narrow resonance curves. In (WANG et al., 2018a) the best resolution in sensitivity (LoD of 3.54E-6) in binding interactions of BSA with anti-BSA is achieved. A Digital Micro mirror device (DMD) is used with an array of mirrors and lenses that make setup complicated for portability purposes. In (HERNÁNDEZ, 2018) a Kretschmann setup is presented where the laser beam is focused on two materials: incidence on the PDMS and on the fluid, making a comparison with air and water. This setup achieves a Sensitivity of $66°/RIU$ and a FoM of $26RIU^{-1}$. An important increase in the sensitivity of the setup is using 2D-type materials, in (SINGH; PASWAN; RAGHUWANSHI, 2021) it is using graphene and black phosphorus to increase the sensitivity up to $218°/RIU$, tested using concentrations of water and ethanol. Another example of the use of 2D material is in (ZAIN et al., 2022) where relative humidity is measured reaching a sensitivity of up to 0.07°/%RH using graphene oxide.

In the angular scanning setup presented in this work, there is a sensitivity of up to 156°/RIU with a LoD of 2.3E-4. Despite the fact that the sensitivity becomes as theoretically expected, the detection limit level is still low than expected, indicating that there is still room for improvements in system noise reduction. This can be done by improving the limitations of the width of the laser beam and the background noise that affects the photodetector. In the case of intensity detection, LoD can also be improved by finding ways to reduce ambient noise by introducing a case, for example.

Author	Year	Description	Medium sensing (RIU)	S	FOM	LoD
G. Gupta, et.al. (GUPTA; KONDOH, 2007)	2006	Tests of three different prisms in Kretschmann configuration setup.	Ethanol solutions: 1.33-1.35	200°/RIU ($n_p = 1.456$), 135°/RIU ($n_p = 1.513$), 95°/RIU ($n_p = 1.597$)	$66 RIU^{-1}$ $54 RIU^{-1}$ $47.1 RIU^{-1}$	-
A. Medina, et.al. (Medina Escuela, 2011)	2011	Kretschmann setup with single photodiode. Based in intensity detection with fixed angle: 71.4°.	1.3327-1.3351	3360a.u.	-	2.69E-05
R. Mejard, et.al. (MÉJARD et al., 2013)	2013	LRSp based Kretschmann configuration setup. Use of Teflon and CYTOP over the glass in contact with the 20nm-gold layer.	1.331415-1.33257	77°/RIU	$466 RIU^{-1}$	-
D. Wang, et.al. (WANG et al., 2018a)	2018	Triangular BK7 prism and Digital Micro mirror device (DMD) based angular sweep. Use of spherical and cylindrical lens in the setup.	BSA and anti-BSA binding interaction tests	-	-	3.54E-06
D. Monzon, et.al. (HERNÁNDEZ, 2018)	2018	Krestschmann configuration adapted for dual-parameter sensing. Used of PDMS microfluidic sctruture and temperature monitoring.	1-1.33	66°/RIU	$26 RIU^{-1}$	-
Y. Singh, et.al. (SINGH; PASWAN; RAGHUWANSHI, 2021)	2021	2D material-based: graphene and black phosphorus in two gold layers (40 and 8nm thickness) of Kretschmann configuration.	1.33-1.36	218°/RIU	$26.13 RIU^{-1}$	-
H. Zain, et.al. (ZAIN et al., 2022)	2022	Kretschmann setup with 50nm-gold layer. Graphene oxide layer to increase the sensivitiy.	Relativity Humidity changes (% RU)	0.17°/%RH (using Graphene oxide) and 0.07°/%RU (without Graphene oxide)	-	-
This work	2023	Kretschmann setup with 50nm-gold layer. $\theta/2\theta$ rotation system Arduino+Pyhton control.	1.3313-1.3561	156°/RIU	$39 RIU^{-1}$	2.3E-4
This work	2023	Kretschmann setup with 50nm-gold layer. Intensity detection using photodetector.	1.3313-1.3561	11154 au/RIU	-	5.3E-4
This work	2023	Kretschmann setup with 50nm-gold layer. Intensity detection using CCD camera.	1.3311-1.3529	1349au/RIU	-	2.6E-4

Tabela 3.12 – Comparison table with performances of other prism-based Kretschmann setups.

4 INTEGRATED PLASMONIC SENSOR

4.1 Hybrid Plasmonic Waveguide

In this section we analyze the structure called a hybrid plasmonic waveguide (HPWG). This type of configuration has already been studied and presented as an easy-to-manufacture, high-confinement, and low-loss alternative for both communications and sensing applications (DAI; HE, 2009; OULTON et al., 2008).

Many recent developments using HPWG for sensing can be found in the literature grouped in two major trends: HPWG used for interferometric configurations (SUN; THYLÉN; WOSINSKI, 2017; MOHRI; ASAKAWA; SUZUKI, 2020; MANOLIS et al., 2019; DEBACKERE et al., 2006; KWON, 2010) and for ring resonator-based structures (BUTT; KHONINA; KAZANSKIY, 2018; ZHOU et al., 2011; BUTT; KHONINA; KAZANSKIY, 2019; Chou Chau et al., 2021; BUTT; KHONINA; KAZANSKIY, 2021; ZHANG et al., 2016). In the case of interferometric configurations, many devices were developed using silicon-on-insulator (SOI) platform that is compatible with the complementary metal-oxide-semiconductor (CMOS) fabrication processes but include some critical steps to create gaps or cavity sections (SUN; THYLÉN; WOSINSKI, 2017; MOHRI; ASAKAWA; SUZUKI, 2020). Other cases use sophisticated elements in order to optimize the operation as an optical attenuator and phase shifter in the reference arm, which allow to reach very high sensitivity (near to 2000 nm/RIU) (MANOLIS et al., 2019). In all these cases the fabrication process faces critical and additional steps than a simpler straight dielectric waveguide case. A simpler approach from an interferometric perspective was presented in (DEBACKERE et al., 2006), where the authors presented an Si waveguide interfacing the sensing medium with a 60 nm thick gold layer and a fixed sensor length of 10μm. The sensing achieved for this device is around 450 nm/RIU in an operation wavelength of 1550 nm. This result is very close to that obtained in (KWON, 2010) where a numerical simulation was approached for a Mach-Zehnder interferometer (MZI)-based sensor. In this case the sensing arm was based on a metal-insulator-silicon configuration and reaches a 430 nm/RIU in 1500 nm band.

On the side of ring resonator-based configurations, they take advantage of the metal-insulator-metal (MIM) structure to put in the insulator region the sensing medium and get high sensitivity values. Again, critical steps for fabrication and the crucial gap dimensions added, the ring and disk gold fabrication have to be overcome (ZHOU et al., 2011; BUTT; KHONINA; KAZANSKIY, 2018). However, a high sensitivity devices reported in (Chou Chau et al., 2021; CHAO et al., 2020a) are based on square or circle ring-shaped and includes silver nanorods, reaching sensitivities up to 2080 and 2500 nm/RIU.

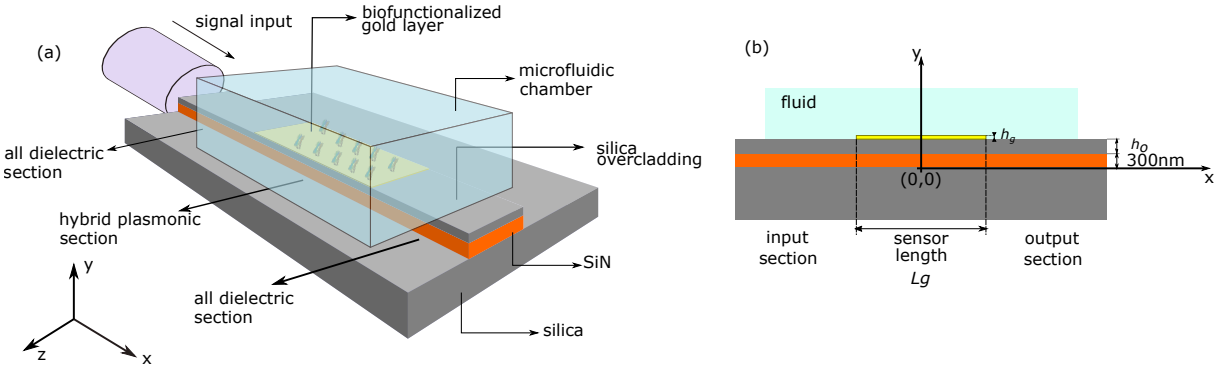

Figura 4.1 – (a) 3D view of our hybrid plasmonic dielectric sensor proposal. (b) Cross-section showing sensor input, region detection (indicated as sensor length) and output section along the propagation direction. We use the parameters: thickness of oxide and gold (h_o and h_g) and gold length (L_g) also called sensor length.

A similar and higher sensitivity structure is presented with a stub with silver nanorod defects, claiming a sensitivity of 5140 nm/RIU (CHAU, 2020). The inclusion of metal nanoparticles (NP) is recurring for HPWG devices in order to improve the sensitivity, like in (CHEN et al., 2016), where the configuration work on a synergy mechanism between localized surface plasmon resonance (LSPR) and propagating surface plasmon resonance (PSPR), reaching a sensitivity of 2600 nm/RIU. The use of LSPR falls outside of CMOS traditional fabrication process and, in this particular case, a MIM configuration has a special appeal. In the literature, many configurations seem quite complicated, as in (KAZANSKIY; KHONINA; BUTT, 2020), where the gold or silver film is disposed in a variety of patterns to improve the enhanced field in contact with the sensing medium. A fabrication challenge is to select the suitable method for metal molding commonly using the lift-off process or ion milling technique. It is possible to consider "simpler"structures those cases with squared ring resonator-based sensors (BUTT; KHONINA; KAZANSKIY, 2019; BUTT; KHONINA; KAZANSKIY, 2021; ZHANG et al., 2016) which reached important levels of sensitivity, of the order of 1000 nm/RIU but with hard manufacturing restrictions in their resonant structures like gaps between $15 - 45$ nm and 5 nm.

In this chapter, we detail the hybrid modes behavior analyzed in a simple HPWG structure, a straight SiN (silicon nitride) waveguide, cladding of SiO_2 (silicon dioxide or silica), and thin gold layer, for visible and part of near-infrared (NIR) spectrum. We evaluate its efficiency for biosensing applications, that is, for a fairly small refractive index variation range. In the design process, the length of the sensor region is taken into account and the impact of this parameter on the sensing performance is detailed. The results were obtained numerically using the finite difference method implemented in Lumerical's 2D-FDTD solver.

The structure of the proposed sensor is an integrated sensor using only a straight

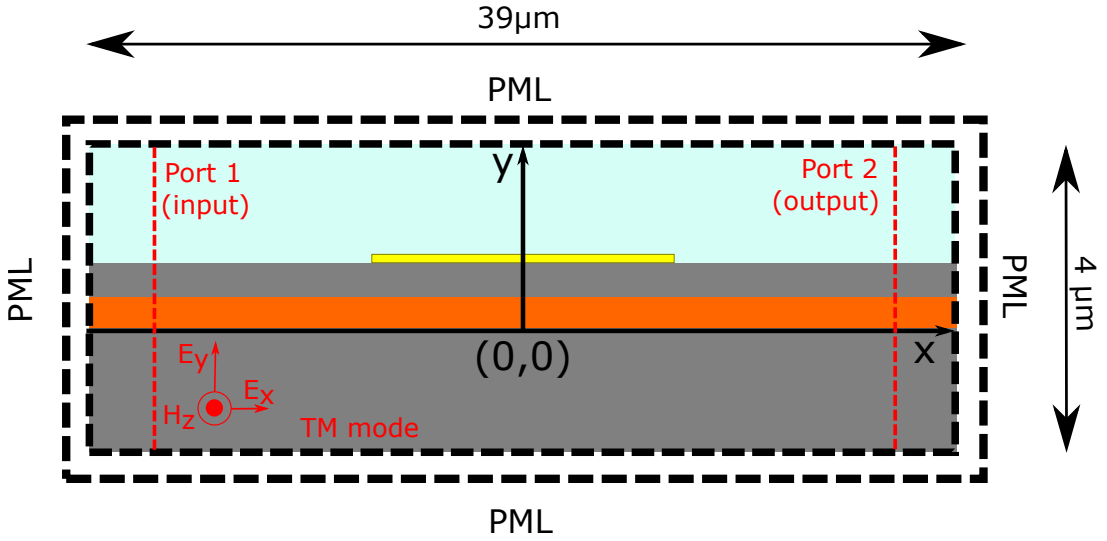

Figura 4.2 – Schematic of the simulated design.

waveguide that serves to detect refractive index changes. When the sensing medium, in contact with the gold layer, changes, the hybrid modes' behavior will shift according to new dispersion relation, so the resonance conditions will present also a spectral shift which can be tracked by the sensing system. Fig. 4.1(a) presents the 3D schematic of the sensor and Fig. 4.1(b) shows the cross-section of the sensor along the propagation direction. The sensor is composed of three parts: input section, hybrid plasmonic section, and output section. The input and output sections correspond to a SiN dielectric waveguide with a thickness of 300 nm over a SiO_2 substrate and with a top cladding SiO_2. The SiN layer has 300 nm thickness and it is compatible with the foundries specifications as IMEC. In the hybrid plasmonic section, we have a structure formed by a SiN guide over a SiO_2 substrate and top cladding by another silica layer with thickness h_o. A thin gold layer (with thickness h_g) is deposited over top cladding. This gold layer is put in touch with the sensing medium. The central section is a hybrid plasmonic section because their eigenmodes are formed for the coupling between dielectric and plasmonic modes (HOMOLA, 2006b).

Next we show the simulation model and fabrication considerations (Subsection 4.1.1), the details of the hybrid modes under analysis (Subsection 4.1.2) and the impact of top coating thickness and metal (Subsection 4.1.3) on the modal analysis and resonance, discussed qualitatively.

4.1.1 Simulation Model and fabrication considerations

We work on the 2D-FDTD simulation and modelling of the HPWG structure to analyze the sensing performance over the selected spectral band. In Fig. 4.2 is detailed the 2D model and the positions of the ports and PML contourn. Table 4.1 compiles the configuration specifications of the 2D-FDTD used to develop the analyze and get the results presented in this work.

Element	Definition	x axis	y axis
FDTD Simulation region	2D simulation region	$Length = 39\mu m$	$Length = 4\mu m$
Boundary conditions	Perfect Match Layers (all boundaries)		
Mesh condition	Mesh in all simulation region	$20nm$	$30nm$
Waveguide mesh	Mesh resolution on dielectric waveguide	$20nm$	$20nm$
Metallic film mesh	Mesh resolution on metallic region	$20nm$	$1nm$
Port	Port1: Modal source at the input (TM)	$x = -19\mu m$	$Length = 4\mu m$
Port	Port2: Port at the output (TM)	$x = 19\mu m$	$Length = 4\mu m$

Tabela 4.1 – Simulation model specifications.

The materials used are the Silicon oxide or Silica and Silicon nitride (both cases using the IMEC' dataset dielectric constants (IMEC, 2020)) and with Gold we use the Johnson and Christy database optical constants (P. B. Johnson and R. W. Christy, 1972). All this information was mounted on the commercial software Lumerical FDTD Solutions 2021 R1.2, where was configured the 2D simulation region.

The 2D simulation performs the behavior of the case on slab situation (infinite length on z-direction) which reproduces the real 3D case if all thin films (waveguide, oxide and gold) are quite wide compared to the operation wavelengths. The **TM** mode and the vertical coupling are in the same longitudinal plane, so all the physical parameters are taken into account, which allows to go from a 3D situation to a 2D one. Also these simulation results are approximate to the case of channel waveguide with the exception that the modal analysis have to take account the width's effect over the effective indexes of involves modes (feasible to perform based on the known Effective Index Method) (CHIANG, 1986). The main advantage of this 2D simulation is the great savings in computational cost, both in processing resources and in simulation time, which is very necessary given the large number of simulations required to identify the sensing behavior. Many examples of the correct use of 2D simulation instead of 3D are presented in works with MIM nanostructures for sensing (CHAU, 2020; CHAU et al., 2020; CHAO et al., 2020b).

The fabrication steps for fabrication are completely compatible to CMOS fabrication standard, based on process like photolithography (dielectric waveguide design), thin-film deposition as physical or chemical vapor deposition (for oxide deposition and gold deposition) and etching (to remove the protected region around the gold surface) (SAGMEISTER et al., 2018; IMEC, 2020; BAUDOT et al., 2017). This greatly facilitates

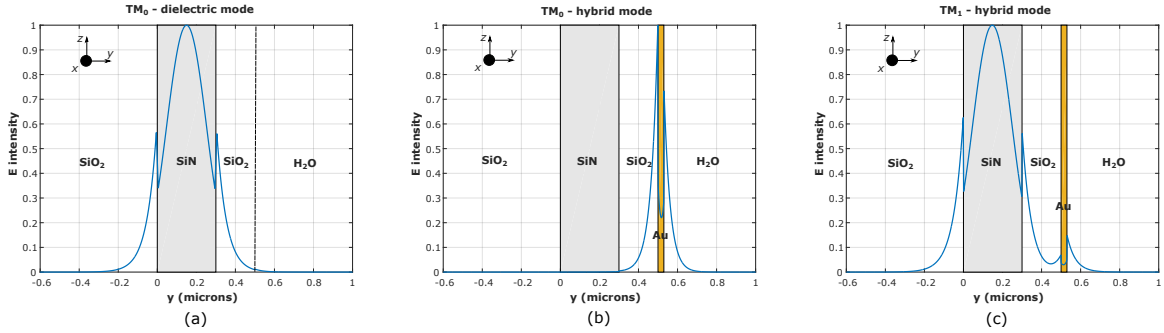

Figura 4.3 – Eigenmodes present in the dielectric region and hybrid region. (a) $\mathbf{TM_0}$ mode in the dielectric region (without the gold layer). (b) $\mathbf{TM_0}$ and (c) $\mathbf{TM_1}$ modes (also called supermodes in coupled-mode theory) in the hybrid region (dielectric and golden layer) with 30 nm gold layer over 200 nm silica layer at $\lambda = 600$ nm. The light direction propagation is the x axis, indicated in all sub figures and perpendicular to the page plane.

their potential mass manufacturing and avoids the use of more sophisticated procedures such as electron beam lithography or focused ion beam (FIB), which complicate and make the manufacturing process more expensive (DIETZEL et al., 2006).

4.1.2 Hybrid modes in SiN-SIO2 with thin gold layer

Figure 4.3 presents the eigenmodes explored that arise in the hybrid structure. In Fig. 4.3(a), we have the $\mathbf{TM_0}$ mode presented in the completely dielectric region, without the gold layer. This configuration makes up the input and output regions as are shown in Fig. 4.1(b). In the Figs. 4.3(b) and 4.3(c) are presented the dielectric-plasmonic modes or hybrid modes. Fig. 4.3(b) presents the $\mathbf{TM_0}$ plasmonic mode, which has most part of the energy around the metal film, high loss, and high confinement. Fig. 4.3(c) presents the $\mathbf{TM_1}$ plasmonic mode, more clearly a hybrid mode, because it presents an important portion of the field inside the dielectric core, while there is a small portion around to the metal surface. This modal analysis was obtained with 300 nm SiN, 200 nm silica top cladding and 30 nm gold thickness.

Figures 4.4 and 4.5 present the dispersion relation and propagation loss in the hybrid structure, respectively. Both analyzes were done using the 200nm silica top coating and 30 nm gold in a range wavelength of $400 - 1000$ nm. In the dispersion relation, it is possible to identify the regions with better conditions for coupling between modes. For shorter wavelength values we can see a high match between the completely dielectric mode (input waveguide) and the hybrid mode $\mathbf{TM_1}$, in a situation very close to the Figs. 4.3(a) and 4.3(c), where the field energy are majority inside the SiN waveguide. The plasmonic mode $\mathbf{TM_0}$ gets closer than dielectric mode curve since around 700 nm wavelength onwards there is an increase in surface energy at the oxide-gold interface that

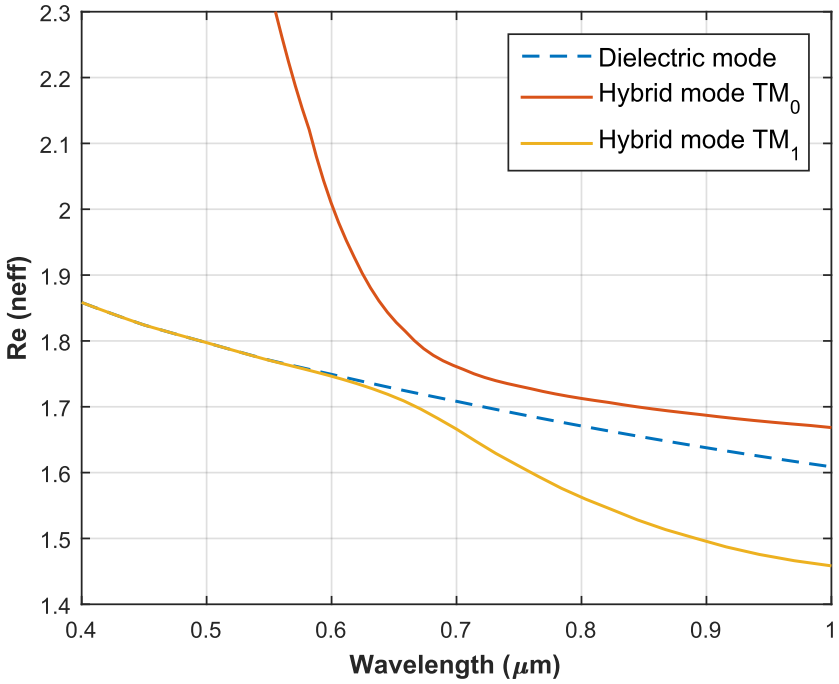

Figura 4.4 – Dispersion relation for the dielectric and hybrid modes ($\mathbf{TM_0}$ and $\mathbf{TM_1}$).

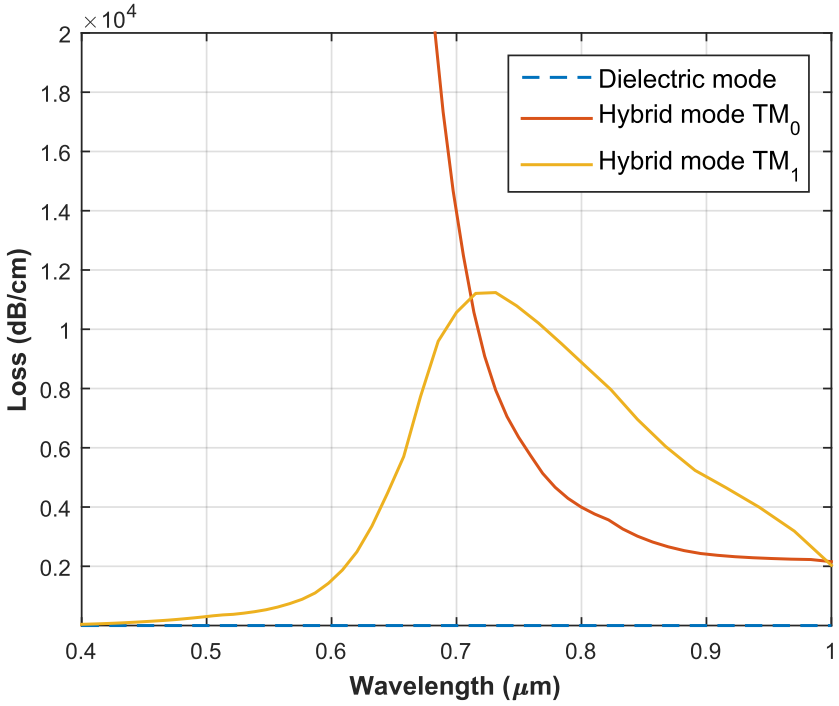

Figura 4.5 – Loss propagation in (dB/cm) as a function of wavelength for the dielectric and hybrid modes ($\mathbf{TM_0}$ and $\mathbf{TM_1}$).

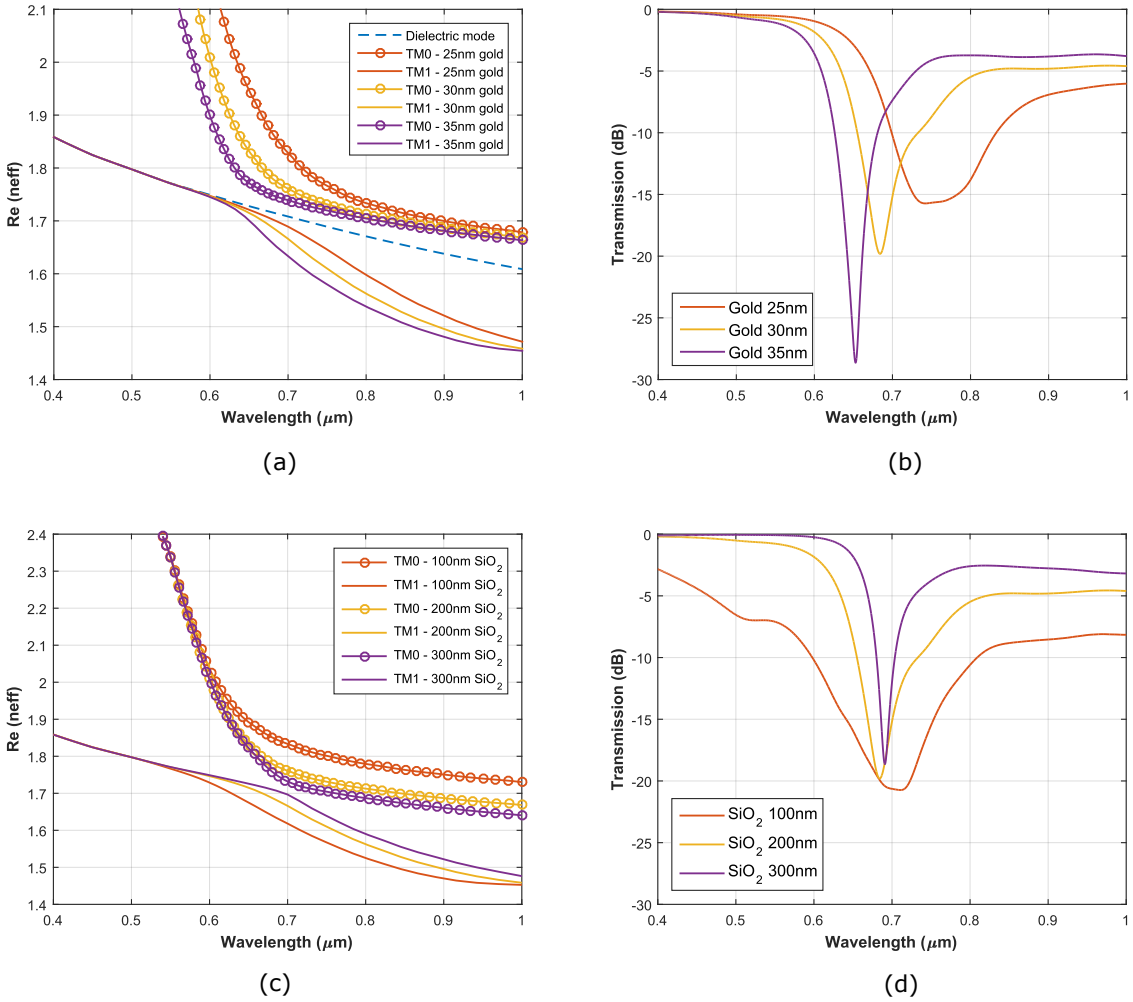

Figura 4.6 – (a) Impact of the gold layer thickness in the dispersion relation of the hybrid modes considering $h_o = 200\ nm$. (b) Transmission as a function of wavelength for 25 nm, 30 nm and 35 nm h_g values. (c) Impact of the silica top cladding thickness in the dispersion relation of the hybrid modes considering $h_g = 30\ nm$. (d) Transmission as a function of wavelength for 100 nm, 200 nm and 300 nm h_o values. $h_g = 30\ nm$ and $L_g = 15\mu m$, fluid index 1.3329.

begins to be guided by the silicon nitride waveguide. In the same way, this increase of operation wavelengths reduces the $\mathbf{TM_1}$ hybrid mode energy within the silicon nitride core leaking to the substrate with the subsequent decrease in the effective index.

Figure 4.5 shows that the propagation loss of the $\mathbf{TM_0}$ mode reduces its huge losses from around 700 nm wavelength, just when the field starts to be guided inside the dielectric core. The loss in $\mathbf{TM_1}$ mode behaves differently because it shows an important increase around 700 nm, a region where the mode field is accumulated around the metallic interfaces. In both cases we obtained the propagation loss from Equation 4.1 (HOMOLA,

2006b):

$$b = Im\{\beta\}\frac{0.2}{ln10} \tag{4.1}$$

Where b is the propagation loss in dB/cm and β is the propagation constant of the mode.

The approximation between the n_{eff} curves of the $\mathbf{TM_0}$ and $\mathbf{TM_1}$ modes with that of the input waveguide (Figure 4.4) determines the resonance region. This is where the transition from almost total coupling to $\mathbf{TM_1}$ mode to that of increasing coupling to $\mathbf{TM_0}$ mode occurs. It is crucial to identify that in this transition the plasmonic resonance of the device arises and that it is produced by the high loss presented by $\mathbf{TM_0}$ mode for shorter wavelengths. The discussion of this issue continues in the next subsection.

4.1.3 Impact of the gold and silica top cladding thicknesses

This subsection addresses the impact of the gold layer thickness that is in touch with the sensing medium. Fig. 4.6(a) shows the shift of the dispersion curves for $\mathbf{TM_0}$ and $\mathbf{TM_1}$ modes for 25 nm, 30 nm and 35 nm h_g values. In the same sense, Fig. 4.6(b) presents the transmission at the output of the device. We are going to analyze the relationship between these graphs and why Fig. 4.6(a) already foresaw the behavior shown in Fig. 4.6(b).

- *Case* $h_g = 25$ nm: The dispersion curve for $\mathbf{TM_0}$ and $\mathbf{TM_1}$ (red lines) begin to be closer to the dielectric mode (dashed line) around 750 nm. It means, the simultaneous transfer to both $\mathbf{TM_1}$ mode and $\mathbf{TM_0}$ mode happens in this value. This coupling involves an enormous loss because in this region both $\mathbf{TM_0}$ as $\mathbf{TM_1}$ present high loss. As we can see in Fig. 4.6(b), this is the resonance region, almost centered at 750 nm. Continuing in Fig. 4.6(a), for longer wavelengths the excited mode will be $\mathbf{TM_0}$, as the associated $\mathbf{TM_1}$ dispersion curve moves away. In this region there is no more resonance since the high loss associated with the $\mathbf{TM_0}$ mode is steadily reduced (from Fig. 4.5).

- *Case* $h_g = 30$ nm: The increase of gold layer shifts the dispersion curves for $\mathbf{TM_0}$ and $\mathbf{TM_1}$ modes (yellow lines). This time the curves are closer to the dashed line around 700 nm. The physical mechanism is maintained: the dielectric mode begins to excite both modes equally, both modes presenting a high loss. This is reflected as a blue shift of the resonance region in Fig. 4.6(b), this time occurring around 700 nm (yellow line).

- *Case* $h_g = 35$ nm: A new increase in the gold layer produces a new shift in the modal dispersion curves. Now the closest approximation of the $\mathbf{TM_0}$ and $\mathbf{TM_1}$ modes

(purple lines) is around 650 nm. Again, in this region is present a high loss reflected in the resonance region with a new blue shift, this time to 650 nm (Fig. 4.6(b) – purple line). The effect of the thickness of the gold layer on the resonance of the device is clear: a sustained blue shift as the gold layer thickens, explained from the modal behavior of the identified hybrid modes.

The effect of the thickness of the gold layer on the resonance of the device is clear: a sustained blue shift as the gold layer thickens, explained from the modal behavior of the identified hybrid modes.

In the case of the silica top cladding thickness, its impact is shown in Figure 4.6(c). In this case, there is no significant wavelength shift effect in which the dispersion curves of the $\mathbf{TM_0}$ and $\mathbf{TM_1}$ modes get closer, but there is an effect on how close the dispersion curves of these modes are. Thus, together with Figure 4.6(d) we can observe:

- *Case* $h_o = 100$ nm: There is a poor approximation between the dispersion curves of modes (red lines). Maximum coupling region around 700 nm. Resonance width value of 120 nm.
- *Case* $h_o = 200$ nm: The approximation between dispersion curves of modes (red lines) improve. Maximum coupling region is the same, around 700 nm. Resonance width value of 50 nm.
- *Case* $h_o = 300$ nm: Maximum approximation between dispersion curves of modes (purple lines). Coupling region remains around 700 nm. Resonance width value of 20 nm.

The impact of these widths, as FWHM values, in the performance of the sensors are more discussed on Section 4.3.

At this point we must highlight three issues:

i) The transmission curves of Fig. 4.6(b) present three regions: (a) high transmission region (for shorter wavelengths), (b) resonance or minimum transmission region and (c) again a high transmission region for longer wavelengths. This behavior is explained by the modal curves in Fig 4.6(a) together with the behavior of the losses of each mode in Fig. 4.5. In region (a) there is a maximum coupling to the $\mathbf{TM_1}$ mode, which presents very low losses in this region. Region (b) is where the resonance is produced as a result of a simultaneous coupling to both the $\mathbf{TM_0}$ and $\mathbf{TM_1}$ modes, both presenting a high propagation loss. Finally, region (c) where a coupling to the $\mathbf{TM_0}$ mode is mainly produced, which presents a lower propagation loss.

ii) The transmission curves in Fig. 4.6(b) also show a narrow resonance as the gold layer increases. This can be partially explained also by the modal curves in Fig. 4.6(a). The proximity between the $\mathbf{TM_0}$ and $\mathbf{TM_1}$ modal curves becomes narrower as the gold layer thickens. This proximity causes the b region (resonance region) to become narrower, passing faster from the simultaneous excitation of both modes to the excitation of the $\mathbf{TM_0}$ mode. This transmission curve is also impacted by the behavior that occurs in region b, that is, the behavior of the excited modes $\mathbf{TM_0}$ and $\mathbf{TM_1}$ that will propagate in the sensing region simultaneously and that could be analyzed under a theory of coupled hybrid modes. This theoretical analysis is not addressed in this paper, but its effects are described in detail in Subsection 4.2.1, based on the length of the gold layer.

iii) The resonance in the transmission curves (Fig. 4.6(d)) also narrows as the oxide layer increases. Analogously to the previous case, this can be explained by the effect of the narrowing of the modal dispersion curves of Fig. 4.6(c). However, as shown in Subsection 4.2.1, the length of the gold layer also has an impact on the quality of this resonance.

4.2 Simulation results

Taking into account the range of action of the biosensors, simulations were carried out considering sample indices in the range of 1.3329 to 1.3347 (ZINOVIEV et al., 2011). The design parameters of the sensor are the thickness of the oxide top cladding, the thickness of the gold layer, and its length. The efficiency of any sensor is taken from the sensitivity (S), the full width at half minimum (FWHM), and the figure of merit (FOM). The sensitivity express the variation rate of the resonant wavelength (λ_{res}) due to the index change Δn of the sensing medium ($S = \Delta\ \lambda_{res}/\Delta n$), and the FOM is calculated from S/FWHM (HOMOLA, 2006b; KAZANSKIY; KHONINA; BUTT, 2020). So the behavior of these two parameters is the priority to take into account in the design process. The objective is to obtain the maximization of the sensitivity in the application range and the minimization of the FWHM that allows us to have a good performance with the consequent maximization of the FOM.

Figure 4.7 shows the field intensity behavior along the device in the 400 to 1000 nm wavelength range. This plot was obtained with $h_o = 200\ nm$, and $h_g = 30\ nm$ with $L_g = 15\ \mu m$. This intensity was captured with a linear field monitor along the central region of the dielectric guide (SiN) in a 39 μm simulation region. The minimum output intensity (at $x = 19.5\mu m$) is observed at about 700 nm (according to Fig. 4.6(b)). As discussed in Subsection 4.1.2, we can verify that for shorter wavelengths there is a high transmission, while for values greater than 600 nm the output power begins to decline

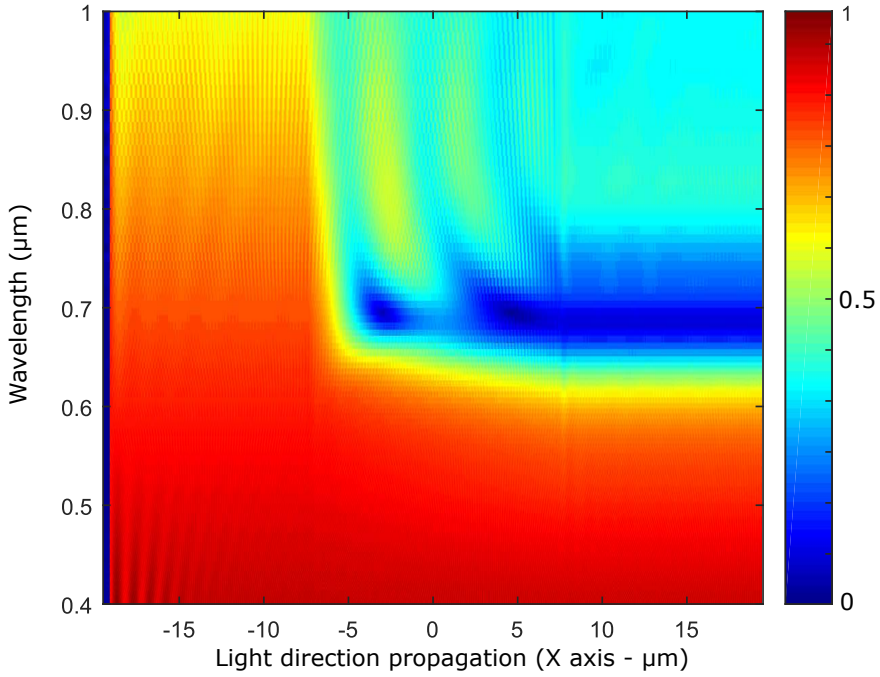

Figura 4.7 – Field intensity at the center of the SiN waveguide along all propagation regions. The wavelengths where the transmission begins to be affected by plasmonic excitation and where the power is minimal (resonance) can be clearly distinguished at the output of the sensing region ($x > 7.5\mu$m).

rapidly, until reaching a maximum absorption or 'resonance' dip. For wavelengths greater than 700 nm, power is partially recovered while an undulatory pattern in the field intensity (in the range $-7.5 < x < 7.5\mu m$) indicates a power exchange between the hybrid modes.

4.2.1 Resonance quality behavior

To analyze the resonance we will focus on the power exchange at the dip region (around $\lambda = 680\ nm$) whose field profile is shown in Fig. 4.8(a). The resonance condition at this wavelength is the product of a greater coupling to the $\mathbf{TM_1}$ mode and its high loss it has compared to longer wavelengths conditions. Fig. 4.8(b) shows the behavior of the field in this resonance condition. Despite having a high attenuation, it is still observed that there is a energy interchange that produces the fluctuation in the field intensity recorded in the SiN core.

Figure 4.8(c) shows the transmission as a function of the wavelength and highlights the effect of the gold length on the quality of the resonance. As expected, the power coupled to the output guide fluctuates as a function of this intermodal power transfer behavior. It is observed from Figure 4.8(b) that with a gold length of 5 μm a point of minimum power is reached coupled to the output guide ("local minimum- Lm). Similarly, with about 8.5 μm length of gold it presents a point of "local maximum - LM"coupled

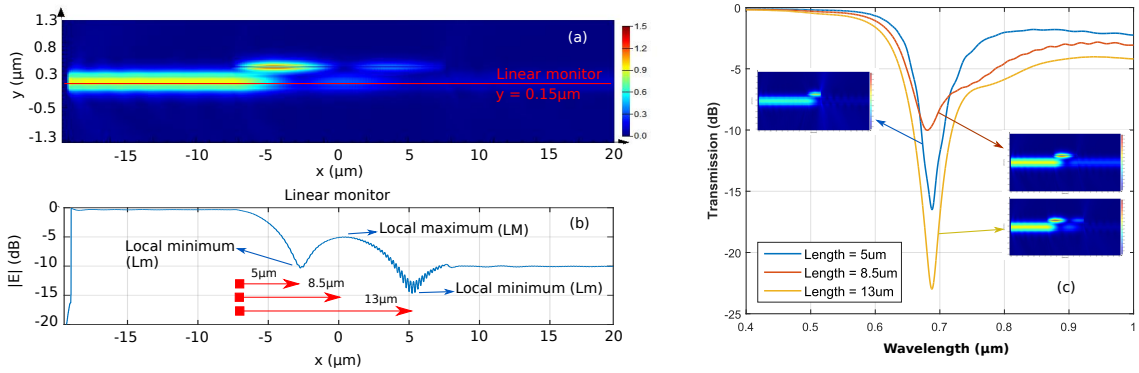

Figura 4.8 – (a) Field propagation in the resonant condition (around $\lambda = 684\ nm$) for $h_o = 200\ nm$, $h_g = 30\ nm$, and $L_g = 15\ \mu m$. (b) Electric field intensity along the center of the dielectric core captured with the linear monitor. (c) Sensor transmission for different L_g values considering 5 μm, 8.5 μm, and 13 μm.

power and with 13 μm, again an Lm coupled power. This power fluctuation directly impacts the FWHM values which are 40.5 nm, 110.9 nm, and 44.2 nm respectively. When there is a local minimum at the output, the FWHM get reduce and improves the quality of the sensor.

In order to quantify and set a classification with the sensor parameters (S, FWHM, and FOM) as a function of the gold length taking account the local minimum and maximum positions, a large number of simulations were carried out to capture each of these parameters for different gold length values from 5 to 32 μm. The gold length is hereinafter referred to as sensor length.

Figure 4.9 presents the parameters obtained for each sensor length value in four cases: the gold thickness of (a) 23 nm, (b) 25 nm, (c) 30 nm, and (d) 35 nm. All in the same configuration of 300 nm SiN and $h_o = 200\ nm$. It can be observed that there is a direct relationship between the behavior of the FWHM with that of the minimum transmission. When the transmission minimum is quite low with high plasmonic resonance, the FWHM is reduced, the dip becomes narrower, which means that the resonance presents better quality. However, a relationship with the behavior of sensitivity is not observed, which, under a thick look, behaves in an approximate uniform way, except with some peaks above or below the average. This explains why the behavior of the FOM curve is mainly defined by that of minimum transmission. Finally, this behavior is governed by the process of mutual coupling between the hybrid modes, which as the thickness of the gold increases, present the 'local minimum' positions for longer lengths.

4.2.2 Best Potential Case (BPC) identification

In order to identify the 'best potential cases - (BPC)' from this set of simulated structures, a compilation of S and FOM values has been made for cases with different top

cladding thicknesses (125 nm to 325 nm values) and different gold thicknesses (23 nm to 35 nm values). We call BPC those cases where the FOM is greater than 5 and represent a local peak such as the cases shown in Fig 4.9(a). This compilation is presented in Table 4.2, showing until four BPC with their respective sensor length, S and FOM.

In an illustrative way, we can explain Table 4.2 by describing the BPC obtained for 125 nm oxide thickness case. In the first row is the case for 23 nm gold. The BPC 1 is presented for a $L_g = 13$ μm, with an S of 601.79 nm/RIU and a FOM of 5.4. Since no other values are found to achieve BPC restriction, the BPC 2, 3, and 4 are empty. In the case of 25 nm gold, there are two BPC, the first for $L_g = 17$ μm and for $L_g = 21$ μm with sensitivity values greater than 600 nm/RIU and FOM of 6.5 and 5, respectively. In the case of h_g =30 nm, any BPC is reported and the cells are empty. For 35 nm gold, two

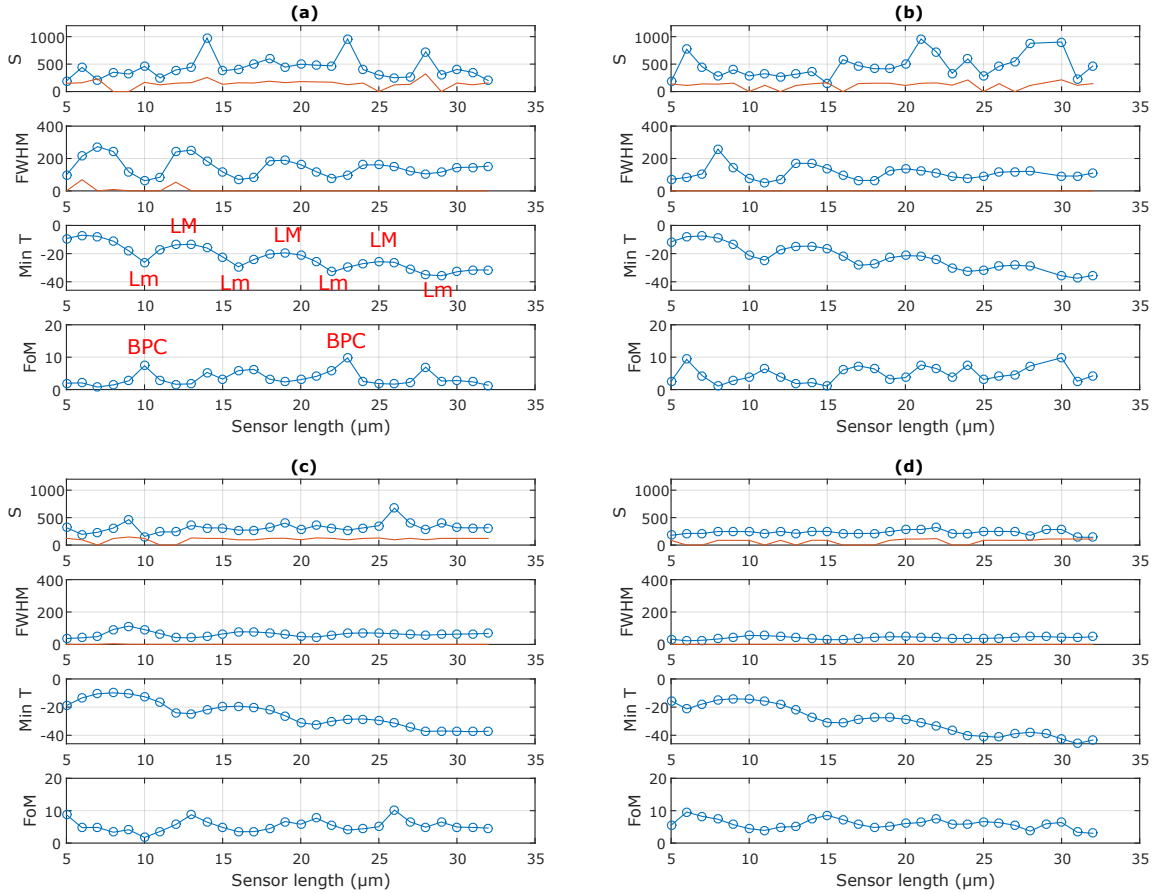

Figura 4.9 – For different sensor length values were captured the: Sensitivity - S [nm/RIU], FWHM [nm], FOM [RIU^{-1}] and the transmission minimum value - Min T [dB]. All cases present the predetermined configuration of 300 nm SiN with $h_o = 200$ nm. The gold layer thicknesses are: (a) 23 nm, (b) 25 nm, (c) 30 nm and (d) 35 nm. In (a) are indicated the 'local maximum - LM' and 'local minimum - Lm' positions and the Best Potential Cases (BPC). The red line present in the plots of S and FWHM are the standard deviation values. As seven points in the sensing range 1.3329-1.3347 were taken, six sensitivity values and seven FWHM values resulted, which were averaged.

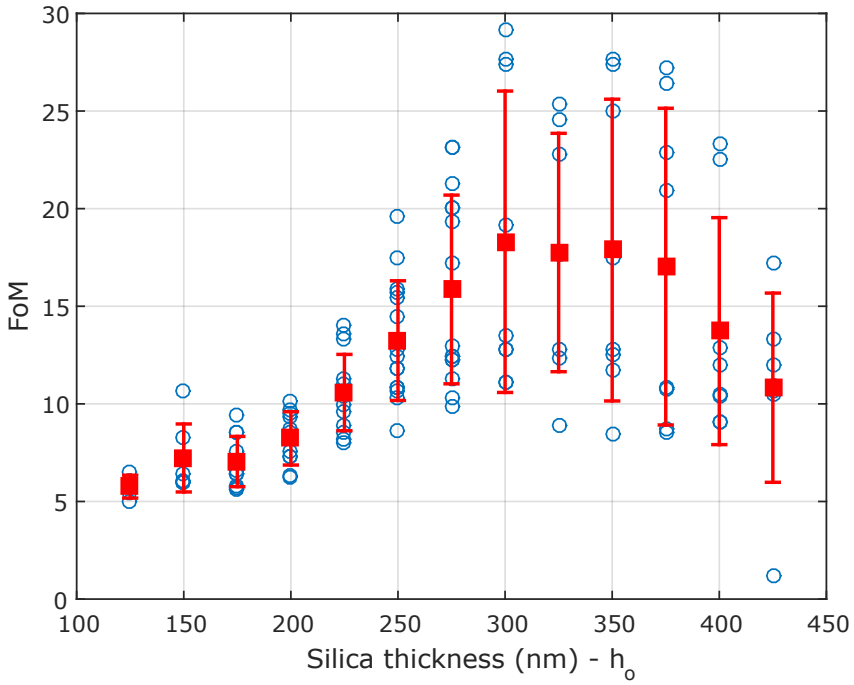

Figura 4.10 – FOM behavior with h_o values from 125 to 425 nm. Higher values were obtained around 300 nm thickness.

BPC are presented, for $L_g = 29$ and 30 μm respectively. This logic is applied to all the rows of the table.

With the data from Table 4.2 implemented in Fig. 4.10, we can see that the thickness of the oxide delimits a region where the FOM is maximum, on average. For cases from 125 to 200 nm, the average value of the FOM does not exceed 9 RIU^{-1}. For greater thicknesses, the value of FOM begins to grow until it reaches a maximum average value around 20 RIU^{-1}, and from 350 nm onwards this average begins to decrease steadily. The values of Table 4.2 shows that this behavior is due to a sustained reduction in the FWHM, which favors or limits the sensor quality.

An analogous behavior we can observe as a function of the thickness of the gold layer. The greater the thickness of gold, the sensitivity tends to decrease. All sensitivity values greater than 800 nm/RIU were obtained with thin thicknesses (3 of the 9 cases with a thickness of 25 nm and the remaining with a thickness of 23 nm). Sensitivities values greater than 900 nm/RIU happens only with 23 nm gold thickness. This behavior is expected given the evanescent nature of plasmonic sensors, however, a deeper discussion on this matter will not be addressed in this paper. As a theoretical reference on this aspect we recommend (HOMOLA, 2006b). These general trends are graphically expressed in Figure 4.10 and Figure 4.11, clearly showing the impact of oxide and gold thickness on FOM and sensitivity, respectively.

Thickness		Best Potential Case 1			Best Potential Case 2			Best Potential Case 3			Best Potential Case 4		
h_o	h_g	L_g	S	FOM	L_g	S	FOM	L_g	S	FOM	L_g	S	FOM
[nm]	[nm]	[μm]	[nm/RIU]	[RIU^{-1}]	[μm]	[nm/RIU]	[RIU^{-1}]	[μm]	[nm/RIU]	[RIU^{-1}]	[μm]	[nm/RIU]	[RIU^{-1}]
125	23	13	601	5.4	-	-	-	-	-	-	-	-	-
125	25	17	800	6.5	21	638	5	-	-	-	-	-	-
125	30	-	-	-	-	-	-	-	-	-	-	-	-
125	35	29	575	5.8	30	634	6.1	-	-	-	-	-	-
150	23	19	1191	6.4	20	992	8.3	-	-	-	-	-	-
150	25	12	836	10.7	-	-	-	-	-	-	-	-	-
150	30	8	318	6.1	13	398	7.1	14	429	6	-	-	-
150	35	9	249	6	-	-	-	-	-	-	-	-	-
175	23	8	521	6.4	-	-	-	-	-	-	-	-	-
175	25	13	799	5.7	14	381	5.6	20	466	6.4	-	-	-
175	30	10	357	8.5	17	394	6.6	23	357	5.8	28	680	9.4
175	35	5	247	7.6	11	285	8.5	18	320	7	24	575	10.4
200	23	10	459	7.3	17	504	6.2	23	959	9.7	28	724	6.9
200	25	6	770	9.3	17	470	7.3	24	593	7.6	30	902	9.8
200	30	13	355	8.7	26	672	10.1	-	-	-	-	-	-
200	35	6	213	9.5	15	248	8.5	22	320	7.54	30	283	6.3
225	23	12	561	11.3	19	624	8.9	28	914	8	-	-	-
225	25	6	770	9.3	17	470	7.3	24	593	7.6	30	902	9.8
225	30	7	314	11	16	356	10.6	17	315	10.4	25	357	8.2
225	35	8	248	13.6	9	248	14	22	248	10	32	391	10.7
250	23	6	862	15.7	8	797	10.7	15	665	12.88	23	568	8.6
250	25	7	602	14.5	16	422	10.3	26	611	10.8	-	-	-
250	30	9	316	15.9	10	315	12.4	20	397	11.8	21	317	10.8
250	35	12	213	15.4	13	248	19.6	14	213	17.5	24	319	11.8
275	23	7	462	12.3	18	513	10.3	27	730	9.9	-	-	-
275	25	8	563	23.1	17	809	11.3	20	469	12.4	21	468	12.3
275	30	12	277	17.2	13	316	20	27	357	12.4	30	317	13
275	35	24	249	20	25	249	21.3	26	248	23.1	27	248	19.3
300	23	9	618	19.2	22	569	12.8	32	1043	13.5	-	-	-
300	25	10	707	27.4	22	615	11.1	25	518	12.8	-	-	-
300	30	19	317	27.6	20	317	29.2	-	-	-	-	-	-
300	35	15	322	11.1	-	-	-	-	-	-	-	-	-
325	23	11	519	24.55	20	1035	12.3	29	621	12.8	-	-	-
325	25	14	518	25.31	15	470	22.7	-	-	-	-	-	-
325	30	32	318	17.7	32	318	17.7	-	-	-	-	-	-
325	35	30	251	8.9	-	-	-	-	-	-	-	-	-
350	23	15	624	25	30	731	12.8	-	-	-	-	-	-
350	25	22	471	27.3	23	518	27.6	-	-	-	-	-	-
350	30	19	400	11.7	32	359	12.5	-	-	-	-	-	-
350	35	16	542	17.4	27	252	8.4	-	-	-	-	-	-
375	23	21	573	26.4	22	573	27.2	-	-	-	-	-	-
375	25	30	520	20.9	32	520	22.9	-	-	-	-	-	-
375	30	19	403	10.8	29	361	10.7	-	-	-	-	-	-
375	35	22	252	8.7	32	252	8.5	-	-	-	-	-	-
400	23	31	575	22.5	32	575	23.3	-	-	-	-	-	-
400	25	30	524	12.9	32	476	12	-	-	-	-	-	-
400	30	30	362	10.4	32	362	10.5	-	-	-	-	-	-
400	35	30	252	9.1	31	252	9.1	-	-	-	-	-	-
425	23	31	580	12	32	632	13.3	-	-	-	-	-	-
425	25	20	964	17.2	31	526	10.9	-	-	-	-	-	-
425	30	26	363	10.7	30	363	10.5	-	-	-	-	-	-
425	35	31	253	1.2	-	-	-	-	-	-	-	-	-

Tabela 4.2 – Results compilation of Sensitivities (S) and Figure of Merit (FOM) for different thicknesses combinations of silicon oxide (h_o between $125 - 425\ nm$) and gold (h_g between $23 - 35\ nm$). For each combination, up to four BPC are presented, with their respective values of length (L_g), S, and FOM. Oxide thicknesses between 175 and 275 nm allow collecting various BPC with high performance, unlike low thicknesses ($h_o = 125\ nm$) and higher ($h_o > 325\ nm$) where there are fewer high-quality sensors.

Author	Year	Description	Wavelength Range [nm]	Medium sensing (RIU)	S [nm/RIU]	FOM [RIU^{-1}]
Debackere, et.al. (DEBACKERE et al., 2006)	2006	Sensor based on Surface Plasmon interferometer in a thin layer of gold embedded in a silicon WG. Gold length approximately 10 μm.	1400-1600	1.2-1.4	463.5	-
Kwon, et.al. (KWON, 2010)	2010	Sensor based on plasmonic MZI interferometer. Waveguide based on Si_3N_4 core and SU8 cladding and thin gold film in the sensing section. Gold length until 5.5 μm.	1450-1650	1.29-1.44	430	-
Zhang, et.al. (ZHANG et al., 2016)	2016	Sensor based on MIM waveguide coupled with double rectangular cavity. Gap between WG and cavities 5 nm. Cavities of 10×100 nm.	480-800	1-1.05	596	7.5
M. Butt, et.al. (BUTT; KHONINA; KAZANSKIY, 2019)	2018	Sensor based on MIM waveguide with squared ring resonator design. Gap between WG and resonator between $25 - 45$ nm.	1200-1800	1-1.1	1200	19.7
M. Butt, et.al. (BUTT; KHONINA; KAZANSKIY, 2021)	2019	Sensor based on MIM waveguide with squared ring resonator design. Gap between WG and resonator of $15 - 35$ nm.	1300-1800	1-1.2	1320	16.7
Y. Chou Chau, et.al. (CHAU, 2020)	2020	Sensor based on MIM 50 nm-width waveguide with stub: 50 nm width and 500 nm length (best performance). Nanorods with 20 nm radius.	500-6000	1-1.5	5140	-
Y. Chou Chau, et.al. (CHAU et al., 2021)	2021	Sensor based on MIM 50 nm-width waveguide with elliptical-ring resonator, gap waveguide-ring of 10 nm. Nanorods with 20 nm radius.	400-1500	1.335-1.385	2600	60
Fernandez, et.al. [This work]	2022	Sensor based on HPWG with a thin layer of gold and SiN core with a Silica overcladding. Gold length between 5 to 32 μm.	400-1000	1.3329-1.3347	707	27.4
Fernandez, et.al. [This work]	2022	Sensor based on HPWG with a thin layer of gold and SiN core with a Silica overcladding. Gold length between 5 to 32 μm.	400-1000	1.3329-1.3347	1191	6.4
Fernandez, et.al. [This work]	2022	Sensor based on HPWG with a thin layer of gold and SiN core with a Silica overcladding. Gold length between 5 to 32 μm.	400-1000	1.3329-1.3347	964	17.2

Tabela 4.3 – Comparison table with other similar works.

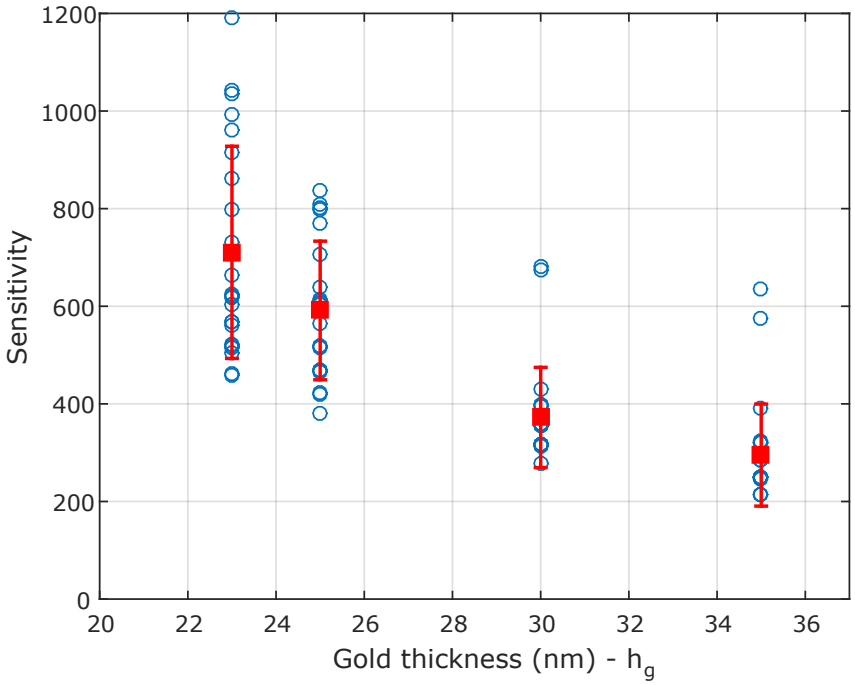

Figura 4.11 – Sensitivity behavior in relation with h_g values from 23 to 35 nm. The thicker the gold, the sensitivity decreases steadily.

4.3 Results discussion and design roadmap

In this way, we can arrive at the conclusion that the best configuration for the HPWG sensor of this type is oxide thicknesses values around 300 nm and very thin gold thicknesses. However, we must take into account the initial restrictions that we assume. For example, the lower limit of the thickness of gold was taken $h_g = 23\ nm$, due to source considerations with a limit of up to 1000 nm of wavelength. For thinner thicknesses gold layers, a redshift and a resonance broadening are obtained (higher FWHM) become them inappropriate to perform an analysis in the selected band. A greater thickness of oxide will increase the FOM, because while keeping the FWHM reduced, however on the other hand, this behavior is not more valid since 350 nm thickness, where the narrowness of the FWHM does not compensate for the low sensitivity achieved and the FOM values start decreasing.

The best configuration found for this type of 300 nm SiN core HPWG sensor is a top cladding oxide of h_o =300 nm and a gold layer deposition of h_g =25 nm thickness with L_g =10 μm. This device achieves a sensitivity of 707 nm/RIU and a FOM of 27.4 RIU^{-1}. Another important configuration with a high FOM is that of a $h_g = 30\ nm$ with $L_g = 20\ \mu m$ length, also for an oxide thickness of 300 nm. In this case, an FOM of 29.2 is obtained, although with a relatively low sensitivity of 322 nm/RIU. We can also highlight the case of higher sensitivity of 1191 nm/RIU for h_o =150 and h_g =23nm, $L_g = 19\mu m$, albeit with a low FOM of 6.4 RIU^{-1}. Another quite attractive case presents

S =964 nm/RIU and FOM = 17.2 RIU^{-1} in the configuration with h_o =425 nm and h_g = 25 nm, with $L_g = 20\mu m$.

4.3.1 Comparison with similar works

The main contribution of the present work is the modal analysis of the modes in the hybrid structure, as well as the mapping of the BPC for each addressed configuration. In this aspect, it is feasible to compare with a variety of works with similar structures found in the literature. Table 4.3 presents a list of values for S and FOM obtained in previous works.

As mentioned in the Introduction section, a series of ring resonator-based structures achieve high sensitivity and FOM values, however they present strong manufacturing restrictions, such as the fairly narrow gap between the MIM waveguide and the resonant structure. Thus, the references (BUTT; KHONINA; KAZANSKIY, 2019; BUTT; KHONINA; KAZANSKIY, 2021; ZHANG et al., 2016) are in the order of resonant nanostructures, with dimensions in the order of 25 nm waveguide thickness in rectangular dimensions below 500x500 nm (BUTT; KHONINA; KAZANSKIY, 2019; BUTT; KHONINA; KAZANSKIY, 2021) and 35x100 nm in (ZHANG et al., 2016). In none of the listed cases a FOM over 20 was obtained, although in (BUTT; KHONINA; KAZANSKIY, 2019) and (BUTT; KHONINA; KAZANSKIY, 2021) the sensitivity exceeds 1000 nm/RIU. It is important to highlight at this point the works also based on MIM that managed to overcome these marks by working with resonant cavities and stubs with silver nanorod defects (CHAU, 2020; CHAU et al., 2021), achieving sensitivities of up to 5240 nm/RIU and 2600 nm/RIU. In (CHAU et al., 2021) an FOM of 60 is reported. Again, these structures require nanofabrication techniques that allow defining, in both cases, nanorods with 40 nm diameter. For the (KWON, 2010) and (DEBACKERE et al., 2006) cases, the structures are much closer to that of the present work, although they are interferometric-based sensors. The values of sensitivities obtained are 430 nm/RIU and 463 nm/RIU respectively, the FOM are not reported.

In this way, it is verified that the present work reports novel performance values with a very simple micro-waveguide based sensor compatible with CMOS standard fabrication methods as mentioned above. The results were obtained based on evidencing the behavior of the hybrid modes involved in the plasmonic resonance.

4.3.2 Roadmap for design HPWG based sensor

From this experience we suggest the following roadmap for future designs in this type of sensors:

- Selection of the materials to work according to the feasible manufacturing conditions.

- Identify the operating range of the device based on the available characterization setup (source and spectrometer, in the case of wavelength interrogation).
- Determine the thickness of the dielectric core.
- Establish an initial thickness of the low-index material over the core.
- In the thin metal layer region take account higher mesh resolution for avoid weak simulation results.
- Identify the hybrid modes that appear in the structure in the operating range (as in Figure 4.3) and their modal analysis (Figures 4.4 and 4.5).
- Recognize the influence of the thickness of the low index material and the metallic layer (Figure 4.6) in the dispersion curves of the modes. These curves will give clues to the potential best settings.
- Identify the local maximums and minimums (LM and Lm), as well as the BPC for specific sensor configurations.

With this roadmap it is possible to identify BPC that can be potential starting points both for a subsequent manufacturing and testing process as well as for possible optimization algorithms that allow increasing the quality of the sensor.

4.4 Tests of pedestal HPWG

In this section the initial tests with the HPWG sensor under a pedestal structure are exposed. This experience was possible thanks to the collaboration with USP's Department of Electronic Systems Engineering (USP, 2022), who have extensive experience in the manufacture and characterization of pedestal guides. This was the first time that the pedestal-type guide produced at USP was used for plasmonic sensing tests from metallization with gold. This section presents both the fabrication and simulation aspects of the pedestal guide with the Ta_2O_5 material (Subsection 4.4.1 and 4.4.2) as well as the description of some tests carried out with the manufactured chips (Subsection 4.4.3).

4.4.1 Fabrication of pedestal waveguides

The advances in fabrication and optical analysis working in pedestal waveguides are compiled in (SIERRA et al., 2021), where two different mechanisms for pedestal architecture fabrication are described: one of them using Cr mask and the other does not make use of Cr mask. In the case of this work the fabrication process of this type of waveguides doesn't use Cr mask and the process is explained in (SIERRA et al., 2019).

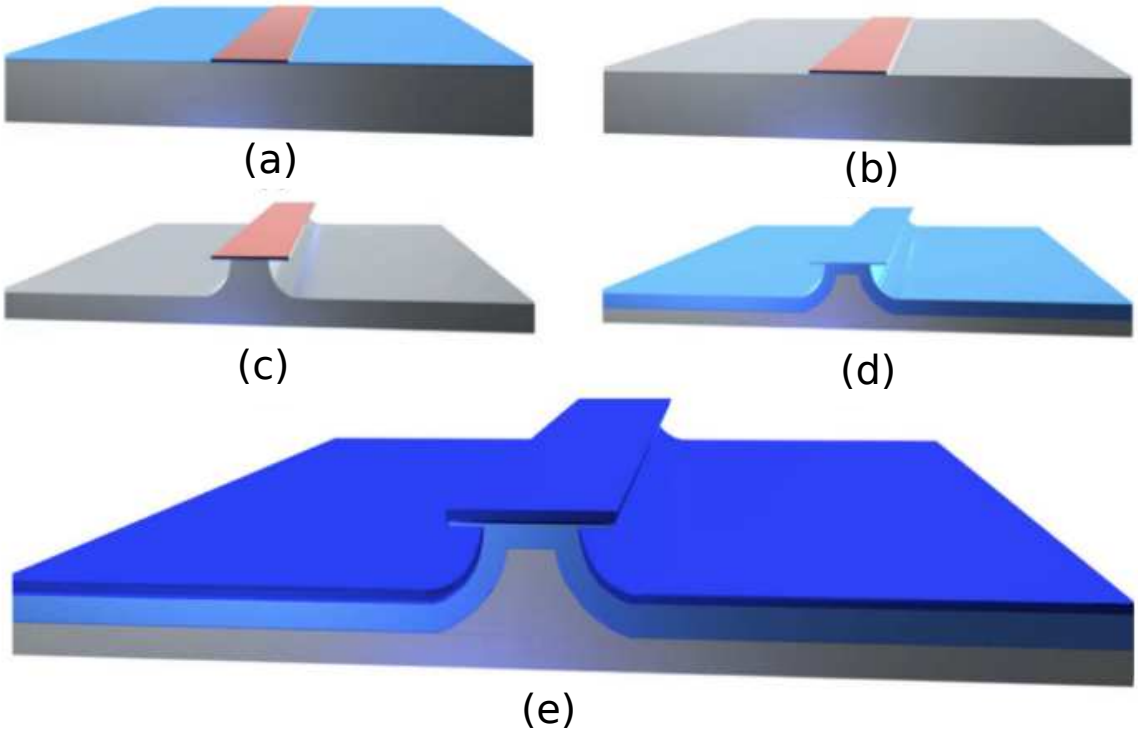

Figura 4.12 – Stages of the fabrication process of the pedestal waveguides: (a) Silicon oxide deposition and optical contact lithography. (b) Wet etch of silicon oxide layer. (c) Isotropic reactive ion etching of the Si substrate. (d) Thermal oxidation step. (e) Deposition of the Ta_2O_5 core layer.

The process is illustrated in Fig. 4.12 and it was done on p-type silicon wafers. After standard cleaning, a dry oxide growth process is performed inside a furnace at 1135 °C for 1 hour, in a H_2 and O_2 gaseous mixture, obtaining a thermal silicon dioxide (SiO2) with 150nm thickness (blue layer in Fig. 4.12(a)). Subsequently, a photolithography process is performed to define the waveguide geometry (Fig. 4.12(a)). After developing the photoresist, the oxide is wet etched (Fig. 4.12(b)) using Buffered Oxide Etch (BOE) for 2 minutes.

Figure 4.12(c) illustrates the isotropic etch of the silicon underneath the photoresist and the silicon dioxide layers. This is achieved with SF6 plasma (26 sccm flow), with 100W of RF power and 68 mTorr of pressure, for 3.5 minutes, leading to an etched structure 3.7μm deep. The photoresist stayed undamaged during the etch, protecting the SiO_2 layer. Figure 4.12(c) shows how the silicon underneath the thin silica layers is undercut, leaving a silica 'hat' which allows a controlled deposition of the devices' core, protecting the sidewalls of the pedestal. In addition, this shape isolates the waveguide from the lateral slab waveguides, avoiding coupling losses.

The subsequent step is a wet oxidation process at 1150 °C performed on the silicon wafer, creating a thick SiO_2 layer (1.65μm) underneath the silica 'hat' and in the lateral regions of the pedestal structure (Fig. 4.12(d)). This oxide is in fact the lower

cladding of the waveguides whereas the upper cladding is air. The refractive index of the thermally grown SiO_2 was measured using ellipsometry technique, and its value is 1.46. For this reason, the material used as a core must have a higher index to allow for total internal reflection (TIR) to take place inside the waveguide. The measured refractive index of Ta_2O_5 is 2.07. The core is deposited using the DC reactive sputtering technique (dark blue layer in Fig. 4.12(e)). The core is a $430nm$-thick layer of Ta_2O_5. The DC voltage used in the deposition process is $1.77kV$ and the total process time is 50 min.

4.4.2 Design of HPWG with Ta_2O_5 core

The HPWG sensor is described in (Fernandez H; RUMALDO; HERNANDEZ-FIGUEROA, 2022) and is made up of a dielectric core covered by a cladding with a lower refractive index and a thin layer of gold where the dielectric-plasmonic hybrid modes are produced. A schematic of this sensor making use of the pedestal structure is presented in Fig. 4.13.

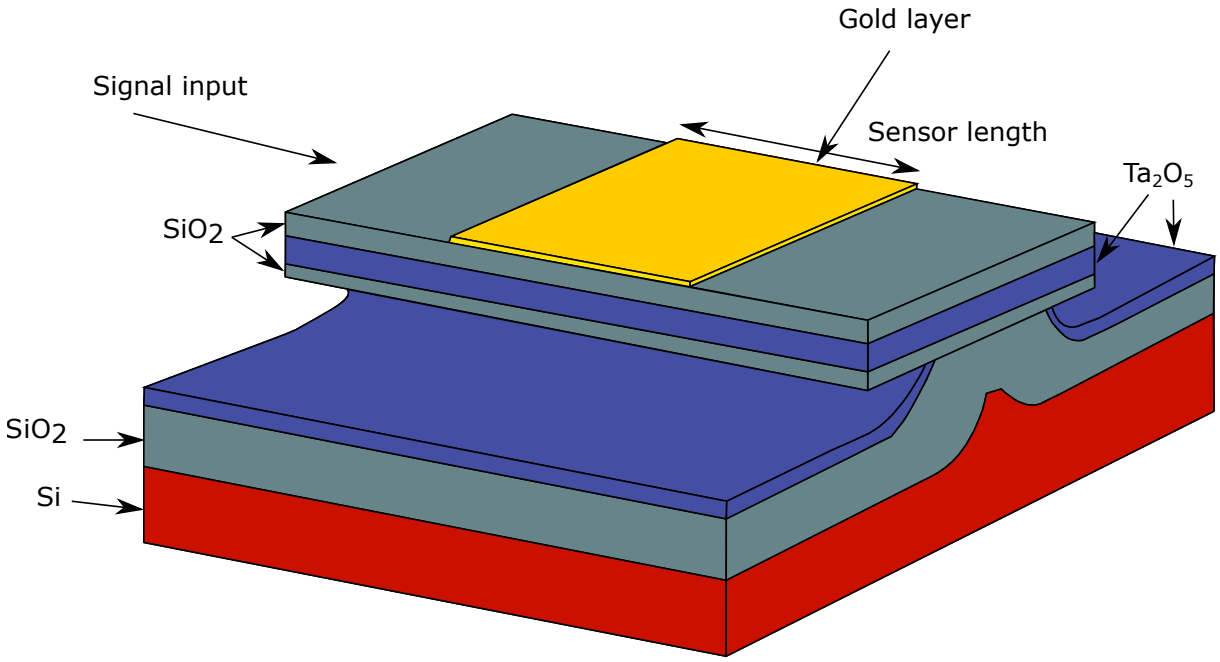

Figura 4.13 – Hybrid plasmonic - pedestal dielectric sensor schematic.

As a first step, we approximate the modeling of a rectangular pedestal waveguide with a strip-type rectangular waveguide, in order to simplify the 2D simulation. The dimensions used are $4\mu m$ wide with 400 nm high core, which are quite feasible to be fabricated (SIERRA et al., 2021). The plot of both structures is shown in Fig. 4.14, along with the respective $\mathbf{TM_0}$ modes. The dispersion curve of each of these modes is evaluated in Fig. 4.15, where a great approximation of the behavior of both modes can be observed in the wavelength range of 600 to 1000 nm.

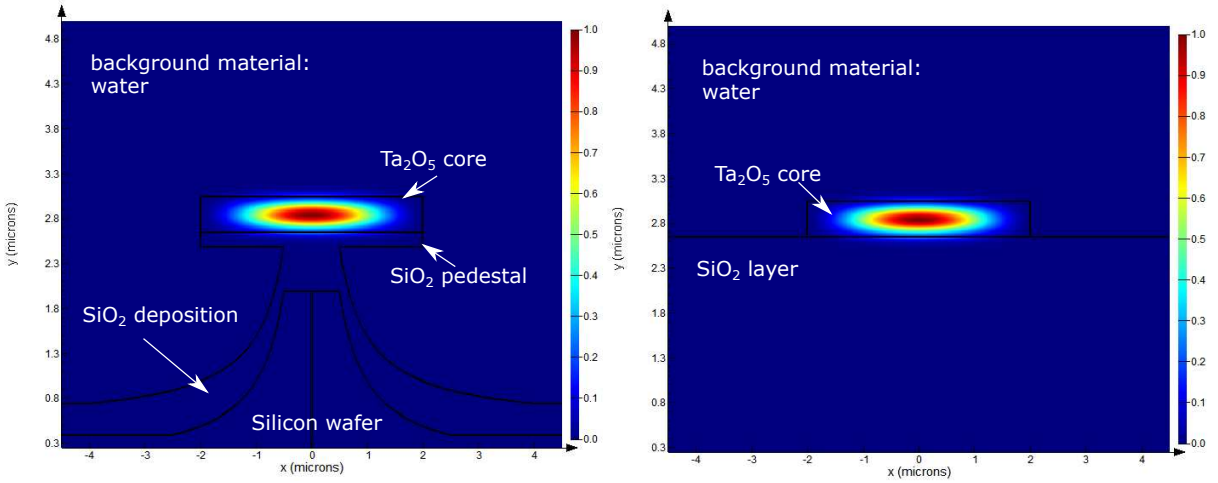

Figura 4.14 – Modal profile $\mathbf{TM_0}$ for pedestal guide and strip guide structures.

This fairly approximate behavior allows us to assume a similar behavior when modeling the hybrid pedestal waveguide with the hybrid guide as presented in previous section with the difference that in this case we replace the SiN for a Ta_2O_5 core.

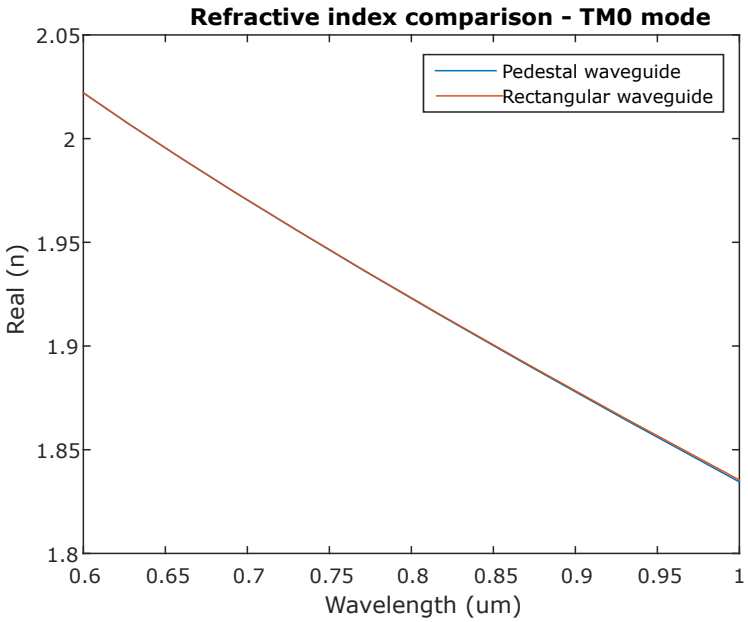

Figura 4.15 – Dispersion curve for pedestal and strip Ta_2O_5 waveguide.

In Fig. 4.16 the hybrid mode profiles of the interaction region for a wavelength of 800 nm are presented. It can be observed the hybrid modes $\mathbf{TM_0}$ and $\mathbf{TM_1}$ that will present the beating effect and will be responsible for the sensing in the interaction region.

In order to evaluate the performance of the devices in the biodetection range, simulations have been carried out where the refractive index of the external medium varies between 1.3329 and 1.3347 (ZINOVIEV et al., 2011).

Table 4.4 presents a compilation of sensitivity and FOM values for various

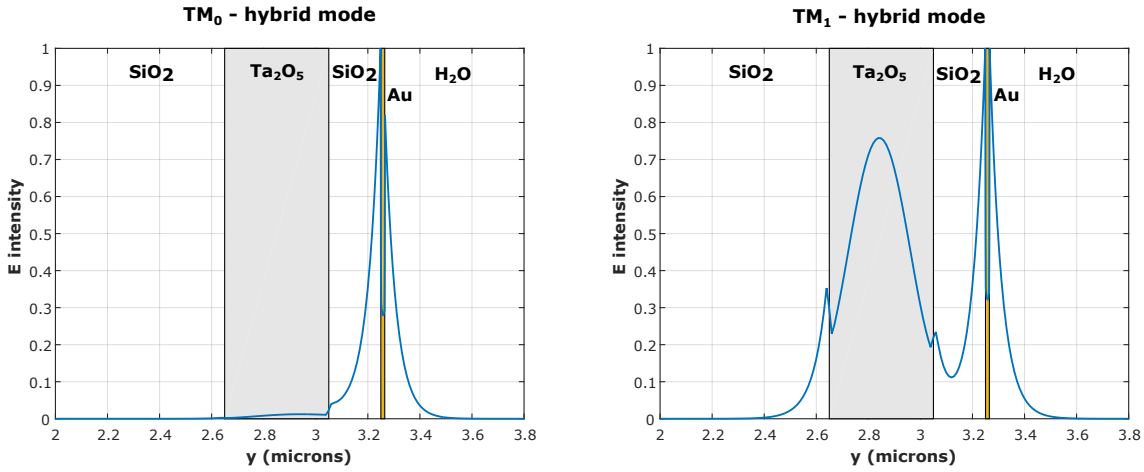

Figura 4.16 – Hybrid plasmonic-dielectric modes $\mathbf{TM_0}$ and $\mathbf{TM_1}$ in the interaction region at 800 nm wavelength operation and 15 nm gold thickness.

dimensions of the overcladding layer and gold thicknesses, the most prominent being those with 15 nm gold layer and 10μm length, which reaches a sensitivity of 556 nm/RIU and a FOM of 18 RIU^{-1}.

Tabela 4.4 – Compilation results.

Silica Thickness (nm)	Gold Thickness (nm)	Gold Length (μm)	Sensibility (nm/RIU)	FWHM (nm)	FOM (RIU^{-1})
200	15	10	556	30	18.5
200	15	20	560	64	8.7
200	15	25	555	64	8.7

4.4.3 Experimental setup and tests

The chips were fabricated at USP using a mask of straight guides with various widths, from 10 to 100μm. The thickness of the Ta_2O_5 core was 400 nm and the overclading oxide was 200 nm. The length of the gold layer deposited is 25μm with a projected thickness of 15 nm, as shown in table 4.4. A photo of the metalized guides is shown in Fig. 4.17.

The evaluation setup is shown in Fig. 4.18 showing the output of the NKT Photonics $390-2400$ nm supercontinuous laser (PHOTONICS, 2022), a free space optical attenuator, the Thorlabs linear polarizer to excite the **TM** modes in the guide and a objective lens that allows to focus the beam of light at the entrance of the guide. In Fig. 4.19 you can see the detail of the alignment with the inclined chip to guarantee the capture at the exit of the guided light only. The chip holder and the fiber that goes to the Thorlabs CCS175M spectrometer (THORLABS, 2022a) are also observed.

Several spectra were captured at the output of the guides, in such a way that it allows recording the change in the resonance wavelength for two media: with air and with

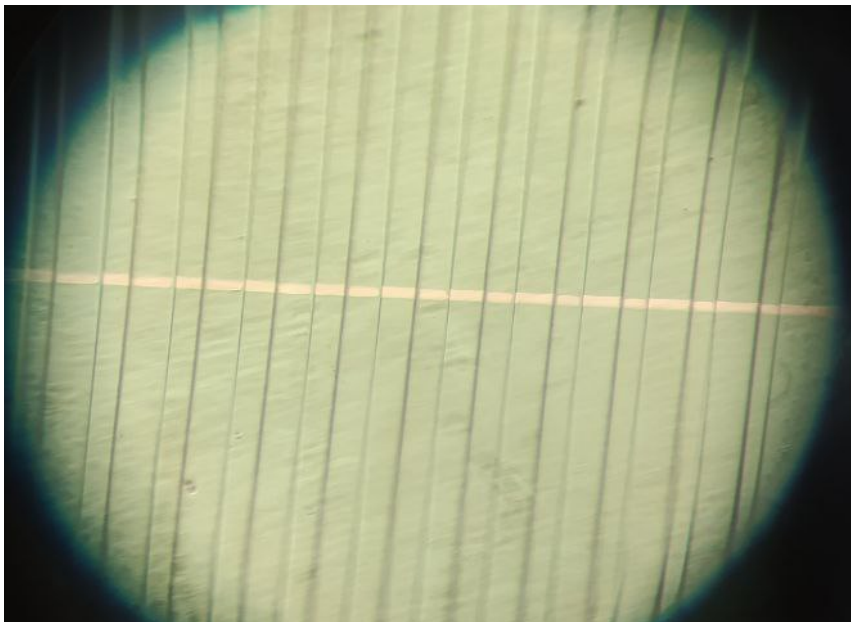

Figura 4.17 – Microscope picture of the metalizated detail in the pedestal waveguides. Metalized length: $25\mu m$.

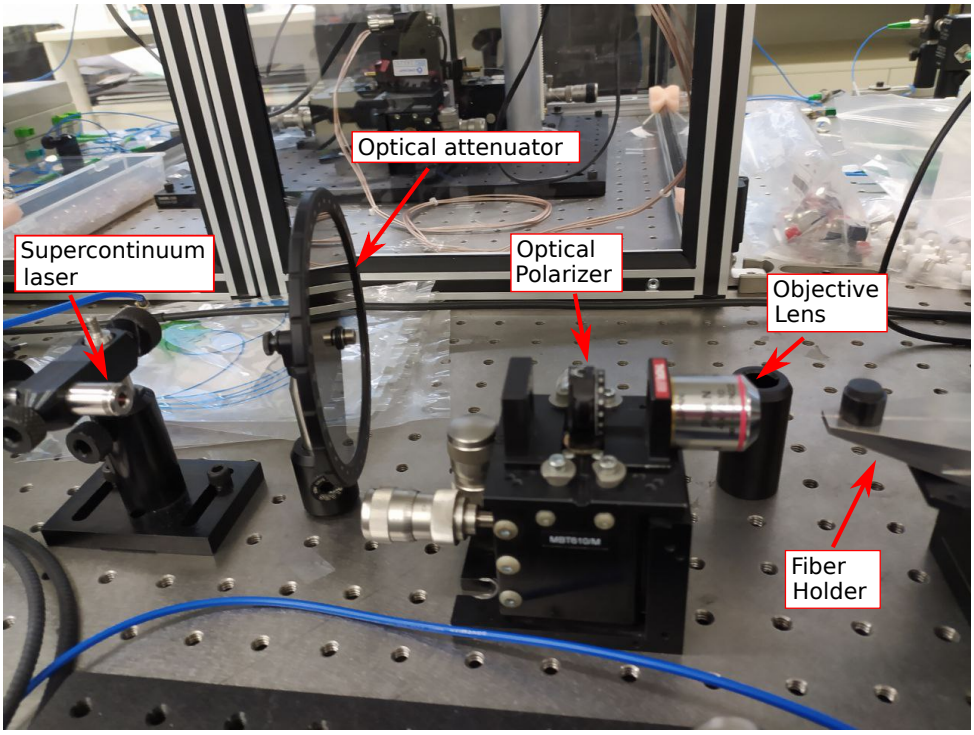

Figura 4.18 – Experimental setup with super continuous source, free space optical attenuator, 3-axis micropositioners with the linear filter and the objective lens.

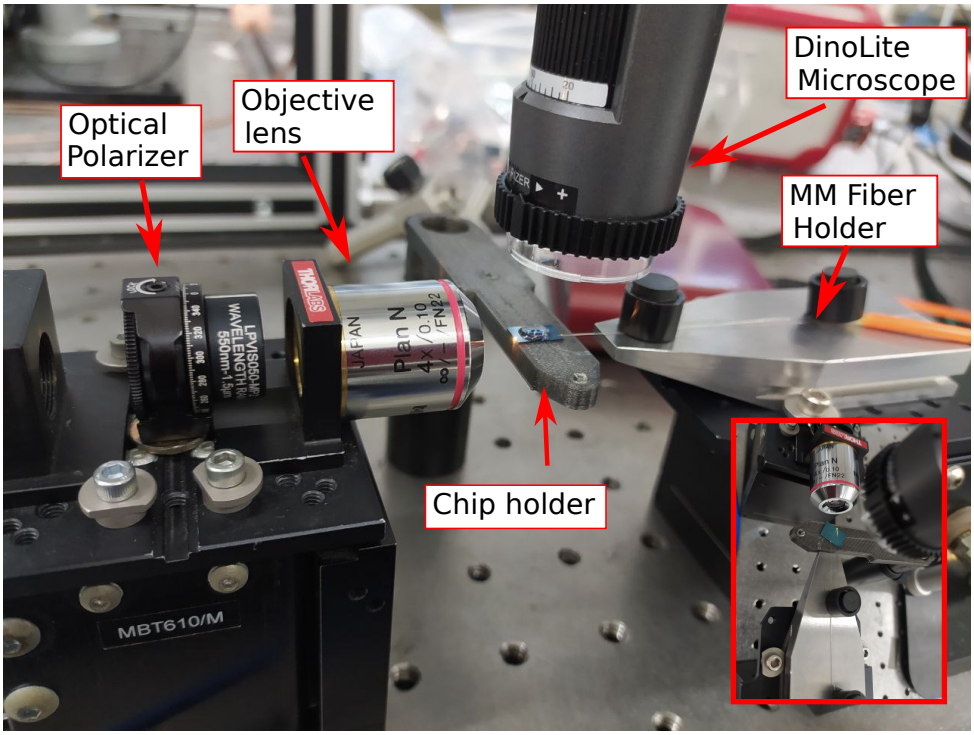

Figura 4.19 – Detail with the chip holder and the multimode optical fiber over the holder aligned. Inset: inclination of the chip in order to capture only the guided light with the multi-mode fiber.

water. The lack of a microfluidic channel and the inherent difficulties of working with a pedestal structure guide to avoid fluid spillage, limited the test to placing a drop of water directly on the chip.

Figure 4.20 shows the spectrum captured for the air case. The pink line is the **TM** spectrum while the black line shows the **TE** spectrum. As is known, the resonance is expected for the **TM** spectrum, so in this case the **TE** spectrum is taken as the reference signal. The light blue curve represents the normalized relationship **TM**/**TE**. It can be seen that there is a fairly wide dip between about 680 to 980 nm.

Figure 4.21 shows the same curves for the case of water. Compared to Fig. 4.20, a slight resonance shift to the right is observed, however a variation in the resonance peak is not clear.

In the case of a second guide we see a similar behavior. Figs. 4.22 and 4.23 show the spectrum in contact with air and with water respectively. Again some shift of the resonance to the right is observed but it is not entirely clear.

From both specific cases we have not been able to obtain conclusive statements but the development of the tests has left us the following lessons:

- For practical reasons, it is better to work with the widest guides with more than $20\mu m$ width.

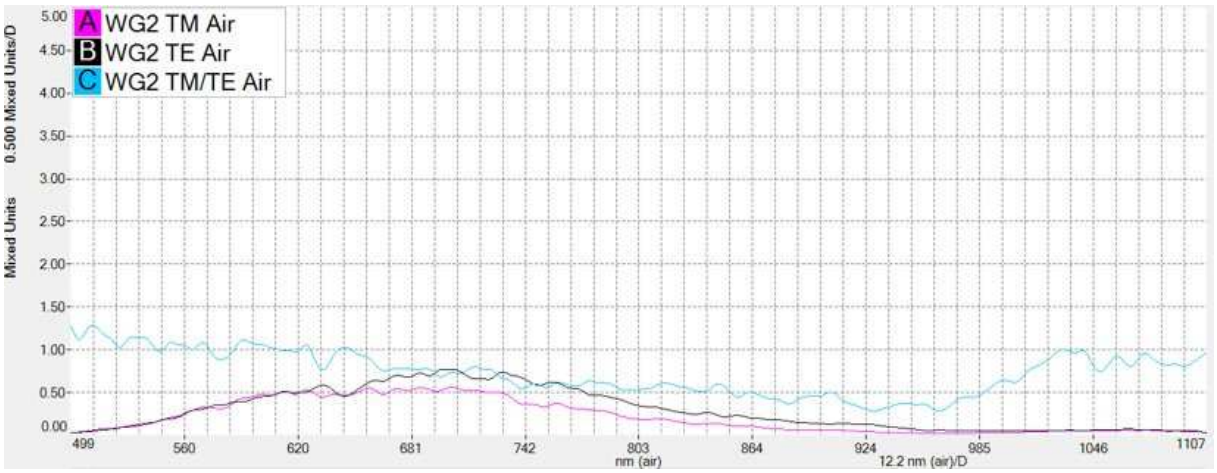

Figura 4.20 – Spectra at the output of the waveguide using air as dielectric media in contact with the gold layer.

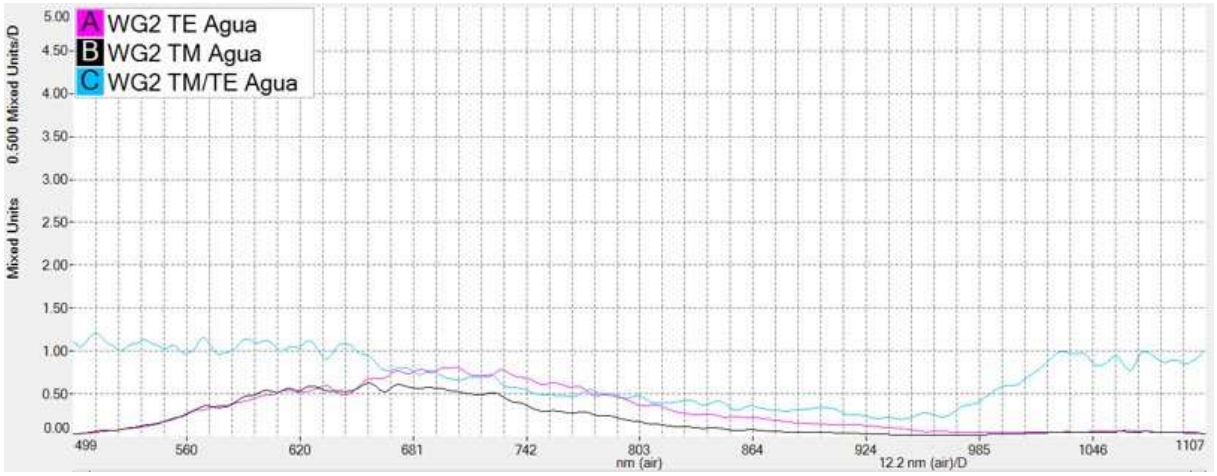

Figura 4.21 – Spectra at the output of the waveguide using a drop of water as dielectric media in contact with the gold layer.

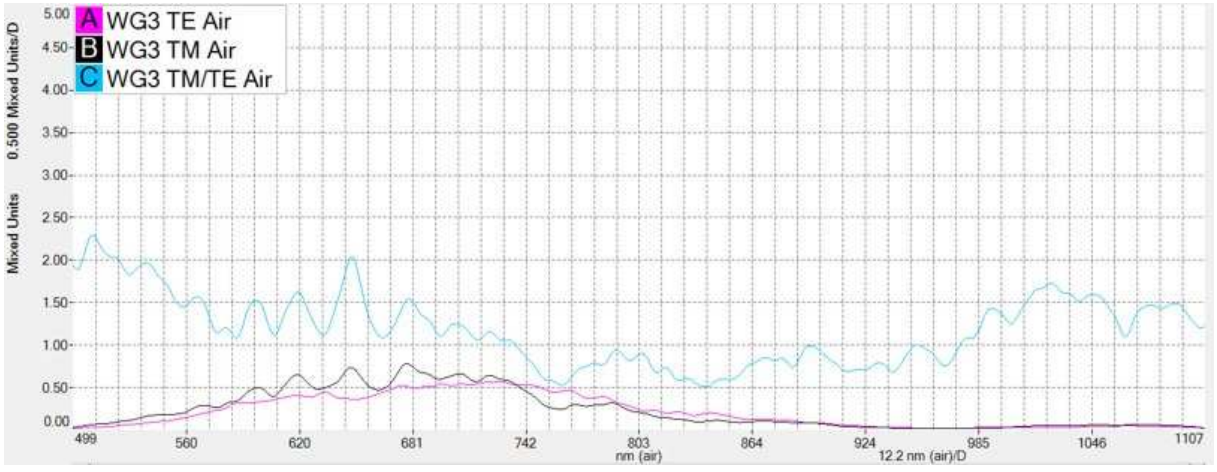

Figura 4.22 – Spectra at the output of the waveguide using air as dielectric media in contact with the gold layer.

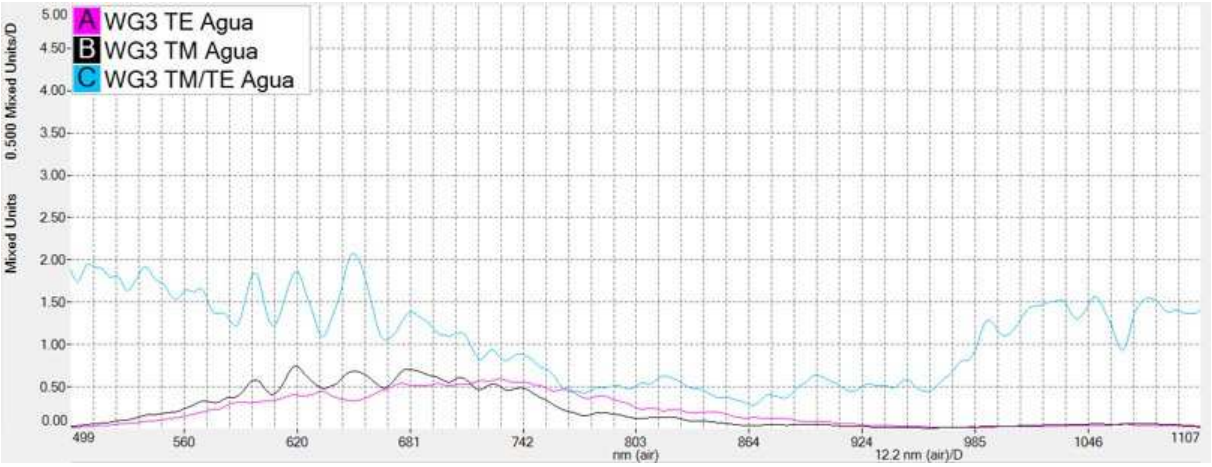

Figura 4.23 – Spectra at the output of the waveguide using a drop of water as dielectric media in contact with the gold layer.

- It is necessary to use a mask that allows having guides of the same width with and without metallization to compare not with the **TE** polarization but with the same **TM** polarization but without plasmon excitation. In addition, under the new mask, structures can be considered that allow perfecting the coupling and guiding, such as tapers and guides with curves.
- Try to implement a microfluidic circuit that allows the test to be carried out with different samples of different refractive index, avoiding spills.

5 CONCLUSIONS AND FUTURE WORKS

5.1 Prism coupling setup

5.1.1 Conclusions

- A functional Kretschmann configuration setup was developed from an ad hoc designed $\theta/2\theta$ rotation system. The electro-optical components were characterized and the mechanical structure improved with 3D parts. A graphical interface was developed to manage the system that allows identifying the resonance position and tracking for the sensing process.

- For angular scanning, the use of digital filters is necessary to reduce system noise, which allows reaching a sensitivity of up to $156°/RIU$ and a LoD of 2.3E-4 RIU, for refractive index values close to the of the water.

- With the same rotation setup, two intensity detection options were tested, using the S5870 photodetector and a DCU224M CCD camera. With the first one a LoD of 5.3E-4 RIU was obtained and with the last one it reached 2.8E-4 RIU.

- The impact of titanium and gold thicknesses on the sensitivity and performance of the sensor was analyzed. Numerical simulation was realized through the Fresnel reflection coefficient of a three layer structure and it was found that both the titanium layer and the gold layer influence the characteristics of the resonance and, therefore, of the sensor. In general, thicker gold layer gives better sensitivity in exchange of weaker resonances, while the influence of the titanium layer depends on the thickness of the gold layer being used. Moreover, experimental data was acquired with metal layers composed of a 2 nm titanium film and a gold film of 35, 50 and 75 nm. The results found were in great agreement with the theoretical ones. The greatest sensitivity found was $222°/RIU$ for a gold layer of 75 nm, showing an improvement of 11.8% and 38.4% in relation to the sensitivity for the gold layers with 50 nm and 35 nm. In the same way, the ER drops from 95% (35 nm-gold layer) to 55% and 18% (for 50 nm and 75 nm gold layers respectively). A low level of ER can be critical for high-noise experimental setups, however, for systems with low noise level, thicker gold layers can be used for bigger sensitivities, since low ERs are not a problem.

5.1.2 Future works

- The mechanical setup can be improved with more 3D printed parts, both for the case and for the holder of the components such as the prism and the photodetector. Integrated semiconductor laser diode types that can replace the He-Ne canyon laser can be tested in order to miniaturize the equipment. The Arduinos used can be integrated into a single electronic board along with the motor circuitry and photodetector for better electronic integration. Coupled with 3D printing these considerations can help build a working prototype of portable sensing.

- Development of an integrating GUI that allows managing the detection of the resonance curve, real-time monitoring by controlling the flow of samples and the post-processing for the detection of sensitivity and estimation of unknown samples.

- Study of the distortion of the laser wavefront due to the use of a hemispherical prism. This impacts the FWHM value which can be reduced with a narrower beam of light than the currently available or by using a triangular type prism. Other prisms with different materials could explored in this objective too.

- Exploration of other sensing setups such as angle scanning without mechanical rotation but by image sensor and incident beam with high numerical aperture. In this case, the semicylindrical prism is necessary together with a converging lens focused on the axis of the prism.

- Use of a spatial light modulator (SLM) to replace the mechanical rotation system with a rotation effect controlled electronically.

5.2 Waveguide coupling setup

5.2.1 Conclusions

- The design process of a hybrid plasmonic waveguide sensor based on a silicon nitride waveguide and gold layer has been presented. The design can be completely manufactured with planar technology and in the current CMOS microfabrication foundries. Although these types of sensors have lower sensitivity compared to the classic Kretschmann configuration and those based on fiber, their manufacturing process and miniaturization possibilities make it very feasible to be used in various LoC configurations for laboratories and applications.

- To the best of our knowledge, this is the first time that the waveguide-based plasmonic sensor has been subjected to a modal analysis of its first two hybrid modes, making explicit the impact of both the top cladding and metal thicknesses on the sensitivity

and other parameters of the device. Additionally, to put on evidence the gold layer length as critical parameter in order to optimize the sensor performance. Taking account all these considerations design, we found high sensing performances with S of 707 nm/RIU and a FOM of 27.4, also S of 1191 nm/RIU and 964 nm/RIU with FOM values of 6.4 and 17.2 RIU^{-1} respectively.

- This contribution paves the way for later works that use the same configuration with other materials or with other hybrid dielectric-plasmonic devices for different purposes. The exploitation of this design process for biosensing applications can be used for next stages such as 3D approach, fabrication, and designs that are oriented to intensity-based detection or as starting points for optimization or smart algorithms-based sensors.

- The first tests of the HPWG sensor could be carried out under a pedestal waveguide platform. Although the results were not conclusive, the complete setup for characterization could be implemented. This experience allowed deducing several tasks discussed in future works subsection.

5.2.2 Future works

- Carry out the mathematical model of the dielectric singlemode and plasmonic multimode intermodal coupling phenomenon that allows determining the length of the gold layer that presents the highest sensitivity in the HPWG scheme.

- The development of an online calculator of the hybrid dielectric-plasmonic coupling that provides the main coupling parameters based on the dimensions and materials considered. To the best of our knowledge, this online application is not currently available and it can be quite useful for the design of devices that are based on this technology.

- Development of lithography masks for the development of pedestal guides with taper and curves that allow optimizing the source-chip and chip-fiber coupling for the spectrometer. In the case of pedestal guides, it is also interesting to explore the design of broadband grades for vertical coupling, or the development of broadband polarization controllers, which allow obtaining a **TM** without the need for an external filter on the chip. These aspects can also be worked on for strip-type waveguides.

- Realize a resonance detection platform that can connect with the Thorlabs spectrometer used. In this way, real-time monitoring of the resonance displacement and the detection of the refractive index change can be carried out.

5.3 Further future works

- A first approximation was made for plasmonic sensing with exposed core fibers (ECF). This line of work with plasmonic sensors using fiber platforms can be resumed as it presents several advantages such as high sensitivity and portability. At this point, an important aspect to be taken into account is the microfluidic chip design, the length of the metal layer, as well as the multiplexing capacity that can be developed on this platform.
- Perform biodetection tests from the biofunctionalization of the gold surface. This aspect also gives rise to the exploration of the most appropriate biofunctionalization process according to the application, which allows reducing the amount of fluidic material as well as the time required in this process prior to detection.
- The use of bimetallic layers can also be considered to be evaluated and integrated into the detection platforms by intensity and angle variance.
- Implementation of the machine learning technique for optimization both in the design of the sensors (geometric aspects of the metallic structure for the excitation of the plasmon polaritons for example) and in the diagnosis, to increase the efficiency and reliability in the detection.

Referências

Affinité Instruments. *The Four Key Concepts of Surface Plasmon Resonance and SPR with Affinité Instruments*. 2019. 1–5 p. Disponível em: <https://secureservercdn.net/198.71.233.163/12b.76f.myftpupload.com/wp-content/uploads/Affinite-Tech-note-SPR.pdf>. Citado 2 vezes nas páginas 21 e 50.

AKIB, T. B. A. et al. Design and numerical analysis of a graphene-coated spr biosensor for rapid detection of the novel coronavirus. *Sensors*, v. 21, n. 10, p. 1–21, 2021. ISSN 14248220. Citado 3 vezes nas páginas 47, 53 e 62.

ALAM, M. Z. *Hybrid plasmonic waveguides: theory and applications*. 171 p. Tese (Doutorado) — University of Toronto, 2012. Citado 2 vezes nas páginas 21 e 31.

Aruna Gandhi, M. S. et al. Recent advances in plasmonic sensor-based fiber optic probes for biological applications. *Applied Sciences (Switzerland)*, v. 9, n. 5, 2019. ISSN 20763417. Citado na página 20.

BARNES, W. L.; DEREUX, A.; EBBESEN, T. W. Surface plasmon subwavelength optics. *Nature*, v. 424, n. 6950, p. 824–830, 2003. ISSN 00280836. Citado na página 24.

BAUDOT, C. et al. Developments in 300mm silicon photonics using traditional CMOS fabrication methods and materials. p. 765–768, 2017. Citado na página 75.

BIJALWAN, A.; SINGH, B. K.; RASTOGI, V. Surface Plasmon Resonance-Based Sensors Using Nano-Ribbons of Graphene and WSe2. *Plasmonics*, Plasmonics, 2020. ISSN 15571963. Citado 3 vezes nas páginas 47, 53 e 62.

BRASIL, E.; RODRIGUES, P.; PEREIRA, H. A. An Open-Source Simulator Applied to Prism Coupling Sensors Based on Kretschmann ' s Configuration. *IEEE Sensors Letters*, v. 3, n. 10, p. 0–3, 2019. Citado na página 33.

BUTT, M. A.; KHONINA, S. N.; KAZANSKIY, N. L. Hybrid plasmonic waveguide-assisted Metal–Insulator–Metal ring resonator for refractive index sensing. *Journal of Modern Optics*, Taylor & Francis, v. 65, n. 9, p. 1135–1140, 2018. ISSN 13623044. Disponível em: <https://doi.org/10.1080/09500340.2018.1427290>. Citado na página 72.

BUTT, M. A.; KHONINA, S. N.; KAZANSKIY, N. L. Plasmonic refractive index sensor based on M-I-M square ring resonator. *2018 International Conference on Computing, Electronic and Electrical Engineering, ICE Cube 2018*, IEEE, p. 1–4, 2019. Citado 4 vezes nas páginas 72, 73, 87 e 89.

BUTT, M. A.; KHONINA, S. N.; KAZANSKIY, N. L. Metal-insulator-metal nano square ring resonator for gas sensing applications. *Waves in Random and Complex Media*, Taylor & Francis, v. 31, n. 1, p. 146–156, 2021. ISSN 17455049. Disponível em: <https://doi.org/10.1080/17455030.2019.1568609>. Citado 4 vezes nas páginas 72, 73, 87 e 89.

CHAO, C. T. C. et al. Highly sensitive and tunable plasmonic sensor based on a nanoring resonator with silver nanorods. *Nanomaterials*, v. 10, n. 7, p. 1–14, 2020. ISSN 20794991. Citado na página 72.

CHAO, C. T. C. et al. Highly sensitive and tunable plasmonic sensor based on a nanoring resonator with silver nanorods. *Nanomaterials*, v. 10, n. 7, p. 1–14, 2020. ISSN 20794991. Citado na página 75.

CHAU, Y. F. C. Mid-infrared sensing properties of a plasmonic metal-insulator-metal waveguide with a single stub including defects. *Journal of Physics D: Applied Physics*, IOP Publishing, v. 53, n. 11, 2020. ISSN 13616463. Citado 4 vezes nas páginas 73, 75, 87 e 89.

CHAU, Y. F. C. et al. Ultrawide bandgap and high sensitivity of a plasmonic metal-insulator-metal waveguide filter with cavity and baffles. *Nanomaterials*, v. 10, n. 10, p. 1–17, 2020. ISSN 20794991. Citado na página 75.

CHAU, Y. F. C. et al. Improved refractive index-sensing performance of multimode fano-resonance-based metal-insulator-metal nanostructures. *Nanomaterials*, v. 11, n. 8, 2021. ISSN 20794991. Citado 2 vezes nas páginas 87 e 89.

CHEN, L. et al. Numerical investigations of a near-infrared plasmonic refractive index sensor with extremely high figure of merit and low loss based on the hybrid plasmonic waveguide-nanocavity system. *Optics Express*, v. 24, n. 20, p. 23260, 2016. ISSN 1094-4087. Citado na página 73.

CHIANG, K. S. Dual effective-index method for the analysis of rectangular dielectric waveguides. *Applied Optics*, v. 25, n. 13, p. 2169, 1986. ISSN 0003-6935. Citado na página 75.

CHINOWSKY, T. M. et al. Performance of the Spreeta 2000 integrated surface plasmon resonance affinity sensor. *Sensors and Actuators, B: Chemical*, v. 91, n. 1-3, p. 266–274, 2003. ISSN 09254005. Citado na página 30.

Chou Chau, Y.-F. et al. Significantly enhanced coupling effect and gap plasmon resonance in a MIM-cavity based sensing structure. *Scientific Reports*, Nature Publishing Group UK, v. 11, n. 1, p. 1–17, 2021. ISSN 2045-2322. Disponível em: <https://doi.org/10.1038/s41598-021-98001-z>. Citado na página 72.

ČTYROKÝ, J. et al. Theory and modelling of optical waveguide sensors utilising surface plasmon resonance. *Sensors and Actuators, B: Chemical*, v. 54, n. 1, p. 66–73, 1999. ISSN 09254005. Citado na página 31.

CYTIVA. *Biacore 8K and Biacore 8K +*. cytiva, 2020. 8 p. Disponível em: <https://cdn.cytivalifesciences.com/api/public/content/digi-18070-pdf>. Citado na página 30.

CYTIVA/BIACORE. *Biacore systems for more information and faster decisions biological realities*. [S.l.], 2022. 12 p. Disponível em: <https://cdn.cytivalifesciences.com/api/public/content/digi-18392-pdf>. Citado na página 30.

DAI, D.; HE, S. A silicon-based hybrid plasmonic waveguide with a metal cap for a nano-scale light confinement. *Optics Express*, v. 17, n. 19, p. 16646, 2009. ISSN 1094-4087. Citado na página 72.

DEBACKERE, P.; BIENSTMAN, P.; BAETS, R. *Nanophotonic Biosensor based on Surface Plasmon Interference*. Tese (Doutorado), 2009. Citado na página 20.

DEBACKERE, P. et al. Surface plasmon interferometer in silicon-on-insulator: Novel concept for an integrated biosensor. *IEEE International Conference on Group IV Photonics GFP*, v. 14, n. 16, p. 7–9, 2006. ISSN 19492081. Citado 4 vezes nas páginas 31, 72, 87 e 89.

DIETZEL, A. et al. *Micro- and nano- structuring using ion beams*. Woodhead Publishing Limited, 2006. 9–12 p. Disponível em: <http://dx.doi.org/10.1016/B978-008045263-0/50003-9>. Citado na página 76.

FALQUETO, A. Estudo e implementação de um biossensor de Ressonância de Plásmons de Superfície baseado em smartphone Estudo e implementação de um biossensor de Ressonância de Plásmons de Superfície baseado em smartphone. *Dissertação de Mestrado*, 2019. Citado na página 31.

Fernandez H, J. R.; RUMALDO, Y.; HERNANDEZ-FIGUEROA, H. E. Plasmonic sensor design using gold and silicon nitride waveguide at visible and NIR wavelengths. *Optics & Laser Technology*, Elsevier Ltd, v. 153, n. April, p. 108196, 2022. ISSN 00303992. Disponível em: <https://doi.org/10.1016/j.optlastec.2022.108196>. Citado 2 vezes nas páginas 21 e 92.

FOCTEK. *Precision Optical components*. 2022. Disponível em: <https://www.foctek.net/Products/list-112.html>. Citado na página 34.

Glass Dynamics, L. *BK-7 OPTICAL GLASS*. 2022. Disponível em: <http://www.glassdynamicsllc.com/bk7.html>. Citado na página 35.

GUPTA, G.; KONDOH, J. Tuning and sensitivity enhancement of surface plasmon resonance sensor. *Sensors & Actuators: B. Chemical*, v. 122, p. 381–388, 2007. Citado 2 vezes nas páginas 69 e 71.

HAMAMATSU. *S5870 Si PIN photodiode array*. 2022. Disponível em: <https://www.hamamatsu.com/eu/en/product/optical-sensors/photodiodes/si-photodiode-array/segmented-type-si-photodiode/S5870.html>. Citado 2 vezes nas páginas 39 e 40.

HAQUE, T.; ROUF, H. K. A Performance Improved Kretschmann Configuration Based Surface Plasmon Resonance (SPR) Sensor. *1st International Conference on Advances in Science, Engineering and Robotics Technology 2019, ICASERT 2019*, IEEE, v. 2019, n. Icasert, p. 19–22, 2019. Citado na página 62.

HERNÁNDEZ, D. M. Prism-Based Surface Plasmon Resonance for Dual-Parameter Sensing. v. 18, n. 10, p. 4030–4037, 2018. Citado 2 vezes nas páginas 70 e 71.

HILL, R. T. Plasmonic Biosensors. p. 1–28, 2016. Citado na página 20.

HOMOLA, J. *Surface Plasmon Resonance Based Sensors*. [s.n.], 2006. v. 4. 252 p. ISSN 16182642. ISBN 978-3-540-33918-2. Disponível em: <http://link.springer.com/10.1007/b100321>. Citado 3 vezes nas páginas 31, 33 e 57.

HOMOLA, J. *Surface plasmon resonance based sensors, Springer series on chemical sensors and biosensor/Methods and Applications*. [S.l.: s.n.], 2006. v. 4. 7–8 p. ISBN 9783540339182. Citado 5 vezes nas páginas 24, 74, 79, 81 e 85.

IFGW. *Device Research Laboratory*. 2022. Disponível em: <https://sites.ifi.unicamp.br/lpd/>. Citado na página 35.

IMEC. *BIOPIX TECHNOLOGY AND LAYOUT HANDBOOK*. 2020. 20 p. Citado na página 75.

KALATEC. *Motores De Passo*. Campinas, Brasil: [s.n.], 2022. 41 p. Disponível em: <http://www.mecatronica.eesc.usp.br/wiki/upload/0/0a/Motor{_}passo.> Citado na página 34.

KAZANSKIY, N. L.; KHONINA, S. N.; BUTT, M. A. Plasmonic sensors based on Metal-insulator-metal waveguides for refractive index sensing applications: A brief review. *Physica E: Low-Dimensional Systems and Nanostructures*, Elsevier B.V., v. 117, n. October 2019, p. 113798, 2020. ISSN 13869477. Disponível em: <https://doi.org/10.1016/j.physe.2019.113798>. Citado 2 vezes nas páginas 73 e 81.

KRETSCHMANN, E.; RAETHER, H. Radiative Decay of Non Radiative Surface Plasmons Excited by Light. *Zeitschrift fur Naturforschung - Section A Journal of Physical Sciences*, v. 23, n. 12, p. 2135–2136, 1968. ISSN 18657109. Citado 2 vezes nas páginas 29 e 33.

KRUPIN, O.; BERINI, P. Long-range surface plasmon-polariton waveguide biosensors for human cardiac troponin I detection. *Sensors (Switzerland)*, v. 19, n. 3, p. 1–11, 2019. ISSN 14248220. Citado na página 20.

KWON, M. S. Theoretical investigation of an interferometer-type plasmonic biosensor using a metal-insulator-silicon waveguide. *Plasmonics*, v. 5, n. 4, p. 347–354, 2010. ISSN 15571955. Citado 3 vezes nas páginas 72, 87 e 89.

LAKSONO, F. D. et al. Development of low cost and accurate homemade sensor system based on Surface Plasmon Resonance (SPR). *Journal of Physics: Conference Series*, v. 1011, n. 1, 2018. ISSN 17426596. Citado na página 30.

LAVERS, C. R.; WILKINSON, J. S. A waveguide-coupled surface-plasmon sensor for an aqueous environment. *Sensors and Actuators: B. Chemical*, v. 22, n. 1, p. 75–81, 1994. ISSN 09254005. Citado na página 31.

LEE, K. S. et al. Resolution enhancement in surface plasmon resonance sensor based on waveguide coupled mode by combining a bimetallic approach. *Sensors*, v. 10, n. 12, p. 11390–11399, 2010. ISSN 14248220. Citado na página 31.

LEE, Y. et al. Reflectance Analysis of the Otto Chip Using an Automated Reflectometer. *International Conference on Optical MEMS and Nanophotonics*, v. 2018-July, p. 65–66, 2018. ISSN 21605041. Citado na página 33.

MANOLIS, A. et al. Plasmonics co-integrated with silicon nitride photonics for high-sensitivity interferometric biosensing. *Optics Express*, v. 27, n. 12, p. 17102, 2019. ISSN 1094-4087. Citado 2 vezes nas páginas 62 e 72.

Medina Escuela, A. F. *Desarrollo e implementacion electronica de biosensores basados en SPR para alta sensibilidad.pdf*. 294 p. Tese (Doutorado) — Universidad de Las Palmas de Gran Canaria, 2011. Citado 5 vezes nas páginas 30, 40, 48, 69 e 71.

MÉJARD, R. et al. Tuneable and robust long range surface plasmon resonance for biosensing applications. *Optical Materials*, Elsevier B.V., v. 35, n. 12, p. 2507–2513, 2013. ISSN 0925-3467. Disponível em: <http://dx.doi.org/10.1016/j.optmat.2013.07.011>. Citado 2 vezes nas páginas 70 e 71.

MEJÍA-SALAZAR, J.; OLIVEIRA, O. N. Plasmonic Biosensing. *Chemical Reviews*, n. 118, p. 10617–10625, 2018. Citado na página 20.

METALVET. *BOMBA DE INFUSÃO SERINGA - UHNICA*. 2022. Disponível em: <https://www.metalvet.com.br/departamentos/equipamentos/bomba-de-infusao-seringa-uhnica>. Citado na página 41.

MOHRI, K.; ASAKAWA, K.; SUZUKI, H. Hybrid plasmon waveguide for highly sensitive biosensing. *Optical Engineering*, v. 59, n. 11, p. 1–11, 2020. ISSN 0091-3286. Citado na página 72.

MOREIRA, C. S. et al. Biosensores: tecnologia e Aplicações. *Universidade Federal da Paraíba*, p. 1–18, 2010. Disponível em: <http://www.biologia.seed.pr.gov.br/arquivos/File/biotecnologia/biosensores.pdf>. Citado na página 30.

MOREIRA, L. F. *Caracterização e montagem de um Sensor de Ressonância de Plasmon de Superfície (SPR)*. 66 p. Tese (Master Thesis) — Universidade Estadual de Campinas, 2016. Citado na página 21.

MUSTANSAR, C. *Handbook of functionalized nanomaterials for industrial applications*. [S.l.: s.n.], 2020. 1037 p. ISBN 9780128167878. Citado na página 50.

ORFANIDIS, S. J. *Electromagnetic Waves and Antennas*. [s.n.], 2016. v. 2. 1413 p. ISSN 0717-6163. ISBN 9780750649476. Disponível em: <http://www.ece.rutgers.edu/{~}orfanidi/ew>. Citado 3 vezes nas páginas 29, 35 e 62.

OTTO, A. Excitation of nonradiative surface plasma waves in silver by the method of frustrated total reflection. *Zeitschrift für Physik*, v. 216, n. 4, p. 398–410, 1968. ISSN 14346001. Citado 3 vezes nas páginas 24, 29 e 33.

OULTON, R. F. et al. A hybrid plasmonic waveguide for subwavelength confinement and long-range propagation. *Nature Photonics*, v. 2, n. 8, p. 496–500, aug 2008. ISSN 17494885. Disponível em: <http://www.nature.com/articles/nphoton.2008.131>. Citado na página 72.

P. B. Johnson and R. W. Christy. Optical Constant of the Nobel Metals. *Physical Review B*, v. 6, n. 12, p. 4370–4379, 1972. Citado 2 vezes nas páginas 62 e 75.

PANDEY, P. S.; RAGHUWANSHI, S. K.; KUMAR, S. Recent Advances in Two-Dimensional Materials-Based Kretschmann Configuration for SPR Sensors: A Review. *IEEE Sensors Journal*, IEEE, v. 22, n. 2, p. 1069–1080, 2022. ISSN 15581748. Citado na página 33.

PHOTONICS, N. *NKT Photonics SuperK COMPACT*. 2022. Disponível em: <https://www.nktphotonics.com/products/supercontinuum-white-light-lasers/superk-compact/>. Citado na página 94.

PREECHABURANA, P. et al. Surface plasmon resonance chemical sensing on cell phones. *Angewandte Chemie - International Edition*, v. 51, n. 46, p. 11585–11588, 2012. ISSN 14337851. Citado na página 31.

RAMIREZ, J. C. et al. Study of a low-cost trimodal polymer waveguide for interferometric optical biosensors. *Optics Express*, v. 23, n. 9, p. 11985, 2015. ISSN 10944087. Citado na página 21.

RAMIREZ, J. C. et al. Dielectric barrier discharge plasma treatment of modified SU-8 for biosensing applications. *Biomedical Optics Express*, v. 9, n. 5, p. 2168, 2018. ISSN 2156-7085. Citado na página 21.

Richard B. M. Schasfoort. *Handbook of Surface Plasmon Resonance*. [S.l.: s.n.], 2017. 554 p. ISBN 9781788010283. Citado 4 vezes nas páginas 20, 30, 33 e 50.

SAGMEISTER, M. et al. Monolithically Integrated, CMOS-Compatible SiN Photonics for Sensing Applications. *Proceedings*, v. 2, n. 13, p. 1023, 2018. Citado na página 75.

SANDFORD, A. *Coronavirus: Half of humanity now on lockdown as 90 countries call for confinement*. 2020. Disponível em: <https://www.euronews.com/2020/04/02/coronavirus-in-europe-spain-s-death-toll-hits-10-000-after-record-950-new-deaths-in-24-hou>. Citado na página 20.

SCHOOL, O. M. *COVID-19 Data Explorer*. 2022. Disponível em: <https://ourworldindata.org/explorers/coronavirus-data-explorer>. Citado na página 20.

SCHOTT. *Optical Glass Data Sheets*. Duryea, 2014. 127 p. Citado na página 62.

SCRIBBR. *Coefficient of Determination (R2) Calculation and Interpretation*. 2022. Disponível em: <https://www.scribbr.com/statistics/coefficient-of-determination/>. Citado na página 51.

SIERRA, J. H. et al. Pedestal waveguides based on GeO2-Bi2O3, GeO2-PbO, Ta2O5 and SiOxNy cores as platforms for optical amplifiers and nonlinear optics applications: Review of recent advances. *Journal of Luminescence*, v. 236, n. January, 2021. ISSN 00222313. Citado 2 vezes nas páginas 90 e 92.

SIERRA, J. H. et al. Low-loss pedestal Ta 2 O 5 nonlinear optical waveguides. *Optics Express*, v. 27, n. 26, p. 37516, 2019. ISSN 10944087. Citado na página 90.

SINGH, Y.; PASWAN, M. K.; RAGHUWANSHI, S. K. Sensitivity Enhancement of SPR Sensor with the Black Phosphorus and Graphene with Bi-layer of Gold for Chemical Sensing. *Plasmonics*, Springer US, v. 16, n. 5, p. 1781–1790, 2021. ISSN 15571963. Disponível em: <https://doi.org/10.1007/s11468-020-01315-3>. Citado 2 vezes nas páginas 70 e 71.

SOLER, M.; HUERTAS, C. S.; LECHUGA, L. M. Label-free plasmonic biosensors for point-of-care diagnostics: a review. *Expert Review of Molecular Diagnostics*, Taylor & Francis, v. 19, n. 1, p. 71–81, 2019. ISSN 17448352. Disponível em: <https://doi.org/10.1080/14737159.2019.1554435>. Citado na página 20.

SPLAB. *Knittel lamínulas*. 2022. Disponível em: <https://www.splab.com.br/knittel-laminulas>. Citado na página 35.

SRIVASTAVA, S. K.; VERMA, R.; GUPTA, B. D. Surface plasmon resonance based fiber optic sensor for the detection of low water content in ethanol. *Sensors and Actuators, B: Chemical*, Elsevier B.V., v. 153, n. 1, p. 194–198, 2011. ISSN 09254005. Disponível em: <http://dx.doi.org/10.1016/j.snb.2010.10.038>. Citado na página 63.

Stefan Maier. *Plasmonics: Fundamentals and applications*. [S.l.: s.n.], 2007. 229 p. ISSN 15206882. ISBN 9780387331508. Citado 2 vezes nas páginas 25 e 33.

SUN, X.; THYLÉN, L.; WOSINSKI, L. Hollow hybrid plasmonic Mach–Zehnder sensor. *Optics Letters*, v. 42, n. 4, p. 807, 2017. ISSN 0146-9592. Citado na página 72.

THORLABS. *DCU224M Câmera CCD, 1280x1240*. 2021. Disponível em: <https://www.thorlabs.com/thorproduct.cfm?partnumber=DCU224M>. Citado na página 59.

THORLABS. *Espectômetro CCD Compacto*. 2022. Disponível em: <https://www.thorlabs.com/newgrouppage9.cfm?objectgroup{_}id=3482{&}pn=CC>. Citado na página 94.

THORLABS. *HNL050LB - Sistema de laser de HeNe, 632.8nm, potência 5mW, polarizacao linear*. 2022. Disponível em: <https://www.thorlabs.com/thorproduct.cfm?partnumber=HNL050LB>. Citado na página 34.

THORLABS. *Isoladores de Espaço Livre Visível (395 - 690 nm)*. 2022. Disponível em: <https://www.thorlabs.com/newgrouppage9.cfm?objectgroup{_}id=2>. Citado na página 34.

THORLABS. *NDC-50C-4M - Filtro circular de densidade neutra variavel Montado, D=50mm, Contínuo,*. 2022. Disponível em: <https://www.thorlabs.de/thorProduct.cfm?partNumber=NDC-50C-4M>. Citado na página 34.

THORLABS. *ThorCam software for scientific and compact USB cameras*. 2022. Disponível em: <https://www.thorlabs.com/software{_}pages/viewsoftwarepage.cfm?code=thorcam{&}vie>. Citado na página 59.

USP. *Departamento de Engenharia de Sistemas Eletrônicos*. 2022. Disponível em: <https://sites.usp.br/psi/departamento/>. Citado na página 90.

WANG, D. et al. Real-time multi-channel SPR sensing based on DMD-enabled angular interrogation. *Optics Express*, v. 26, n. 19, p. 24627, 2018. ISSN 1094-4087. Citado 2 vezes nas páginas 70 e 71.

WANG, X. et al. Investigation of wide-range refractive index sensor based on asymmetric metal-cladding dielectric waveguide structure. *AIP Advances*, v. 8, n. 10, 2018. ISSN 21583226. Citado na página 31.

WOOD, R. W. On a remarkable case of uneven distribution of light in a diffraction grating spectrum. *Proceedings of the Physical Society of London*, v. 18, n. 1, p. 269–275, 1901. ISSN 14787814. Citado na página 24.

ZAIN, H. A. et al. Graphene oxide/Gold coated Kretschmann surface plasmon resonance setup for relative humidity detection. *IEEE Sensors Letters*, IEEE, v. 6, n. 4, p. 4–7, 2022. ISSN 24751472. Citado 2 vezes nas páginas 70 e 71.

ZHANG, Z. et al. Fano resonance based on metal-insulator-metal waveguide-coupled double rectangular cavities for plasmonic nanosensors. *Sensors (Switzerland)*, v. 16, n. 5, p. 22–24, 2016. ISSN 14248220. Citado 4 vezes nas páginas 72, 73, 87 e 89.

ZHAO, Y. et al. Current status of optical fiber biosensor based on surface plasmon resonance. *Biosensors and Bioelectronics*, Elsevier B.V., v. 142, n. July, p. 12, 2019. ISSN 18734235. Disponível em: <https://doi.org/10.1016/j.bios.2019.111505>. Citado na página 32.

ZHOU, L. et al. Miniature microring resonator sensor based on a hybrid plasmonic waveguide. *Sensors*, v. 11, n. 7, p. 6856–6867, 2011. ISSN 14248220. Citado na página 72.

ZHUANG, J. et al. Advanced "lab-on-a-chip" to detect viruses – Current challenges and future perspectives. *Biosensors and Bioelectronics*, Elsevier B.V., v. 163, n. March, p. 112291, 2020. ISSN 18734235. Disponível em: <https://doi.org/10.1016/j.bios.2020.112291>. Citado na página 20.

ZINOVIEV, K. E. et al. Integrated bimodal waveguide interferometric biosensor for label-free analysis. *Journal of Lightwave Technology*, v. 29, n. 13, p. 1926–1930, 2011. ISSN 07338724. Citado 2 vezes nas páginas 81 e 93.